

May 2016

Application of Reynolds Stress Model Using Direct Modeling and Actuator Disk Approaches for a Small-Scale Wind Turbine

Randall Scott Jackson
University of Wisconsin-Milwaukee

Follow this and additional works at: <https://dc.uwm.edu/etd>



Part of the [Mechanical Engineering Commons](#)

Recommended Citation

Jackson, Randall Scott, "Application of Reynolds Stress Model Using Direct Modeling and Actuator Disk Approaches for a Small-Scale Wind Turbine" (2016). *Theses and Dissertations*. 1156.
<https://dc.uwm.edu/etd/1156>

This Dissertation is brought to you for free and open access by UWM Digital Commons. It has been accepted for inclusion in Theses and Dissertations by an authorized administrator of UWM Digital Commons. For more information, please contact open-access@uwm.edu.

APPLICATION OF REYNOLDS STRESS MODEL USING DIRECT MODELING AND
ACTUATOR DISK APPROACHES FOR A SMALL-SCALE WIND TURBINE

by

Randall S. Jackson

A Dissertation Submitted in
Partial Fulfillment of the
Requirements for the Degree of

Doctor of Philosophy
in Engineering

at

The University of Wisconsin-Milwaukee

May 2016

ABSTRACT
APPLICATION OF REYNOLDS STRESS MODEL USING DIRECT MODELING AND
ACTUATOR DISK APPROACHES FOR A SMALL-SCALE WIND TURBINE

Randall S. Jackson

The University of Wisconsin-Milwaukee, 2016
Under the Supervision of Professor Ryoichi Amano

The Reynolds Stress Model (RSM) has been avoided for turbulence closure in CFD simulations of wind turbines, largely due to the computational expense and the high potential for numerical instability. The advantage of using RSM is having access to shear stresses that are not available from two-equation RANS-based closure models like $k-\varepsilon$ and $k-\omega$. Access to the shear stresses will aid in the understanding of how the blade design will affect the wake, particularly in the near-wake region. In this research, the RSM turbulence model has been successfully applied in simulating a three-bladed small-scale wind turbine through a direct-model approach and an actuator disk approach. In the direct-model method, the turbine blades were discretized within a rotating subdomain and in the actuator disk method, the turbine blades were modeled as a rotating disk using the Virtual Disk model available in Star CCM+. The transient Rigid Body Motion (RBM) simulation was able to accurately predict velocity deficit and tip vortices that compared well with hot-wire measurements and high speed images. The actuator disk method is more practical in simulating wind farms due to the simplified mesh and requires accurate information for lift and drag coefficients. Experimental results showed interaction between the tower and rotating blades can create significant turbulence in the wake. Experiments with multiple turbines showed how each turbine contributed to the velocity deficit and total turbulence intensity. For the experimental blade design, the velocity deficit recovered and turbulence intensity had dissipated within three rotor diameters.

©Copyright by Randall S. Jackson, 2016
All Rights Reserved

DEDICATION

It has been a long and arduous adventure, but I would like to thank my lovely wife, Sharon, for her love and support since starting on this quest. Thank you to my daughters Stephanie, Kelly, and Randee; I tried not to miss many of your athletic or extracurricular activities, and I hope I have inspired you to continue your education to the highest level possible. I love you all very much. This work would not have been completed without the patience and guidance of my advisor, Dr. Ryoichi Amano. I would also like to thank Ron Morgenson, K.C. Fung, and HydraForce management for their support and flexibility. Since beginning my doctoral studies in 2002, I have lost two people very dear and close to me. I would like to dedicate this work in their honor, for, without them, I would not be where I am today. To my mother, Barb Lukas, you taught me never give up, no matter how old you are. I miss your laugh and our long talks. To my father-in-law, Ted Linneman, you were an incredible man with a giant heart.

TABLE OF CONTENTS

| | |
|---|------|
| TABLE OF CONTENTS..... | v |
| LIST OF FIGURES | vii |
| LIST OF TABLES..... | xiii |
| LIST OF NOMENCLATURE..... | xiv |
| 1 Introduction..... | 1 |
| 1.1 Background | 3 |
| 2 Literature Review..... | 3 |
| 3 Model Wind Turbine Design | 9 |
| 3.1 Turbine Blade Design..... | 10 |
| 3.2 Blade Element Momentum Analysis..... | 13 |
| 4 Wind Tunnel | 16 |
| 4.1 Layout and Description | 17 |
| 4.2 Traverse System | 18 |
| 4.3 Data Acquisition and Instrumentation..... | 19 |
| 4.3.1 Hot Wire Probe | 19 |
| 4.3.2 DAQ Hardware | 20 |
| 4.3.3 Air Temperature..... | 20 |
| 4.3.4 Blade Rotation Speed..... | 20 |
| 5 Hot Wire Anemometry | 22 |
| 5.1 Constant Temperature Anemometer | 23 |
| 5.2 Overheat Adjustment..... | 24 |
| 5.3 Calibration Velocity..... | 25 |
| 5.4 Dantec 54H10 Hot Wire Calibrator | 26 |
| 5.4.1 Isentropic Flow Relations and Static Pressure Correction..... | 28 |
| 5.5 Hot-Wire Calibration Methods..... | 30 |
| 5.5.1 Effective Angle Method..... | 31 |
| 5.5.2 Polynomial Surface Fit | 38 |
| 5.5.3 Surface Interpolation with MATLAB..... | 42 |
| 5.5.4 Method Comparison..... | 42 |
| 5.6 Temperature Correction | 46 |
| 6 Model Wind Turbines-Experimental Results and Discussion | 46 |
| 6.1 Empty Tunnel..... | 46 |
| 6.1.1 Empty Tunnel Characterization | 47 |

| | | |
|-------------|--|-----|
| 6.1.2 | Turbulence measurements | 48 |
| 6.2 | Experiments with Model Wind Turbines | 52 |
| 6.2.1 | Single Turbine Measurements | 54 |
| 6.2.2 | Dual Turbine Results | 61 |
| 6.2.3 | Triple Turbine Results | 66 |
| 6.3 | High Speed Camera Imaging | 72 |
| 7 | Computational Study | 75 |
| 7.1 | Computational Domains and Boundary Conditions-Direct Model..... | 75 |
| 7.2 | Grid Generation-Direct Model | 79 |
| 7.3 | Computational Domains and Boundary Conditions-Actuator Disc..... | 81 |
| 7.4 | Grid Generation-Actuator Disk..... | 83 |
| 7.5 | Governing Equations..... | 84 |
| 7.6 | Numerical Method..... | 88 |
| 7.7 | Grid Sensitivity | 90 |
| 7.8 | CFD Results and Comparison to Experimental Data..... | 92 |
| 8 | Conclusions and Recommendations | 105 |
| | References..... | 106 |
| Appendix A. | LabVIEW Instruments | 112 |
| Appendix B. | MATLAB Scripts..... | 116 |
| Appendix C. | Measurement Uncertainty and Error | 125 |
| Appendix D. | Measurement Locations | 128 |
| | Curriculum Vitae | 129 |

LIST OF FIGURES

| | |
|---|----|
| Figure 1-1. The United States 2014 year end wind energy production [1]..... | 1 |
| Figure 2-1. Illustration of actuator disk (AD), actuator line (AL), and actuator surface (AS) methods for modeling a turbine [5]. | 5 |
| Figure 3-1. Model wind turbine design..... | 10 |
| Figure 3-2. Model blade design | 11 |
| Figure 3-3. NACA4424 blade profile | 11 |
| Figure 3-4. Rotor model and section locations as entered in QBlade..... | 14 |
| Figure 3-5. Rotating blade velocity vectors (a) and associated lift and drag forces (b) | 15 |
| Figure 3-6. Calculated thrust and torque coefficients for model turbine blade using QBlade software..... | 16 |
| Figure 4-1. Wind tunnel at UWM..... | 17 |
| Figure 4-2. Dantec Model 55P64 hot wire probe | 19 |
| Figure 4-3. Hot-wire probe wire orientation..... | 19 |
| Figure 4-4. Blade rotational speed measured with Hall-effect sensor (a) CAD layout of sensor (b) operation of sensor showing square wave output | 21 |
| Figure 5-1 Simplified hot wire anemometer circuit..... | 23 |
| Figure 5-2. Dantec 54T30 Mini-CTA setting for wire 1 | 25 |
| Figure 5-3. Dantec 54T30 Mini-CTA setting for wire 2 | 25 |
| Figure 5-4 Benchtop equipment used to calibrate the hot wire sensors: Dantec 54H10 calibrator (1), Fluke Model 922 Micromanometer (2), Fluke Model 87 Multimeter (3), and Conex JDB1 Digital Barometer (4), 2-Axis Probe Support Holder (5) | 27 |
| Figure 5-5. Sample hot-wire calibration from spreadsheet supplied by Dantec Dynamics..... | 28 |
| Figure 5-6. Residual sum of squares error (SSE) in determining n values for power law curve fit | 34 |
| Figure 5-7. Power law curve fit from Equation (5.15) | 35 |
| Figure 5-8. Hot wire calibration using a 4th order polynomial curve fit..... | 36 |

| | |
|--|----|
| Figure 5-9. Hot wire calibration fixture shown at zero yaw angle. | 38 |
| Figure 5-10. Calibration velocity at different yaw angles. | 39 |
| Figure 5-11. Yaw angle at different velocity settings (m/s). | 39 |
| Figure 5-12. Points used to establish calibration surfaces and points used for error evaluation. . | 43 |
| Figure 5-13. Comparison of normalized standard deviation for different hot wire calibration methods. | 44 |
| Figure 5-14. In-situ calibration of hot wire anemometer. | 45 |
| Figure 5-15. In-situ calibration correction for probe angle. | 46 |
| Figure 6-1. Wind tunnel velocity at different motor drive frequencies, $T_o=24.1$ C. | 47 |
| Figure 6-2. Half-plane inlet velocity measurements at three different motor drive frequencies; hot wire probe located 21 cm downstream of test section. | 48 |
| Figure 6-3. Time series of U-velocity at test section inlet, 10 Hz drive frequency. | 51 |
| Figure 6-4. Time series of V-velocity at test section inlet, 10 Hz drive frequency. | 51 |
| Figure 6-5. Power spectral density (PSD) of velocity signal in empty wind tunnel at various motor drive frequency settings. | 52 |
| Figure 6-6. Wake profiles of a horizontal-axis wind turbine [72]. | 52 |
| Figure 6-7. Dual turbine installation in test section. | 53 |
| Figure 6-8. Measurement plane locations for single turbine experiments. | 54 |
| Figure 6-9. Measured blade speed with hot-wire probe positioned at the hub height and at planes shown in Figure 6-8. | 55 |
| Figure 6-10. Velocity deficit profiles for three vertical measurement regions at locations shown in Figure 6-8, $U_\infty=6.6$ m/s. | 56 |
| Figure 6-11. Downstream velocity deficit from vertical measurements at various y/r values, $U_\infty=6.6$ m/s. | 57 |
| Figure 6-12. Velocity deficit profiles for three horizontal measurement regions at locations shown in Figure 6-8, $U_\infty=6.6$ m/s. | 58 |
| Figure 6-13 Turbulence intensity from two measurement regions in the vertical direction at x/D_b locations shown in Figure 6-8, $U_\infty=6.6$ m/s. | 59 |

| | |
|--|----|
| Figure 6-14. Downstream turbulence intensity from vertical measurements at various y/r values, $U_\infty=6.6$ m/s..... | 60 |
| Figure 6-15. Measurement plane locations for dual turbine experiments. | 61 |
| Figure 6-16. Measured blade speed with hot-wire probe positioned at the hub height and at planes shown in Figure 6-15. | 62 |
| Figure 6-17. Velocity deficit profiles for three vertical measurement regions at locations shown in Figure 6-15..... | 63 |
| Figure 6-18. Downstream velocity deficit from vertical measurements at various y/r values, $U_\infty=6.6$ m/s..... | 64 |
| Figure 6-19. Velocity deficit profiles for three horizontal measurement regions at locations shown in Figure 6-15. | 64 |
| Figure 6-20. Turbulent intensity profiles from vertical measurements at locations shown in Figure 6-15..... | 65 |
| Figure 6-21. Downstream turbulence intensity from vertical measurements at various y/r values, $U_\infty=6.6$ m/s..... | 65 |
| Figure 6-22. Measurement plane locations for measurements using three turbines..... | 66 |
| Figure 6-23. Three model turbines aligned in the wind tunnel with hot wire probe positioned at maximum distance from turbine centerline. | 67 |
| Figure 6-24. Measured blade speed with hot-wire probe positioned at the hub height and at planes shown in Figure 6-22..... | 68 |
| Figure 6-25. Velocity deficit profiles for three vertical measurement regions along turbine center line at locations shown in Figure 6-22..... | 68 |
| Figure 6-26. Downstream velocity deficit from vertical measurements at various y/r values, $U_\infty=6.6$ m/s..... | 69 |
| Figure 6-27 Velocity deficit profiles from horizontal measurements at locations show in Figure 6-22..... | 70 |
| Figure 6-28. Turbulence intensity profiles for three vertical measurement regions at locations shown in Figure 6-16. | 70 |
| Figure 6-29. Comparison of velocity deficit with multiple turbines. | 71 |
| Figure 6-30. Comparison of turbulence intensity with multiple turbines..... | 71 |
| Figure 6-31. High speed images showing wake vortices from a single turbine..... | 73 |

| | |
|--|----|
| Figure 6-32. High speed image showing wake vortex and turbulence from two turbines spaced 2 rotor diameters apart | 74 |
| Figure 6-33. High speed image showing wake vortex and turbulence from three turbines spaced 2 rotor diameters apart | 74 |
| Figure 7-1. Computational domain of direct rotor model with traverse arm located at $x/D_b \sim 1$... | 76 |
| Figure 7-2. Computational domain of direct rotor model with traverse arm located at $x/D_b \sim 3$.. | 76 |
| Figure 7-3. Computational domain of direct rotor model with traverse arm located at $x/D_b \sim 5$.. | 76 |
| Figure 7-4. Computational domain of direct rotor model with traverse arm located at $x/D_b \sim 8$.. | 77 |
| Figure 7-5. Rotating subdomain using trimmed mesh model with prism layer meshing at rotor surfaces | 79 |
| Figure 7-6. Prism layer meshes at blade surface..... | 80 |
| Figure 7-7. Mesh at vertical mid-plane of computational domain with traverse arm at $x/D \sim 5$ | 81 |
| Figure 7-8. Computational domain using a Virtual Disk model and a single turbine; traverse located at max position $x/D \sim 7$ | 82 |
| Figure 7-9. Virtual Disk mesh | 83 |
| Figure 7-10. Computational grid using actuator disk and traverse located at $x/D_b \sim 8$ | 84 |
| Figure 7-11. Typical residuals for last 500 iterations in direct model MRF simulations | 89 |
| Figure 7-12. Typical residuals for last 500 iterations in actuator disk simulations | 90 |
| Figure 7-13. Experimental measurement locations for $x/D_b < 1$ | 92 |
| Figure 7-14. Experimental measurement locations for $x/D_b > 1$ | 92 |
| Figure 7-15. Comparison of turbulence closure models in predicting the velocity deficit using a Rigid Body Motion (RBM) method at three different wake locations. | 94 |
| Figure 7-16. Plan view of velocity contour from MRF simulation with traverse located at $x/D_b \sim 1$ | 95 |
| Figure 7-17. Plan view of velocity contour from MRF simulation with traverse located at $x/D_b \sim 3$ | 95 |
| Figure 7-18. Plan view of velocity contour from MRF simulation with traverse located at $x/D_b \sim 5$ | 95 |

| | |
|---|-----|
| Figure 7-19. Plan view of velocity contour from MRF simulation with traverse located at $x/D_b \sim 8$. | 96 |
| Figure 7-20. Plan view of z-axis vorticity contour from RBM simulation with traverse located at $x/D_b \sim 1$. | 96 |
| Figure 7-21. Plan view of z-axis vorticity contour from RBM simulation with traverse located at $x/D_b \sim 3$. | 97 |
| Figure 7-22. Plan view of z-axis vorticity contour from RBM simulation with traverse located at $x/D_b \sim 5$. | 97 |
| Figure 7-23. Plan view of velocity contour from actuator disk method with traverse located at $x/D_b \sim 5$. | 98 |
| Figure 7-24. Comparison of velocity deficit to experimental data at several vertical measurement planes using different CFD modeling methods: (a) S8 (b) S9 (c) S10 (d) S11, $U_\infty = 6.60$ m/s, traverse arm positioned at $x/D_b \sim 8$. | 99 |
| Figure 7-25. Comparison of velocity deficit to experimental data at several vertical measurement planes using different CFD modeling methods: (a) S12 (b) S13 (c) S14 (d) S15, $U_\infty = 6.60$ m/s, traverse arm positioned at $x/D_b \sim 8$. | 100 |
| Figure 7-26. Comparison of velocity deficit to experimental data at several vertical measurement planes using different CFD modeling methods: (a) S16 (b) S17 (c) S18 (d) S19, $U_\infty = 6.60$ m/s, traverse arm positioned at $x/D_b \sim 8$. | 101 |
| Figure 7-27. Comparison of velocity deficit to experimental data at several vertical measurement planes using different CFD modeling methods: (a) S20 (b) S21 (c) S22 (d) S23, $U_\infty = 6.60$ m/s, traverse arm positioned at $x/D_b \sim 8$. | 101 |
| Figure 7-28. Comparison of velocity deficit to experimental data for the RBM method with the traverse arm positioned at: (a) $x/D_b \sim 1$ (b) $x/D_b \sim 3$ (c) $x/D_b \sim 5$; $U_\infty = 6.60$ m/s. | 102 |
| Figure 7-29. Percent difference between simulation and experiment when accounting for the traverse location. | 103 |
| Figure 7-30. Isosurface of Q-criterion, colored by vorticity, from a transient RBM simulation | 104 |
| Figure 7-31. High speed camera frame capture showing wake vortex structure and eventual dissipation | 104 |
| Figure A-1 LabVIEW instrument for hot wire calibration | 113 |
| Figure A-2. First level of virtual instrument to set initial position of hot wire and initialize communication with Velmex controller. | 114 |

Figure A-3. Secondary level to move traverse and acquire velocity data with directional options to position the traverse 114

Figure A-4. Alternate secondary level to move traverse and acquire velocity data with directional options to position traverse. 115

Figure A-5. Final level to move traverse and acquire velocity data with alternate directional option 115

LIST OF TABLES

| | |
|---|-----|
| Table 3-1 Model blade design details, solidity $S \sim 0.10$ | 12 |
| Table 4-1. Comparison of blade rotational speed using tachometer and hall-effect sensor. | 21 |
| Table 5-1 Summary of calibrations from three different Dantec 9055P064 probes using power law and polynomial fit methods..... | 37 |
| Table 5-2. Comparison of normalized standard deviation, yaw angle error, and computation time for different calibration methods. | 43 |
| Table 6-1 Empty tunnel turbulent flow statistics at different motor drive frequencies | 50 |
| Table 7-1. Mass flow inlet and turbine speed rotation settings for CFD simulations | 79 |
| Table 7-2 Coefficients for the linear pressure-strain model | 88 |
| Table 7-3. Grid sensitivity summary for direct modeled simulation with traverse located a maximum distance from turbine | 91 |
| Table 7-4. Grid sensitivity summary for the actuator disk simulation with traverse located a maximum distance from turbine | 91 |
| Table A-1. Sample calibration file..... | 112 |
| Table C-1. Uncertainty budget to determine total expanded uncertainty | 125 |
| Table C-2. Comparison of calibration velocity calculation to pitot tube measurements..... | 127 |
| Table D-1. Location of measurement planes shown in Figure 6-8, Figure 6-15, and Figure 6-22 | 128 |

LIST OF NOMENCLATURE

| | |
|---|---|
| a | the speed of sound |
| A_b | swept blade area |
| A_o | hot-wire calibrator nozzle exit area |
| A_N | hot-wire calibrator nozzle inlet area |
| A_w | hot wire surface area |
| c | airfoil chord length |
| C_f | hot-wire calibrator static pressure correction factor |
| C_d | drag coefficient |
| $C_{\varepsilon 1}, C_{\varepsilon 2}, C_{\varepsilon 3}$ | constants in dissipation transport equation |
| C_l | lift coefficient |
| C_m | torque (moment) coefficient |
| C_μ | constant to compute turbulence kinetic energy |
| C_N | nozzle contraction ratio |
| C_T | thrust coefficient |
| D_b | turbine blade diameter |
| D_{ij} | dissipation of Reynolds stress |
| E_i | hot wire anemometer voltage ($i=1, 2$) |
| F_w | pressure-strain wall coefficient |
| H | hub height |
| h | convection coefficient |
| I | turbulent intensity |

| | |
|-------------|--|
| I_w | hot wire probe current |
| K_{FR} | hot-wire calibrator nozzle factor |
| k | turbulent kinetic energy |
| k^2 | hot wire yaw coefficient |
| L | length scale |
| M | Mach number |
| n | power law hot wire calibration constant |
| $n_{i,j,k}$ | components of wall normal vector |
| N_B | blade number |
| p | pressure |
| P' | hot-wire calibrator corrected nozzle static pressure |
| P_{ij} | production of Reynolds stresses |
| P_o | hot-wire calibrator nozzle stagnation pressure |
| P'_o | hot-wire calibrator nozzle corrected stagnation pressure |
| Q | turbine blade torque |
| q | residual sum of squares for hot wire calibration (velocity) surface fit method |
| r | radial distance from rotational centerline |
| R | gas constant |
| Re | Reynolds number |
| R_t | hot-wire calibrator thermistor resistance |
| s | residual sum of squares for hot wire calibration (angle) surface fit method |
| T | turbine thrust or temperature |
| T_w | hot-wire temperature |

| | |
|------------------------|---|
| T_∞ | freestream temperature |
| U | velocity component parallel to free stream |
| U_o | hot-wire calibrator nozzle chamber velocity |
| u_i | velocity |
| u^* | friction velocity at nearest wall |
| U_∞ | free stream velocity |
| U_1, U_2 | intermediate velocities for hot wire calibration |
| U_{cal} | calibration velocity at nozzle exit plane |
| \bar{U} | mean velocity component in free stream direction |
| \tilde{U} | measured velocity component parallel to free stream |
| u_i, u_j, u_k | velocity in i, j, and k directions, respectively |
| u', v' | fluctuating velocity component |
| $\overline{u'_i u'_j}$ | Reynolds stresses |
| V | vertical component of velocity vector |
| \bar{V} | mean velocity component in the vertical direction |
| \tilde{V} | measured vertical hot wire velocity component |
| W | relative velocity experienced by rotating turbine blade |
| x | downstream distance from the turbine blade |
| y | distance to the nearest wall, vertical direction |
| y^+ | dimensionless wall distance |

| | |
|--------------------|--|
| z | distance in horizontal direction |
| Greek | |
| α | angle of attack |
| α_f | angle of measured velocity vector |
| β | turbine blade twist angle |
| δ_{ij} | Kronecker delta |
| ε | turbulent kinetic energy dissipation rate |
| ε_{ij} | dissipation tensor |
| ε_u | normalized standard deviation |
| ϕ | the relative flow angle |
| γ | the ratio of specific heats (~ 1.4 for air) |
| μ_t | turbulent viscosity |
| ϕ_{ij} | pressure-strain correlation |
| θ | hot wire yaw angle |
| θ_{eff} | hot wire probe effective angle |
| ρ | density |
| σ_k | turbulent Schmidt number |
| ω | specific turbulence dissipation rate ($\propto \varepsilon/k$) |
| Ω | angular rotational rate |

1 Introduction

With the increasing need for energy independence, wind power is an excellent alternative to fossil fuels. Wind energy in the United States grew 30% on average over the last five years with a cumulative power capacity nearing 66 GW in 2014. In 2014, 4.9% of the U.S. electrical energy was produced by wind turbines with more wind farms on the horizon. Wind farm size and location is dependent on atmospheric wind conditions, geography, and in some cases, state and local laws. Figure 1-1 shows the U.S. wind energy production by state in 2014 with Texas producing more than twice as much as any other state and with little or no wind energy production in the southeast. The lack of wind energy in this region is most likely due to poor siting conditions.

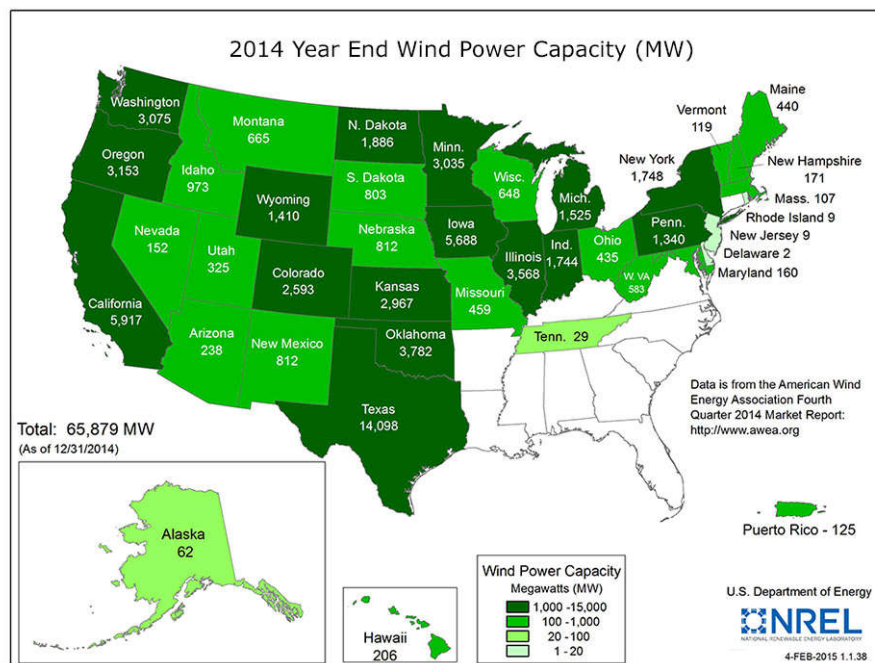


Figure 1-1. The United States 2014 year end wind energy production [1]

Over 80,000 new jobs have been created in the wind energy sector with many more being projected. Of course, wind energy is not without its problems, such as reported health issues due

to exposure to turbulent generated noise and the aesthetic effects on the landscape. With proper care, planning, and additional research, these issues can be mitigated so that wind energy can continue to grow. The growth of wind energy is based on economics and the desire to reduce our carbon footprint. The use of fossil fuels and their effect on global warming is a source of great political debate, but one cannot debate that wind energy is a clean source of renewable energy. The choice to develop a wind farm is usually based on corporate profit goals and payback on an investment. With improving technology and siting methods, wind farms are becoming increasingly more affordable as an alternative source of electricity.

Wind farm power output is highly dependent on the velocity deficit behind wind turbines. Being able to accurately predict the velocity deficit and turbulence generated by wind turbine blades can improve efficiency and lead to more robust turbine designs. The advancement of wind energy as an alternative to hydrocarbons depends heavily on research activities in turbulence modeling and experimentation.

The goals of this research are:

1. Create LabVIEW instruments and set up a data acquisition system for calibrating hot-wire anemometers and automating velocity measurements in the UWM Wind Tunnel Laboratory.
2. Research different methods used for hot-wire calibration and investigate the use of a simple surface interpolation technique compared to the more traditional effective angle method or polynomial surface fit method.
3. Design a small scale wind turbine and perform experiments to study the wake deficit and turbulence intensity using multiple turbines in series.

4. Use commercial CFD software to examine the application of the Reynolds Stress Model (RSM) turbulence closure method to a small scale wind turbine using direct modeling and actuator disk (BEM) models.

1.1 Background

Wind farm layout has a direct effect on energy output and wind farm efficiency. Being able to simulate effectively the wake effects in the development stage of a wind farm can result in optimum spacing, longer wind turbine life, and shorter payback on the investment. Velocity deficit behind wind turbines, wake interaction, and turbulence effects on a wind turbine blade are major concerns in a wind farm. Research using scaled models and Computational Fluid Dynamic (CFD) methods has resulted in more robust turbine blade designs, a better understanding of wind turbine wakes, and improved modeling methods.

2 Literature Review

Advances in wind energy technology are a direct result of research efforts using computational fluid dynamics (CFD) in conjunction with wind turbine experiments. While there is an overwhelming amount of literature available regarding CFD methods and experimental results related to wind turbines, studies using an RSM turbulence model are limited and studies using RSM on a directly modeled wind turbine are non-existent. This first section of this chapter presents computational efforts in developing wake modeling techniques and turbulence closure methods as they relate to horizontal-axis wind turbine (HAWT) and wake analysis. The second section of this chapter presents experimental studies, performed in a controlled laboratory environment (i.e. wind tunnel) using various methods of velocity and turbulence measurement. In many cases, both experimental and numerical results are provided in the same study.

Computational Fluid Dynamics (CFD) has become a staple in the wind energy field and research studies cover a broad range of topics including atmospheric wind profiles, airfoil design, turbine power output, and wake dynamics. Periodically, researchers have summarized advances and state of the art approaches to wind turbine modeling, wake modeling, or CFD for other wind energy topics. Several of these reviews are noteworthy in that they are comprehensive, relevant, and detailed. In 1999, Crespo, et al. [2] provided an overview of the different modeling methods used to predict velocity deficit in the wake of single and multiple wind turbines. Their review included discussions on kinematic wake models, field models, terrain effects, and wind farm modeling. In kinematic models, it is assumed that the perturbation profiles of the velocity deficit and turbulence intensity are axisymmetric and follow a self-similar distribution. Kinematic models express the velocity deficit by an analytical expression developed from theoretical work on co-flowing jets and experimental data. Field models are much like today's CFD models in that they calculate the velocity at every point of the flow field and rely on a numerical solution of turbulent momentum and continuity equations. A major flaw of kinematic and field models is their inability to handle the bodily motion of the wake, known as meandering, that can result from large eddies that are comparable in size to the wake. Meandering is a direct consequence of atmospheric and terrain effects. Early kinematic and field models are still incorporated into software used for wind farm analysis. Vermeer, et al. [3] followed in 2003 with an overview of computational methods relative to horizontal axis wind turbines and included further discussion of kinematic and field models. The unique aspect of the Vermeer paper was their segregation of experimental and analytical research based on near and far wake studies. They also included a thorough review of experiments that had been performed on a variety of wind turbines. Hansen, et al. [4] studied computational methods for wind turbine analysis including Blade Element

Momentum (BEM) methods, panel methods, vortex methods, actuator disc methods. Aeroelastic methods for predicting the dynamic response of the turbine blades from time-dependent aerodynamic loads were also presented. In 2011, Sande, et al. [5] provided a state-of-the-art review of CFD methods for simulating wind turbines. They classified the different numerical methods used and distinguished between models specific to simulating the rotor versus simulating the wake. For simulating the wake, kinematic and field models, previously discussed, are employed. For simulating the rotor, the body forces in the momentum equations can be represented by an actuator disk, actuator line, or actuator surface.

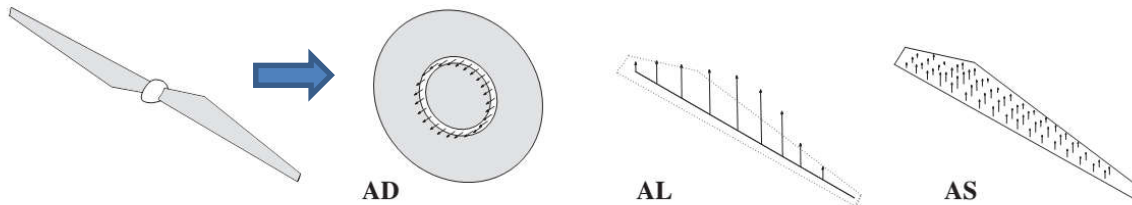


Figure 2-1. Illustration of actuator disk (AD), actuator line (AL), and actuator surface (AS) methods for modeling a turbine [5].

In the case of the actuator disk with uniform loading, the body force is expressed as a function of the approaching relative velocity and the thrust coefficient. For a non-uniformly loaded disk, the body force is dependent on the radial location but is constant over an annular area as seen in Figure 2-1. Sectional lift and drag coefficients are used to determine local forces, and the body force is resolved as a time average of circular line forces. The actuator line method is similar to the computation of local line forces; however, the line forces are time-dependent. Thus, the AL method allows the tip vortex shedding to be calculated. The actuator surface method is also time-dependent, but more complex as the planar surface model forces are determined from pressure and skin friction distribution as well as from lift and drag coefficients. For all non-uniform loading situations, the approaching velocity is computed by interpolating the velocity

field at cell locations near the disk surface. Other researches have provided numerical reviews, but not to the depth as the aforementioned papers. In 2010, Sumner, Watters, and Masson [6] studied various application of CFD to wind energy topics including wind turbine aerodynamics, Atmospheric Boundary Layer (ABL) simulations, and topographical flows. Miller, et al. [7] provided a brief review of a broad range of topics involving numerical computations in wind energy including ABL wind profiling, wind farm siting, CFD methods, and noise generation. In more recent studies where the objective is to determine the turbine power output, validate a solver code, evaluate a meshing technique, or validate a turbulence model, the blade is usually modeled directly with a higher cell density near the blade. Ma, et al., [8] used a commercial code, ANSYS Fluent, to compare an unsteady Delayed-Detached Eddy Simulation (DDES) model to steady Spalart-Allmaras and $k-\omega$ turbulence closure models. Their simulations were evaluated against experimental data from wind tunnel tests on a Fortis Montana 5.8 kW HAWT and they concluded the time-averaged RANS methods tended to overestimate the power losses from the flow field around the turbine compared to the DDES. Sagol, et al. [9] also utilized ANSYS Fluent to perform a similar study, but focused on applying $k-\varepsilon$ and $k-\omega$ methods to compare to NREL Phase VI data. Carrion, et al. [10], used a unique compressible multi-block solver developed at Liverpool University to simulate wind turbines tested in the Large Scale Low-Speed Facility of DNW, the German-Dutch Wind Tunnels. This testing was commonly referred to as the Model Experiments in Controlled Conditions (MEXICO) experiment. Carrion provided a detailed list of all known CFD studies of the MEXICO experiments along with the solver, turbulence models, and geometry used in each study. AbdelSalam and Ramalingam [11] employed ANSYS Fluent to create a full rotor model of a Danwin 180kW turbine and used a standard $k-\varepsilon$ turbulence model to compare the wake velocity profile at various downstream

locations to widely scattered experiment data. The results indicated the full rotor model predicted the downstream wake more accurately than the actuator disc models. Rocha, et al., [12] used an open source CFD package, OpenFOAM, with a $k-\omega$ SST turbulence model to study the performance of small (3 m diameter) prototype, rotor and compare the result to experimental values for the power coefficient. Inlet conditions based on the turbulent length scale were shown to provide unrealistic power coefficients for certain values of the length scale. Tran et al., [13] used the commercial software Star CCM+ from CD-Adapco to predict the wake for a floating offshore wind turbine using a $k-\omega$ SST turbulence model. An overset mesh, sometimes referred to as overlapping or Chimera grid, was incorporated with Rigid Body Motion (RBM) used to simulate the motion of the blade. An alternate approach was also investigated using ANSYS Fluent and a Multiple Reference Frame (MRF) model and the results of both simulations were compared to established BEM codes, FAST, and UBEM. Lawson and Li [14] also used Star CCM+ to simulate an off-shore HAWT and compared the results to BEM code WT_Perf using a hypothetical wind turbine design. CFD simulations with multiple turbines modeled directly are virtually non-existent except for Seydel and Aliseda [15]. They modeled two offset NREL Phase VI rotors with ANSYS Fluent using a $k-\omega$ SST turbulence model. Experimental data for offset turbines was not available, but the results showed excellent agreement with measured values for the pressure coefficient at several radial distances.

Generalized actuator methods are a popular choice for researchers because they allow the wind turbine to be modeled with a much smaller mesh size that significantly reduces the computational expense. Castellani and Vignaroli [16] applied an actuator disc (AD) method and used a $k-\varepsilon$ RNG turbulence closure model to simulate the wake from a 1 MW Bonus wind

turbine located in Western Finland. Although data appeared limited, the AD method showed good agreement with measured values and with alternate wake models. Castellani, et al. [17] also applied the same AD method to simulate a single turbine in the Sexbierum wind farm. The exact values of the velocity deficit and turbulent kinetic energy did not match well with measured values, but the order of magnitude and general behavior was reproduced. The study highlighted the difficulty of comparing a simulation with field measurements where the freestream turbulence may not be well defined or controlled. Wake meandering effects also make it difficult. Martinez Tossas and Leonardi [18] compared AD and actuator line (AL) models using an LES turbulence model in OpenFOAM. Both methods produced similar wake profiles and power output, but the unsteady nature of the AL model was able to capture the vortical structure at the blade locations, which came at a computational expense. Storey et al. [19] proposed an improved alternative to AD methods that will capture the transient effects of the blade without the additional expense.

Over the past decade, there has been a growth in the number of wind tunnel experiments on small-scale wind turbines. The growth can be attributed to the desire to study wake effects under controlled conditions and the need to provide data for CFD validation. Experimental set-up varies depending on the size of the wind tunnel, instrumentation, and test objective. Aubrun, et al. [20, 21], experimented with a small, 3-bladed, 416 mm diameter wind turbine using hot wire anemometry (HWA) to measure the velocity profile at certain distances downstream. The wind tunnel incorporated an upstream mesh to simulate the ABL. For comparison, a non-rotating porous disc was also tested where the disc was designed to have the same velocity deficit at $0.5D_b$. The results indicated the porous disk created similar downstream turbulence

characteristics, and spectral analysis of the HWA data indicated the tip vortex structure was indistinguishable at $x/D_b > 3$. Medici [22] performed wind tunnel experiments on several small turbine models with different blade designs. The experiments were aimed at studying the variation in power output as a function of turbine yaw. Power was determined by the electrical output from a small motor acting as a generator. Using the same equipment and test facilities, additional work performed by Medici, et al. [23] showed that the presence of a wind turbine affects the upstream flow field more than $3D_b$ upstream of a wind turbine. Hot wire anemometry has been used to measure velocity profiles and wake turbulence for single small scale wind turbines [24, 25, 26, 27, 28] and on arrays of wind turbines [29, 30]. Turbulence measurements using Particle Image Velocimetry (PIV) on a single turbine have been captured by Hu, et al. [31], Yang et al. [32], and Massouh and Dobrev [33]. PIV was also used to measure turbulence around an array of small turbines has by Cal, et al. [34] and Lebron, et al. [35].

CFD studies implementing the Reynolds Stress Model (RSM) turbulence closure model for a wind turbine are rare and use an actuator disc model to simulate the wind turbine [36, 37]. The majority of CFD studies that model the rotor directly focus on two-equation methods based on the Boussinesq hypothesis. The wide use of two-equation models is mostly because of the computational expense associated with RSM. With faster and more powerful computers, LES methods are becoming more popular, especially in conjunction with generalized actuator (AD, AL, AS) methods.

3 Model Wind Turbine Design

Three small-scale wind turbines were built for testing in the UWM wind tunnel. Each wind turbine included a custom 3-blade rotor made from ABS plastic, a tower made from 12.7 mm

diameter steel rod, a 30.5 cm x 30.5 cm x 6.4 mm steel base plate, and a small DC motor (Radio Shack P/N 273-0258) to act as a generator. Figure 1 shows a sketch of the assembly.

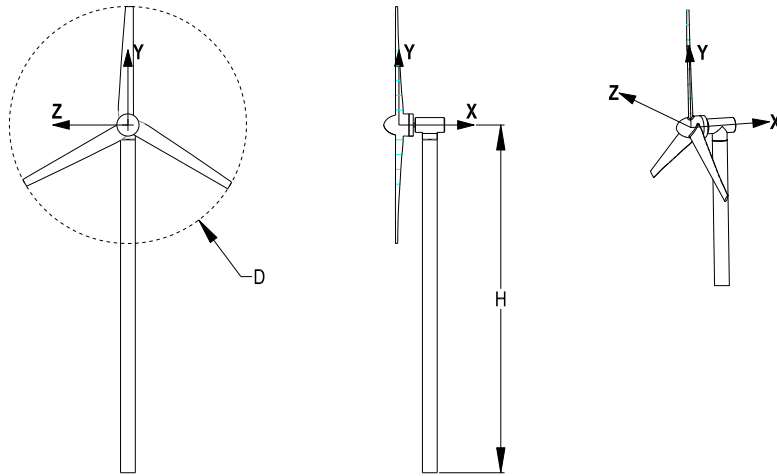


Figure 3-1. Model wind turbine design

The hub height, H , was designed at 30.5 cm and the blade diameter, D_b , was designed at 20.3 cm giving a hub height to blade diameter ratio of 1.5. The overall size of the wind turbines was based on the size of the wind tunnel test section and a desire to fit two turbines side by side, if necessary, with minimal effect from the sides of the wind tunnel. The hub height to blade diameter ratio was selected based on a comparison to several different full-scale wind turbines from various manufacturers.

3.1 Turbine Blade Design

The blade design used for the experiments was arbitrary; however, the blade was designed so that lift and drag coefficients could be determined from published data or airfoil codes. The three-blade model, shown in Figure 3-2, was created using Pro-Engineer software and a *.stp* file of the model was used to create the blades on a 3-D rapid prototyping machine.



Figure 3-2. Model blade design

The turbine blade cross section was based on an NACA 4424 profile shown in Figure 3-3. The NACA 4424 profile was selected because the coordinates are established and it offered a thicker blade profile relative to the chord length to improve the strength and prevent the blades from breaking during handling.

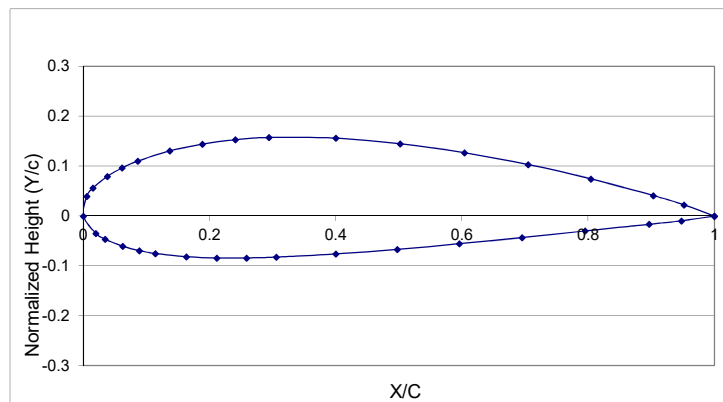


Figure 3-3. NACA4424 blade profile

Details of the blade design are listed in Table 3-1. The blade solidity, S , defined as the ratio of the frontal swept area of the blades to the swept rotor area, was ~ 0.10 .

Table 3-1 Model blade design details, solidity $S=0.10$

| Section | Normalized Radial Distance (x/r) | Chord Length c (m) | Twist Angle β (deg) |
|---------|----------------------------------|--------------------|---------------------------|
| 1 | 0.094 | 0.0159 | 25.1 |
| 2 | 0.125 | 0.0159 | 25.1 |
| 3 | 0.150 | 0.0157 | 24.6 |
| 4 | 0.200 | 0.0152 | 23.4 |
| 5 | 0.250 | 0.0147 | 22.3 |
| 6 | 0.300 | 0.0143 | 21.2 |
| 7 | 0.350 | 0.0138 | 20.1 |
| 8 | 0.400 | 0.0134 | 18.9 |
| 9 | 0.450 | 0.0129 | 17.8 |
| 10 | 0.500 | 0.0125 | 16.7 |
| 11 | 0.550 | 0.0120 | 15.6 |
| 12 | 0.600 | 0.0115 | 14.4 |
| 13 | 0.650 | 0.0111 | 13.3 |
| 14 | 0.700 | 0.0106 | 12.2 |
| 15 | 0.750 | 0.0102 | 11.0 |
| 16 | 0.800 | 0.0097 | 11.0 |
| 17 | 0.850 | 0.0093 | 11.0 |
| 18 | 0.900 | 0.0088 | 11.0 |
| 19 | 0.950 | 0.0083 | 11.0 |
| 20 | 1.000 | 0.0079 | 11.0 |

The known geometry also aided in generating the computer model used to make the blades. A taper was added to the blade along with a twist angle. The blade root was blended at the hub, as opposed to transitioning to a round cross section, to provide greater strength at the root. Other researchers have used small motors attached to the blade to control the blade tip speed, and others have used small torque sensors to estimate the power output from the turbine. In both cases, scaling the results to a full-scale turbine is not practical, but the results provide useful conclusions regarding the behavior of the wind turbine and the wake. For this research, measurement of the motor output power and control of blade speed was abandoned for several reasons:

1. The efficiency of the motor acting as a generator was not known which would provide little information regarding the real wind power extraction.

2. The motor output voltage signal was very noisy and the current too small due to the low blade torque
3. Speed control of the DC motor was not possible.

3.2 Blade Element Momentum Analysis

For the prescribed blade geometry, an open source software, QBlade [38], was used to estimate the thrust and torque coefficients based on Blade Element Momentum (BEM) theory. The software provides a graphical user interface to XFOIL [39], a widely accepted subsonic airfoil design code. The XFOIL code is used to determine the lift and drag coefficients at various attack angles for a given airfoil geometric profile. QBlade uses the lift and drag coefficients and BEM theory to simulate the performance of the rotor. Blade element momentum theory is well published and the applicability to wind turbines is discussed in Burton [40]. In BEM theory, the flow is assumed to pass through the turbine in rotating annular stream tubes. The turbine blade is sectioned into differential elements along the blade span, corresponding to the annular stream tubes, and each element is analyzed for lift and drag forces. The basic assumption of BEM theory is that the lift and drag forces acting on an individual element are the same as those acting on a two-dimensional element with velocity vectors approaching at the same angle of attack. Figure 3-4 shows the sectioned rotor blades as listed in Table 3-1 and as entered into QBlade.

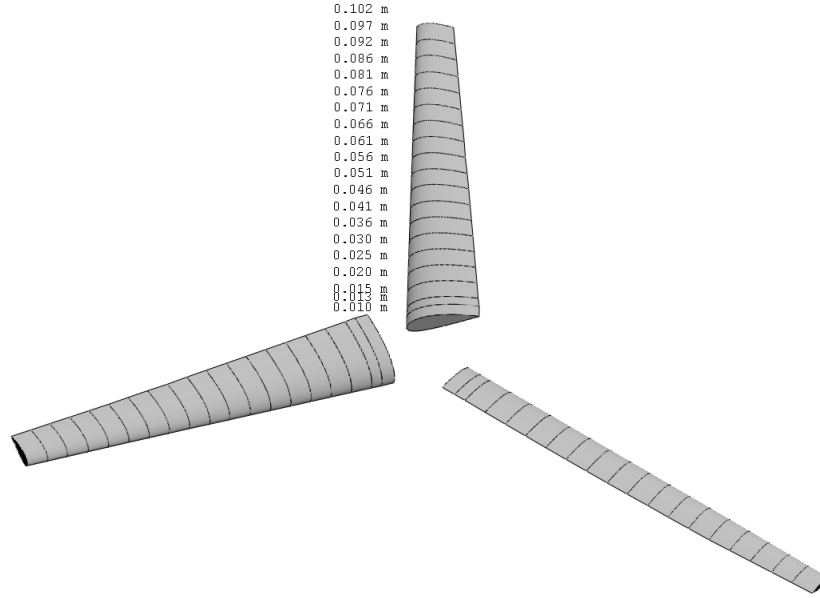


Figure 3-4. Rotor model and section locations as entered in QBlade

Figure 3-5 shows the velocity vectors and lift and drag forces for a cross-section of a blade rotating about the vertical axis. It is assumed there is no aerodynamic interaction between the different elements and the span-wise velocity and three-dimensional effects are ignored. Each element will have a slightly different flow characteristic as they each have a different angular velocity, Ωr , chord length, c , and twist angle, β as noted in Table 3-1.

The thrust on a section of blade is calculated from

$$dT = \frac{1}{2} \rho W^2 N_B c (C_l \cos \phi + C_d \sin \phi) dr \quad (3.1)$$

and the torque on a section of blade is calculated from

$$dQ = \frac{1}{2} \rho W^2 N_B c (C_l \sin \phi - C_d \cos \phi) dr \quad (3.2)$$

The total thrust and total torque on the blades can be determined by numerically integrating equations (3.1) and (3.2). The relative velocity, W , is determined using calculated induction factors at each element location; calculation of induction factors is an iterative process performed behind the scenes in QBlade.

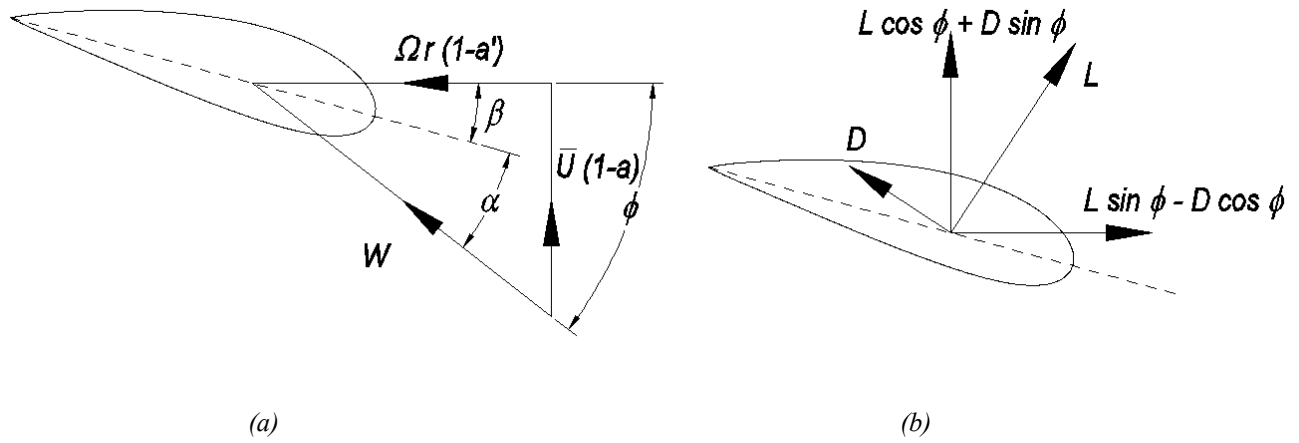


Figure 3-5. Rotating blade velocity vectors (a) and associated lift and drag forces (b)

The thrust coefficient is defined as:

$$C_T = \frac{T}{\frac{1}{2} \rho U_\infty^2 A_b} \quad (3.3)$$

where T is the axial thrust acting on the turbine blades, ρ is the air density, A_b is the swept area of the blades, and U_∞ is the free stream velocity. The thrust coefficient is directly related to the velocity deficit behind the wind turbine because it determines the momentum extracted from the flow. Similarly, the torque (or moment) coefficient is defined as:

$$C_m = \frac{Q}{\frac{1}{2} \rho U_\infty^2 A_b} \quad (3.4)$$

where Q is the torque acting on the turbine blades. Calculated thrust coefficient and moment coefficient values for various tip speed ratios are shown in Figure 3-6.

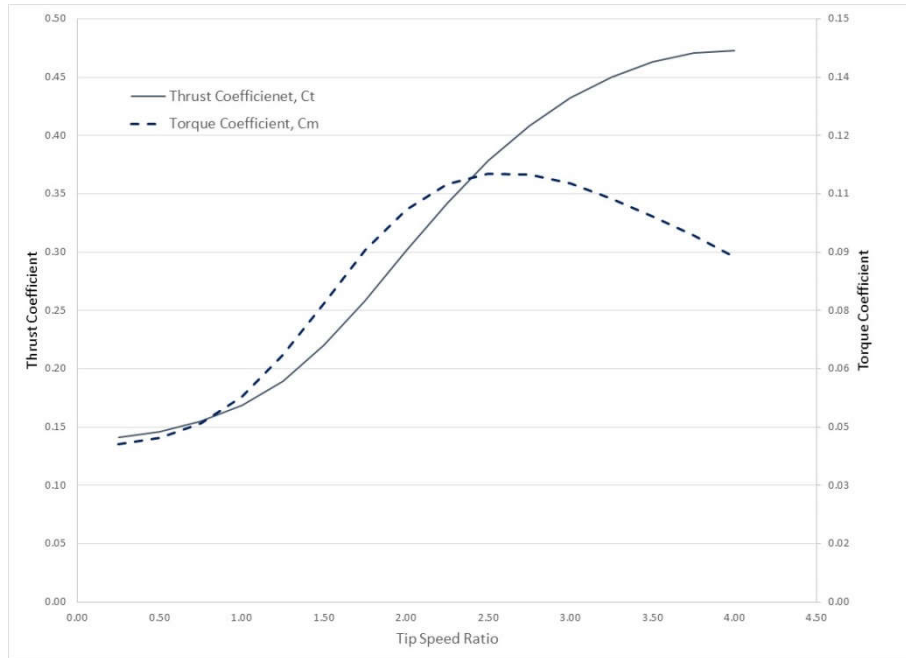


Figure 3-6. Calculated thrust and torque coefficients for model turbine blade using QBlade software.

4 Wind Tunnel

The wind tunnel in the Wind Energy Laboratory at the University of Wisconsin-Milwaukee (UWM) was used for the experimental study. A photograph of the wind tunnel is shown in Figure 4-1. Welsh [41] provides a detailed description of the wind tunnel facility and the design considerations, but a general synopsis is provided here.



Figure 4-1. Wind tunnel at UWM

4.1 Layout and Description

The wind tunnel at UWM is an open-circuit, suction type tunnel that uses an axial fan to draw air through the test section. The inlet settling chamber section was designed with a 7.62 cm long honeycomb and 1 cm hexagonal shaped cells to reduce the large scale turbulence and to eliminate mean lateral and vertical velocity components. A series of screens with reduced mesh sizes was incorporated to reduce further the turbulence and reduce the variation in the mean longitudinal velocity.

The room is temperature controlled which reduces the variation in temperature during testing. Temperature variations with the wind turbine operating continuously for up to 10 hours were less than 0.5 C. The inlet to the contraction section is a little over 9.3 square meters and transitions to the 1.4 square meter test section in ~4 m distance. The 6.2 contraction ratio is on the low end of the recommended range, but given the low wind tunnel speed, it was deemed acceptable. The test section is ~120 cm × 120 cm × 243 cm long and has clear polycarbonate walls to provide a

smooth surface. The wind tunnel boundary layer was not measured for this experimentation, but it was estimated to be less than 15 cm in 2.4 m so that the boundary layer does not extend into the turbine wake. The diffuser section was designed with a 2.25 expansion ratio and a 2.5° expansion angle. The diffuser section transitions from a square cross section at the exit of the test section to an octagonal shape at the entrance to the 1.83 m fan diameter. A rubber coupling was installed between the diffuser and the fan to reduce vibration and prevent measurement errors. The six-bladed fan is attached to a 34 hp motor which is controlled by a variable frequency motor speed drive mounted to the side of the fan enclosure. The motor frequency and resulting wind speed were established during this experimentation and the results are discussed in Section 6.1.

4.2 Traverse System

Inside the wind tunnel test section, a 3-axis traverse system is mounted on the top panel. Stepper motors are attached to each arm to allow the hot wire probe to be positioned accurately upon command. With stepper motors set to the absolute zero position for each axis, the vertical arm is located 33 cm from the inlet of the test section and 8.4 cm from the wall opposite the entry door. The maximum measurement length along the axis of the wind tunnel is limited to 148.5 cm by the stops on the traverse. Each stepper motor provides 25.4 mm of movement for each 4000 revolutions giving a $6.35 \mu\text{m}$ resolution on the position of the hot wire probe. The stepper motors were driven by a Velmex VXM controller and communication between the DAQ PC and the controller was performed via RS232. A LabVIEW virtual instrument module was provided by Velmex and used to automate many of the measurements. A separate LabVIEW virtual instrument was created to position the traverse to the desired measurement locations and differs from the instrument established by Welsh [41] in that it allows the time series of the velocity

signal to be recorded. The block diagram of the LabVIEW instrument created to acquire velocity measurements is shown in Appendix A.

4.3 Data Acquisition and Instrumentation

As mentioned in the previous section, LabVIEW software was used for all data acquisition. New virtual instruments were developed for positioning the traverse during experiments, acquiring data, and calibrating hot-wire probes. The instruments have been used for several research projects at UWM including a study of the flow around an Ahmed body [42] and evaluation of slotted wind turbine blade designs [43]. The LabVIEW instruments are discussed in Appendix A.

4.3.1 Hot Wire Probe

The Dantec Model 55P64 miniature wire probe, shown in Figure 4-2, was used for velocity measurement. It is a dual sensor, cross-wire (e.g. X-wire) type probe designed to measure U and V components of the velocity vector.

Figure 4-2. Dantec Model 55P64 hot wire probe

The probe wires are aligned such that they are in the same plane as the mean flow, as shown in Figure 4-3; however, the axis of the probe was perpendicular to the flow.

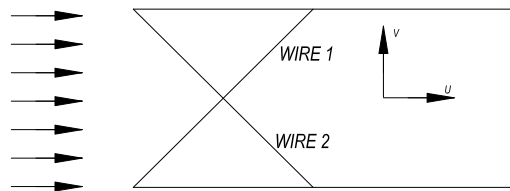


Figure 4-3. Hot-wire probe wire orientation

The 55P64 has two platinum-plated tungsten, 5 mm diameter, wires welded to the probe at 45° to each other and can measure velocity components within a $\pm 45^\circ$ cone. The probe is capable of measuring velocity between 0.05 m/s to 500 m/s. Two Dantec 54T30 Miniature Constant

Temperature Anemometers (CTA's) were used to provide a 0-5 V analog output voltage based on the characteristics of the probe. The offset voltage on each wire was approximately 1.3 V at zero velocity. A more detailed discussion of hot-wire anemometry used for this research is provided in Chapter 5.

4.3.2 DAQ Hardware

The data acquisition (DAQ) system consisted of a National Instruments (NI) cDAQ 9172 Chassis connected to the USB port of a PC. Anemometer output voltage cables were connected to a NI-9215 I/O module with 4 BNC analog input channels. The NI-9215 offers 16-bit resolution that resulted in approximately $7.6E-5$ V measurement resolution for the velocity signal based on a 0-5V output from the anemometer.

4.3.3 Air Temperature

For hot wire calibration, the thermistor inside the hot wire calibrator was used to measure the calibration air temperature; this is discussed further in Chapter 5. For measurements taken during experiments, the air temperature was monitored using a Fluke 80BK-A temperature probe combined with a Fluke 87V digital multimeter (DMM). The accuracy of the temperature probe is published as the greater of ± 2.2 °C or 2% of 0-260 °C. The temperature measurement from the 80BK-A was correlated to the temperature measurement from the hot wire thermistor so that the proper correction factors could be applied during data processing.

4.3.4 Blade Rotation Speed

The blade rotation speed was measured using a Monarch Model PLT200 laser tachometer mounted on a tripod. The tachometer has a LCD display for a direct reading, in RPM, and also provides a TTL pulse output where the frequency can be read with a digital multi-meter (DMM). The accuracy of the tachometer is listed at 0.01% of reading. To verify the tachometer output, a

special turbine was built with a 14-tooth gear attached to the turbine blade; the gear tooth rotation was measured with a Honeywell LCZ260 Hall-effect sensor as shown in Figure 4-4. As each gear tooth passes the sensor, the sensor delivers a square wave voltage signal with a frequency proportional to the blade rotation speed.

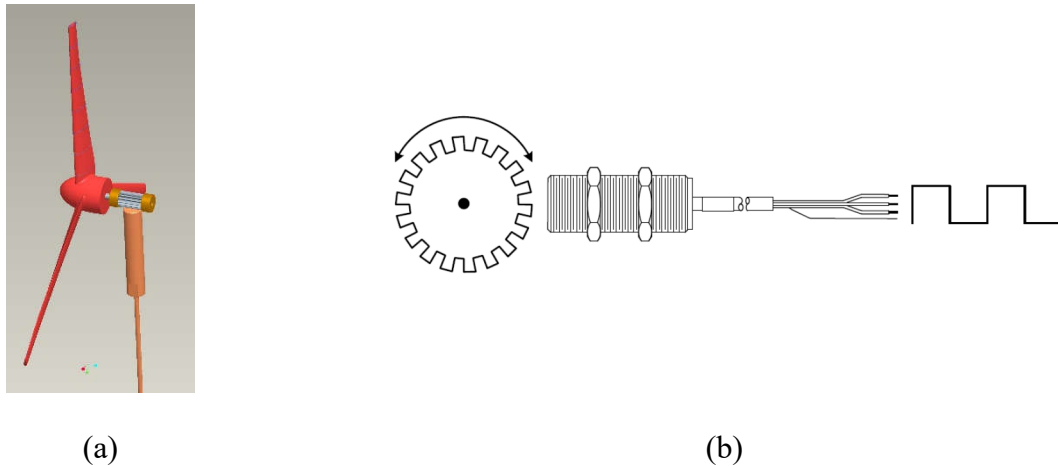


Figure 4-4. Blade rotational speed measured with Hall-effect sensor (a) CAD layout of sensor (b) operation of sensor showing square wave output

A small piece of reflective tape was attached to the hub of the turbine blade to provide feedback for the laser tachometer. With the turbine placed in the wind tunnel, the rotational speed was recorded from the tachometer display at several different velocities. A DMM was used to measure the hall-effect sensor frequency. The rotational speed was calculated from the frequency of the hall-effect sensor and the number of gear teeth. Table 4-1 shows excellent agreement between the two different measurement methods.

Table 4-1. Comparison of blade rotational speed using tachometer and hall-effect sensor.

| Drive Frequency Setting | Estimated Velocity | DMM Measured Frequency-Hall Effect Sensor | Calculated From Hall Effect Sensor-14 Gear Teeth | Measured From Monarch PLT200 Tachometer |
|-------------------------|--------------------|---|--|---|
| [Hz] | [m/s] | [Hz] | [RPM] | [RPM] |
| 10 | 2.89 | 158 | 678 | 677 |
| 15 | 4.47 | 267 | 1143 | 1142 |
| 20 | 6.06 | 373 | 1599 | 1600 |
| 30 | 9.23 | 613 | 2627 | 2630 |

5 Hot Wire Anemometry

Hot wire anemometry (HWA) has been used for many years to measure velocity fluctuations in turbulent flows. It is well suited for turbulent flow studies in low Reynolds number air/gas flows with low to moderate turbulent intensities (<25%). It has the advantage of being much lower cost compared to Particle Image Velocimetry (PIV), Laser Doppler Anemometry (LDA), or Planar Laser-Induced Fluorescence (PLIF) systems and does not require particulate in the flow that could contaminate the components of a wind tunnel. HWA is relatively easy to use, provides a continuous analog output, meaning no information is lost, and has an excellent temporal resolution for spectral measurements.

Within the last decade, research on hot wire anemometry has included studies on data reduction methods [44], improving measurement accuracy [45] calibrating with different fluid properties [46], and measurement techniques [47], [48], [49], [50]. In principle, hot wire anemometry is used to measure local velocity by placing a heated, fine wire into a flow stream and controlling the wire current that corresponds to the convective heat loss in the wire. Thus, hot wire anemometry has two components: a probe containing the heated wire and an anemometer which contains the necessary electronic components to control the wire current (i.e. wire temperature) and produce a conditioned measurement signal that is proportional to the velocity.

Hot-wire probes are available, commercially, in a variety of styles and can include multiple wires to measure the velocity in multiple axes. In general, the number of wires in the probe corresponds to the number of velocity components being measured. The hot wire probe used for this research was described in Chapter 4. The wire for the probes can be made from different materials and with different plating; both affect the heat transfer rate and the response of the probe.

Hot wire anemometers are commonly made in two forms: a constant current type and a constant temperature type. Both types rely on the same physical principle in that the energy generated within the wire is balanced by the convective heat loss from the flow. For equilibrium conditions, we can write an energy balance for the wire as

$$I_w^2 R = hA_w(T_w - T_\infty) \quad (5.1)$$

In the constant current type, the heat generated in the wire, $I_w^2 R$, is held constant and the wire temperature, T_w , must be adjusted by the anemometer circuitry. In the constant temperature type, the wire current is adjusted to maintain a constant wire temperature.

5.1 Constant Temperature Anemometer

Constant temperature anemometers (CTA) were used in this research. A simplified schematic of an anemometer is shown in Figure 5-1 and the operation is based on a Wheatstone bridge where the V_{A-B} voltage is balanced with V_{C-D} with an operating current, I_{bridge} .

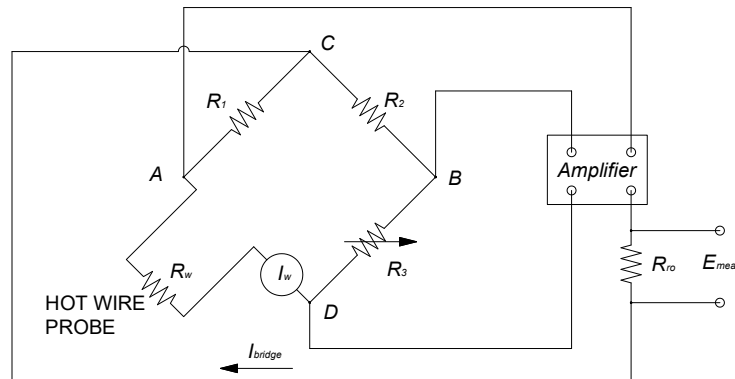


Figure 5-1 Simplified hot wire anemometer circuit

The decade resistance, R_3 , is adjusted to set the bridge operating current that sets the operating wire current, I_w , and wire operating temperature. The other resistances, R_1 and R_2 , are based on the resistances of the probe, probe support, cables, wire, and the bridge ratio of the anemometer. As the resistance of the hot wire changes with velocity fluctuations, the bridge voltage is upset,

and a feedback circuit (amplifier) adjusts the bridge current to maintain a constant wire temperature. A readout resistor senses the current changes and the wire voltage signal can be read from the DAQ or other measurement device.

5.2 Overheat Adjustment

Setting the desired wire operating temperature is critical for calibration and velocity measurements. The wire temperature setting is determined based on the probe manufacturer's recommendations to prevent the wire from burning out while maintaining optimum sensitivity to velocity changes. If the wire temperature is set too high, the wires could burn out prematurely. Setting the wire temperature too low could result in a loss of sensitivity for turbulence measurements. Failure to account for differences in temperature between calibration and experimentation can lead to significant error in the measurements.

The wire operating temperature is set through a process called overheat adjustment where the decade resistance is calculated from values of the wire temperature coefficient of resistance (TCR), sensor resistance, sensor lead resistance, support resistance, flow temperature, and desired operating wire temperature. Figure 5-2 and Figure 5-3 show snapshots of the spreadsheet used for calculating the decade resistance and dip switch settings in the CTA. The equations used in the calculations are described in the CTA user's guide [51]. Both wire temperatures for this research were set to 250 C based on the manufacturer's recommendation. For wire 1, the decade resistance was set to 143.3Ω and for wire 2 the decade resistance was set to 150.6Ω .

Mini-CTA type 54T30, 54N80, 54N81 and 54N82: Selecting and adjusting overheat. **9054S4016**
Org. 980528/TSV
Rev. 100531/MHA
DMS no. 4867v7

Probe identification 55P64 ch.1 -

Insert probe specific parameters etc.

| | | |
|-----------------------------|------------------------|--------------------------------|
| Sensor resistance, R_{20} | 3.30 Ω | See probe box |
| Sensor lead resist., RL | 0.50 Ω | 55P11/61 family |
| Support resistance, R_s | 0.40 Ω | Non standard |
| Cable resistance, R_c | 0.60 Ω | Non standard |
| Sensor TCR, α_{20} | 0.36% /K | Standard tungsten |
| Desired wire temp., T_w | 250 $^{\circ}\text{C}$ | Wire mean temperature |
| Temperature of flow | 20 $^{\circ}\text{C}$ | Temperature during measurement |

Click box below to select resistance range.
(Check label on the Mini-CTA for actual range!)
4-20 Ohms (Standard: 4-20 ohms)

Calculated wire operating resistance etc.

| | |
|------------------------------|------------------------|
| Over temperature, ΔT | 230 $^{\circ}\text{C}$ |
| Operating resist., R_w | 6.03 Ω |
| Total resistance, R_T | 7.53 Ω |
| Overheat ratio, a | 0.83 |
| Bridge ratio, M | 1:20 |
| Decade resistance, R_D | 150.6 Ω |

Set decade controls as follows:
(grey dot indicates switch in down position)

Figure 5-2. Dantec 54T30 Mini-CTA setting for wire 1

Mini-CTA type 54T30, 54N80, 54N81 and 54N82: Selecting and adjusting overheat. **9054S4016**
Org. 980528/TSV
Rev. 100531/MHA
DMS no. 4867v7

Probe identification 55P64 ch.1 -

Insert probe specific parameters etc.

| | | |
|-----------------------------|------------------------|--------------------------------|
| Sensor resistance, R_{20} | 3.10 Ω | See probe box |
| Sensor lead resist., RL | 0.50 Ω | 55P11/61 family |
| Support resistance, R_s | 0.40 Ω | Non standard |
| Cable resistance, R_c | 0.60 Ω | Non standard |
| Sensor TCR, α_{20} | 0.36% /K | Standard tungsten |
| Desired wire temp., T_w | 250 $^{\circ}\text{C}$ | Wire mean temperature |
| Temperature of flow | 20 $^{\circ}\text{C}$ | Temperature during measurement |

Click box below to select resistance range.
(Check label on the Mini-CTA for actual range!)
4-20 Ohms (Standard: 4-20 ohms)

Calculated wire operating resistance etc.

| | |
|------------------------------|------------------------|
| Over temperature, ΔT | 230 $^{\circ}\text{C}$ |
| Operating resist., R_w | 5.67 Ω |
| Total resistance, R_T | 7.17 Ω |
| Overheat ratio, a | 0.83 |
| Bridge ratio, M | 1:20 |
| Decade resistance, R_D | 143.3 Ω |

Set decade controls as follows:
(grey dot indicates switch in down position)

Figure 5-3. Dantec 54T30 Mini-CTA setting for wire 2

5.3 Calibration Velocity

Using hot wire anemometry for flow measurements requires a reliable and repeatable method of establishing a calibration velocity. In many cases, a nozzle with a large contraction ratio is used where the calibration velocity is established at the outlet of the nozzle. Bremhorst and Listijono [52] describe the static pressure consequence of using a nozzle or pitot tube and failure to correct

for the static pressure can lead to significant velocity calibration error. The equipment used to establish a calibration velocity for this research is shown in Figure 5-4.

5.4 Dantec 54H10 Hot Wire Calibrator

A Model 54H10 Hot-Wire Calibrator from Dantec Dynamics [53] was used to provide a uniform free jet to the hot-wire probe. The calibration velocity was based on isentropic relations and known geometry of an internal, low turbulence, nozzle. Stannov [54] describes a similar calibrator that includes more automated features to reduce the calibration time. The 54H10 included a 2-axis rotation probe support holder for measurements at different yaw angles.

In 2-point mode, the 54H10 could be set to provide a calibrated velocity at either 1.6 m/s or 50 m/s with the velocity dependent on the position of the two-way valve (“LOW” or “HIGH), the air temperature, as measured by an internal thermistor, and the ambient atmospheric pressure.

The 54H10 was modified, according to Dantec’s instructions, to use in continuous mode where the differential pressure across the exit nozzle could be adjusted to vary the calibration velocity.

A Fluke Model 922 Airflow Meter/Micromanometer was used to measure the differential pressure across the internal nozzle of the hot-wire calibrator. The micromanometer has a published 4000 Pascal (Pa) differential pressure range with 1 Pa resolution and $\pm 1\%$ of reading +1 Pa accuracy. The Airflow Meter/Micromanometer was purchased as a kit that also included a 30.5 cm long pitot tube for air velocity measurement. With the pitot tube attached to the micromanometer, the air velocity measurement range was published as 1-80 m/s with 0.001 m/s resolution and 2.5% of reading accuracy.

The 54H10 has an internal thermistor to measure the air temperature within the calibrator. The resistance of the thermistor was measured using a Fluke Model 87 Multimeter, which has a published accuracy of 0.05%+2 Ω in the range of resistances of the thermistor. Barometric

pressure (nozzle exit pressure) was measured using a Conex Electro Systems Model JDB1 digital barometer. The JDB1 barometer has an accuracy of ± 0.05 inHg [$\sim 0.2\%$ FS] and a resolution of 0.01 inHg. The JDB1 barometer was calibrated against the barometric pressure listed at General Mitchel International Airport by the NOAA (<http://w1.weather.gov/obhistory/KMKE.html>).

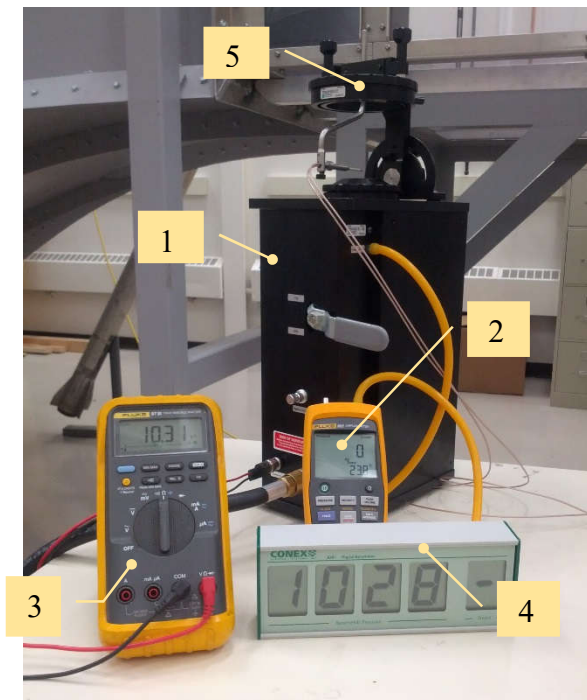


Figure 5-4 Benchtop equipment used to calibrate the hot wire sensors: Dantec 54H10 calibrator (1), Fluke Model 922 Micromanometer (2), Fluke Model 87 Multimeter (3), and Conex JDB1 Digital Barometer (4), 2-Axis Probe Support Holder (5)

Dantec provided an Excel® spreadsheet to use with the 54H10 calibrator where the calibration velocity is determined from user input for the barometric pressure, thermistor resistance, nozzle differential pressure, and measured wire voltages at various differential pressure settings. An image of the spreadsheet is shown in Figure 5-5. The spreadsheet calculates the coefficients of a 4th order polynomial curve fit for converting wire voltage to velocity; however, the spreadsheet

was cumbersome, time consuming, and impractical to use. This was especially true for calibration at different yaw angles.

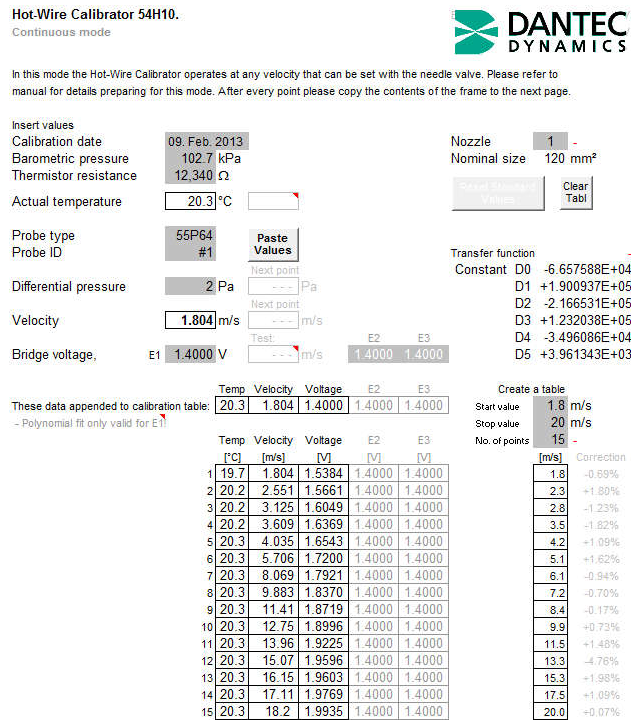


Figure 5-5. Sample hot-wire calibration from spreadsheet supplied by Dantec Dynamics

To reduce the time required for calibration, a LabVIEW instrument was created to read the hot wire voltages with user input for the thermistor resistance, nozzle differential pressure, yaw angle, barometric pressure, and ambient temperature. The data was stored in a text file with each measurement appended to the file. A MATLAB script, *hwcal2.m*, was developed to read the table of calibration data and compute the calibration velocity based on acquired average wire voltages and user input for barometric pressure, thermistor resistance, nozzle differential pressure, yaw angle, and ambient temperature. The MATLAB script is listed in Appendix B and the LabVIEW instrument to build the hot wire calibration tables is shown in Appendix A.

5.4.1 Isentropic Flow Relations and Static Pressure Correction

Similar to the Dantec spreadsheet, the calibration velocity was calculated in the MATLAB script based on isentropic flow relations through a nozzle as described in [54]:

$$\frac{P_o}{P} = \left[1 + \frac{\gamma-1}{2} M^2 \right]^{\frac{\gamma}{\gamma-1}} \quad (5.2)$$

$$\frac{a_o^2}{a^2} = 1 + \frac{\gamma-1}{2} M^2 \quad (5.3)$$

$$a_o = \sqrt{\gamma R T_o} \quad (5.4)$$

where the subscript designates stagnation conditions and no subscript identifies static conditions.

With the definition of the Mach number, M , the equations can be rearranged to solve for the calibration velocity, U_{cal} :

$$M = \sqrt{2 \left[\left(\frac{P_o}{P} \right)^{\frac{\gamma-1}{\gamma}} - 1 \right] / (\gamma - 1)} \quad (5.5)$$

$$a = \sqrt{a_o^2 / \left(1 + \frac{\gamma-1}{2} M^2 \right)} \quad (5.6)$$

$$U_{cal} = Ma \quad (5.7)$$

The above equations are ideal and assume no loss of energy in the stream-wise direction. In reality, corrections need to be made based on the location of the nozzle differential pressure measurement and dissipation of turbulent energy in the nozzle. A small correction is made to the stagnation pressure to account for the dissipation of kinetic energy in the contraction so the corrected stagnation pressure, P'_o , becomes

$$P'_o = P_o + 0.5 \rho_o U_o^2 \quad (5.8)$$

with the chamber velocity, U_o , and chamber density, ρ_o , determined from knowledge of the nozzle contraction ratio, C_N , nozzle exit area, A_N , nozzle inlet area, A_o , and a nozzle-dependent factor, K_{FR} :

$$U_o = \frac{U_{cal}}{C_N} = \frac{U_{cal}A_N}{A_o} \cdot (K_{FR}) \quad (5.9)$$

$$\rho_o = \frac{P_o}{RT} = \frac{P_a + \Delta P}{RT} \quad (5.10)$$

$$T = \frac{1}{A + B \ln(R_t) + C (\ln(R_t))^3} \quad (5.11)$$

For the specific model of 54H10, the nozzle exit area was based on a 12.4 mm exit diameter and the nozzle inlet area was based on a 63 mm inlet diameter. The nozzle-dependent factor was constant at $K_{FR}=0.97$. In equation (5.10), R is the gas constant for air, P_a is the measured atmospheric pressure at the nozzle exit, ΔP is the measured nozzle differential pressure, and T is the temperature. The temperature is computed from the thermistor resistance, R_t , using the Steinhart-Hart equation (5.11) with constants $A = 1.12822 E - 3$, $B = 2.34289 E - 4$, and $C = 8.69243 E - 8$.

A correction is also made to the static pressure in equation (5.10) where the corrected static pressure is

$$P' = P + C_f \Delta P \quad (5.12)$$

where the correction factor, C_f , was interpolated from empirical data provided by Dantec.

5.5 Hot-Wire Calibration Methods

Experimental work performed over the years has led to a number of different methods for calibrating hot wire anemometers with inclined wires. The literature on hot wire anemometry is extensive and covers a wide variety of topics. Brown, et al [55] provide a comprehensive list of

methods developed to account for longitudinal cooling and yaw angle sensitivity. One method that has not been researched is the use of a biharmonic spline interpolation algorithm, developed by Sandwell [56] for constructing ocean floor topography maps from satellite data. The algorithm has also been used for mapping the total electron content of the ionosphere from GPS data [57]. The algorithm is well suited for hot wire anemometry where measurements at different yaw angles and calibration velocities could be irregularly spaced. The algorithm has been implemented in the MATLAB *griddata.m* function with the ‘-v4’ method option. Only a few researchers have even implemented the *griddata.m* function for hot wire anemometry. Chemoray and Hjarne [58] used the *griddata.m* function in their research on multi-hole pressure probes and claimed 1.63% statistical uncertainty with 99% confidence for mean velocity measurements. Burrattini and Antonia [59] concluded that an effective angle method was less reliable than a look-up-table approach where the cubic interpolation option in the *griddata.m* function was designated as a look-up-table. For this research, the biharmonic interpolation algorithm, sometimes referred to as a surface interpolation, is compared to two other traditional methods of hot wire calibration. The three different methods for converting hot wire anemometer voltages to velocities were examined for accuracy and computation time.

5.5.1 Effective Angle Method

The first method examined for calibrating the hot-wire anemometers is outlined in the Dantec literature [60] for hot wire turbulence measurements. It is based on the effective angle method that is described by numerous researchers and detailed in text books by Bruun [61], Perry [62], and Bradshaw [63]. In this approach, the effective velocity is expressed as

$$V_{eff} = \tilde{V}f(\theta_{eff}) \quad (5.13)$$

where \tilde{V} is the magnitude of the velocity vector and $f(\theta_{eff})$ is a function that describes the dependency on the yaw angle and other factors. The effective angle is the angle between the velocity vector and the wire that satisfies equation (5.13). Several functions are presented in the textbooks with one of the more popular functions being:

$$f(\theta) = (\cos^2\theta + k^2\sin^2\theta)^{0.5} \quad (5.14)$$

where the yaw correction factor, k^2 , accounts for cooling effects along the axis of the wire. It is known that the effective angle can vary with velocity and yaw angle; however, Brown, et. al. [55] concluded that the effective angle can be assumed constant in flows with low turbulence intensity without introducing significant errors. Chew and Ha [64] determined that the yaw correction factor for a single wire cannot be used for multiple wire probes and resolved that the yaw correction factor can be assumed constant with little error over a wide range of yaw angles. Bakken and Krogstad [65] developed a velocity dependent effective angle method for low velocities (0.5-6 m/s) and showed an improvement in the measurement of Reynolds stresses. For method comparison in this research, the effective angle was assumed to match the geometric angle of 45° and the yaw correction factor, k^2 , for each wire was assumed constant and set to the manufacturer's default value. In the effective angle method, it was first necessary to establish a relationship between a known (calibration) velocity and the anemometer voltage with the probe normal to the flow (zero degree flow angle).

5.5.1.1 Power Law Fit

Two techniques are commonly used with the most publicized technique being a power law relationship and is expressed as

$$E^2 = A + B \cdot U_{cal}^n \quad (5.15)$$

where E is the anemometer voltage output, U_{cal} is the calibration velocity, and A , B , and n are constants determined from a linear fit of measured anemometer voltage at calibrated velocity settings. Bruun, et al. [66] investigated values of A , B , and n in for various hot wire probes and presented a summary of alternate power law relationships and polynomial relationships. The power law relationship in equation (5.15) has its origin in research by King [67] and is based on heat transfer from an infinite wire in an incompressible, low Reynolds number flow. In his research with small diameter wires, King showed a relationship between the Nusselt number, Nu , and Reynolds number, Re :

$$Nu = C_1 + C_2 \cdot Re^{1/2} \quad (5.16)$$

where C_1 , C_2 are constants. From this, the convective film coefficient can be expressed as a function of the velocity, U , as

$$h = C'_1 + C'_2 \cdot U^{1/2} \quad (5.17)$$

As a result, the power law relationship is often referred to as King's Law when $n=0.5$.

Incorporating this into the energy balance from equation (5.1) and accounting for other resistances in the anemometer circuit relates the anemometer voltage to velocity. Bruun [66] has shown the velocity exponent, n , in equation (5.15) will have a better fit with values between 0.40 and 0.45 instead of the 0.50 established through heat transfer laws. In a conventional power law calibration, the value of n is iterated as constants A and B are determine from a linear fit at each iteration of n . The value of n and the resulting A and B constants are selected such that the residual sum of squares (SSE) is a minimum.

Swaminathan, et al. [68] developed a calibration method to determine A , B , and n by expressing the non-linear power law equation as a Taylor Series expansion about initial estimates of A , B , and n . The resulting linear equations were solved using an iterative Newton-Raphson technique.

Convergence was achieved when changes in A , B , and n became negligible. Using calibration data from three different probes, the method was shown to reduce the SSE by 4-14% compared to the method of minimizing SSE by just iterating n . For this research, the conventional method of iterating n was used where

$$SSE = \sum_1^N (E_i^2 - E_{fit}^2)^2 \quad (5.18)$$

Figure 5-6 shows the output of a MATLAB script, *powerlaw_cal.m*, which determines the minimum value of the coefficient n that minimizes the SSE using equation (5.18). Figure 5-7 shows the curve fit using the minimized values of n for each wire.

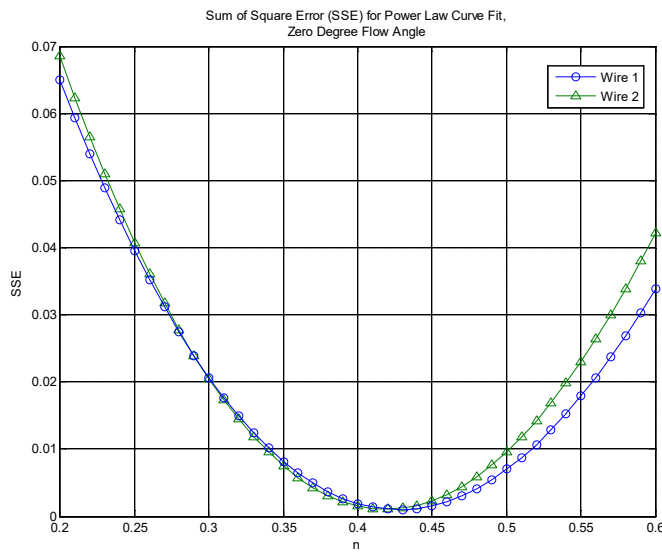


Figure 5-6. Residual sum of squares error (SSE) in determining n values for power law curve fit

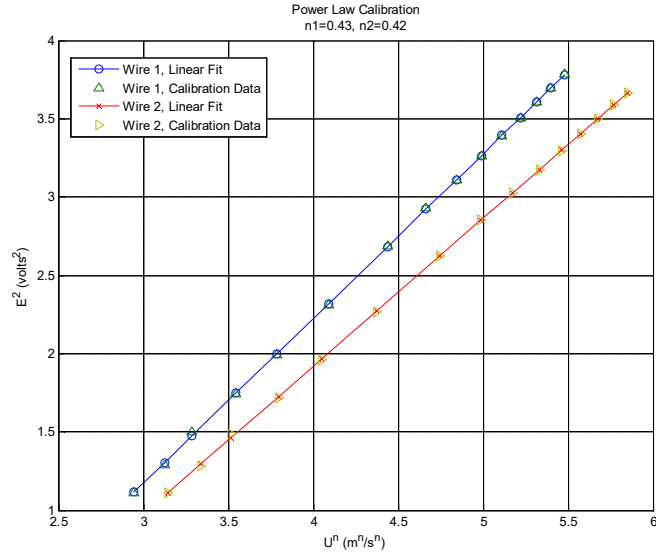


Figure 5-7. Power law curve fit from Equation (5.15)

5.5.1.2 Fourth Order Polynomial Fit

The second technique for relating anemometer voltage to calibration velocity uses a 4th order polynomial fit for each wire:

$$U_{cali} = C_{0i} + C_{1i} \cdot E_{ci} + C_{2i}E_{ci}^2 + C_{3i}E_{ci}^3 + C_{4i}E_{ci}^4 \quad (5.19)$$

where E_{ci} is the anemometer voltage output, corrected for temperature for the i^{th} wire, U_{cali} is the calibration velocity, and $C_{0i}-C_{4i}$ are coefficients of the polynomial. This polynomial fit uses the method of least squares to determine the coefficients and is easily programmed. The drawback of the polynomial fit method is it can be unstable when extrapolating for velocity measurements outside the calibrated velocity range. Figure 5-8 shows the resulting polynomial curve fit using the same calibration data from the power law fit.

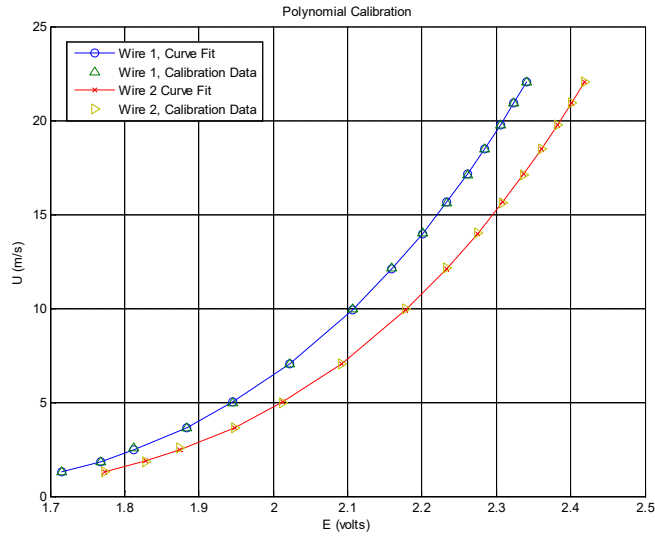


Figure 5-8. Hot wire calibration using a 4th order polynomial curve fit

For comparative purposes, the accuracy of each method can be described by the normalized standard deviation over all velocity values:

$$\epsilon_N = \left[\frac{1}{N} \sum_{i=1}^N \left(1 - \frac{U_{fit}}{U_{cali}} \right)^2 \right]^{1/2} \quad (5.20)$$

where U_{fit} is the velocity calculated from either the power law or the polynomial method and U_{cali} is the calibration velocity. Table 5-1 summarizes the constants and normalized standard deviation for three calibration files using three different Dantec 55P64 hot-wire probes. All calibrations performed showed the polynomial curve fit to be slightly more accurate than the power law calibration.

Table 5-1 Summary of calibrations from three different Dantec 9055P064 probes using power law and polynomial fit methods

| Constant | Probe #1 | | Probe #2 | | Probe #3 | |
|-----------------|---------------|---------------|---------------|---------------|---------------|---------------|
| | Wire 1 | Wire 2 | Wire 1 | Wire 2 | Wire 1 | Wire 2 |
| A | 0.9511 | 1.0584 | 0.6994 | 0.6724 | 0.8755 | 0.9512 |
| B | 1.8833 | 1.9686 | 1.5036 | 1.4211 | 1.9901 | 2.0959 |
| n | 0.43 | 0.42 | 0.45 | 0.45 | 0.45 | 0.44 |
| ϵ_{NA} | 0.0128 | 0.0124 | 0.0041 | 0.0048 | 0.0148 | 0.0149 |
| C ₀ | 4.854 | -0.291 | 25.348 | 22.675 | 3.160 | -4.555 |
| C ₁ | -12.535 | 27.847 | -146.392 | -122.613 | 2.106 | 65.295 |
| C ₂ | 1.373 | -124.228 | 349.794 | 279.794 | -47.557 | -246.374 |
| C ₃ | 17.752 | 194.044 | -393.180 | -304.611 | 91.499 | 370.476 |
| C ₄ | -11.959 | -104.575 | 169.621 | 127.966 | -53.839 | -200.079 |
| ϵ_{NB} | 0.0126 | 0.0120 | 0.0039 | 0.0039 | 0.0100 | 0.0086 |

With the effective angle approach and the effective angle set to match the geometric 45° wire angle, intermediate velocities are calculated based on the wire coordinate system as

$$U_1 = \frac{\sqrt{2}}{2} \sqrt{(1 + k_2^2)U_{cal2}^2 - k_2^2U_{cal1}^2} \quad (5.21)$$

$$U_2 = \frac{\sqrt{2}}{2} \sqrt{(1 + k_1^2)U_{cal1}^2 - k_1^2U_{cal2}^2} \quad (5.22)$$

The final velocity magnitudes and velocity angle, based on the probe coordinate system are calculated from:

$$\tilde{U} = \frac{\sqrt{2}}{2} U_1 + \frac{\sqrt{2}}{2} U_2 \quad (5.23)$$

$$\tilde{V} = \frac{\sqrt{2}}{2} U_1 - \frac{\sqrt{2}}{2} U_2 \quad (5.24)$$

$$\alpha_f = \tan^{-1} \left(\frac{\tilde{V}}{\tilde{U}} \right) \quad (5.25)$$

The manufacturers default values for the yaw coefficients [51] were $k_1^2=k_2^2=0.04$. The MATLAB script *error_eff_angle.m* for computing power law coefficients, polynomial coefficients, velocities and normalized standard deviation are shown in Appendix B.

5.5.2 Polynomial Surface Fit

The second HWA calibration method investigated was based on a surface fit method developed by Oster and Wygnanski [69] and is termed a ‘full calibration’ method because it accounts for yaw angle effects in the calibration. In this method hot-wire measurements are taken at multiple calibration velocity settings and various yaw angles. The data is fit to a 3rd order polynomial surface, and separate polynomial equations are developed for the velocity magnitude and velocity angle. For the polynomial surface fit calibration, data was recorded for 45 different velocity settings with the yaw angle varied between -40° and 40° in 10° increments.

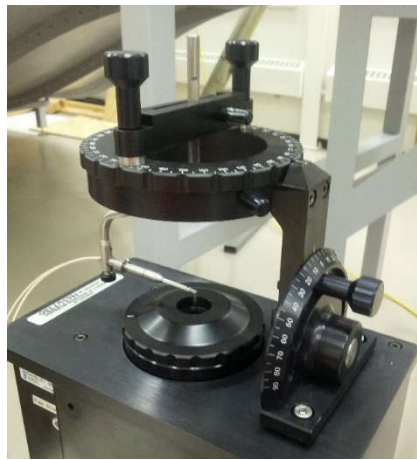


Figure 5-9. Hot wire calibration fixture shown at zero yaw angle.

Note that this data was taken with the probe installed in the calibrator, as shown in Figure 5-9, using the same cables and same probe support as when running wind turbine experiments. Using the same cables and probe support was necessary to eliminate additional uncertainty due to differences in probe support and cable resistances. The calibrator was positioned on a table adjacent to the wind tunnel access door.

Oster and Wygnanski [69] showed that for an X-wire probe there is a unique set of voltages, E_1 , and E_2 , that corresponds to the velocity magnitude and the velocity angle. Figure 5-10 and

Figure 5-11 show 3-dimensional representations of the calibration velocity and angle as a function of the wire voltages for 15 of the 45 velocity settings.

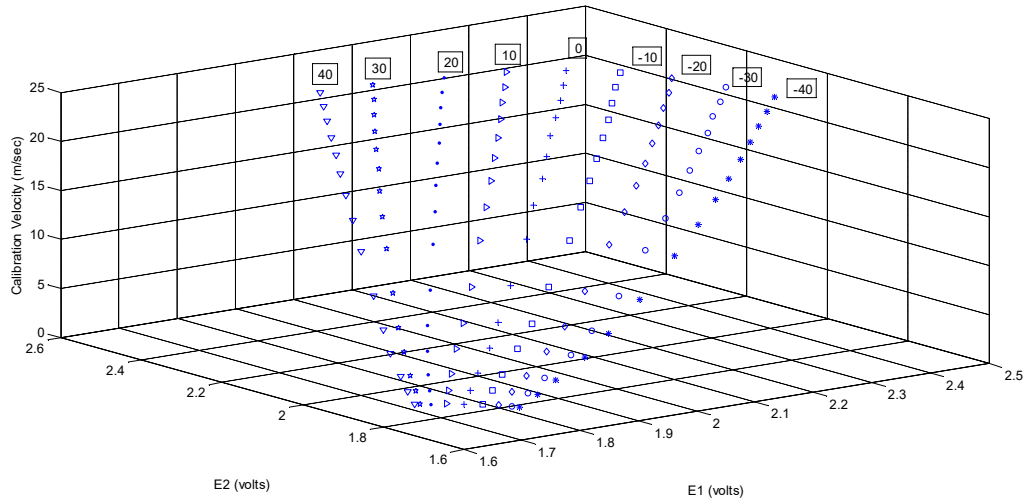


Figure 5-10. Calibration velocity at different yaw angles.

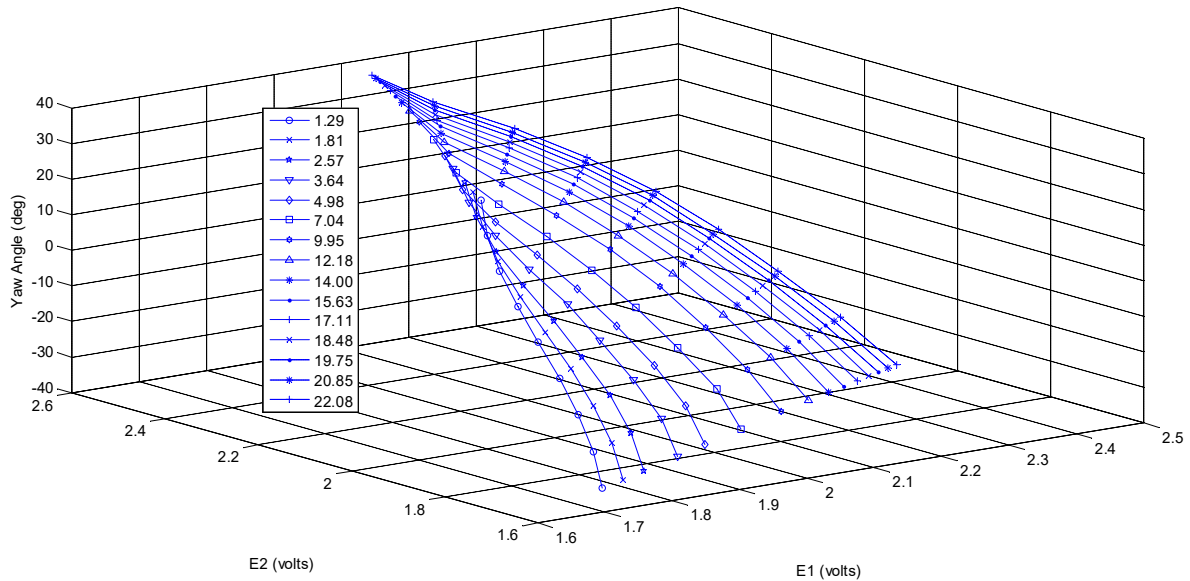


Figure 5-11. Yaw angle at different velocity settings (m/s).

For both velocity, U , and angle, α , the data was fit to 3rd order polynomial surfaces using the following equations:

$$U = a_0E_1^3 + a_1E_1^2E_2 + a_2E_1E_2^2 + a_3E_2^3 + a_4E_1^2 + a_5E_1E_2 + a_6E_2^2 + a_7E_1 \quad (5.26)$$

$$+ a_8E_2 + a_9$$

$$\alpha = b_0E_1^3 + b_1E_1^2E_2 + b_2E_1E_2^2 + b_3E_2^3 + b_4E_1^2 + b_5E_1E_2 + b_6E_2^2 + b_7E_1 + \quad (5.27)$$

$$b_8E_2 + b_9$$

For each variable, the method of least squares was used to determine the coefficients $a_0 \dots a_9$ and $b_0 \dots b_9$. Taking the velocity variable, as an example, and letting q be the residual sum of the squares (SSE) of the difference between the calibrated velocity, U_{cal} , and the surface fit velocity, U , the goal is to minimize q for all data points.

$$q(a_0, a_1, a_2 \dots a_9) = \sum_{j=1}^n (U_{calj} - U(E_1, E_2)_j)^2 \quad (5.28)$$

The necessary and sufficient conditions for q to be a minimum are:

$$\frac{\partial q}{\partial a_0} = 0; \quad \frac{\partial q}{\partial a_1} = 0; \quad \frac{\partial q}{\partial a_2} = 0; \quad \dots \quad \frac{\partial q}{\partial a_9} = 0 \quad (5.29)$$

$$\frac{\partial q}{\partial a_0} = \sum 2(U_{calj} - a_0E_{1j}^3 - a_1E_{1j}^2E_{2j} - a_2E_{1j}E_{2j}^2 - a_3E_{2j}^3 - a_4E_{1j}^2 - \quad (5.30)$$

$$a_5E_{1j}E_{2j} - a_6E_{2j}^2 - a_7E_{1j} - a_8E_{2j} - a_9)(-E_{1j}^3) = 0$$

.....

$$\frac{\partial q}{\partial a_9} = \sum 2(U_{calj} - a_0E_{1j}^3 - a_1E_{1j}^2E_{2j} - a_2E_{1j}E_{2j}^2 - a_3E_{2j}^3 - a_4E_{1j}^2 - \quad (5.31)$$

$$a_5E_{1j}E_{2j} - a_6E_{2j}^2 - a_7E_{1j} - a_8E_{2j} - a_9)(-1) = 0$$

Solving and separating terms yields a set of 10 equations and 10 unknown coefficients (only two are shown here for brevity):

$$\begin{aligned}
& a_0 \sum E_{1j}^6 + a_1 \sum E_{1j}^5 E_{2j} + a_2 \sum E_{1j}^4 E_{2j}^2 + a_3 \sum E_{1j}^3 E_{2j}^3 + a_4 \sum E_{1j}^5 + & (5.32) \\
& a_5 \sum E_{1j}^4 E_{2j} + a_6 \sum E_{1j}^3 E_{2j}^2 + a_7 \sum E_{1j}^4 + a_8 \sum E_{1j}^3 E_{2j} + a_9 \sum E_{1j}^3 = \\
& \sum Ucal_j E_{1j}^3
\end{aligned}$$

.....

$$\begin{aligned}
& a_0 \sum E_{1j}^3 + a_1 \sum E_{1j}^2 E_{2j} + a_2 \sum E_{1j} E_{2j}^2 + a_3 \sum E_{2j}^3 + a_4 \sum E_{1j}^2 + & (5.33) \\
& a_5 \sum E_{1j} E_{2j} + a_6 \sum E_{2j}^2 + a_7 \sum E_{1j} + a_8 \sum E_{2j} + a_9 N = \sum Ucal_j
\end{aligned}$$

The result is a set of linear equations that can be solved by Gaussian elimination or any other method of solving linear equations.

$$\begin{bmatrix} C_{11} & \cdots & C_{1\ 10} \\ \vdots & \ddots & \vdots \\ C_{10\ 1} & \cdots & C_{10\ 10} \end{bmatrix} \begin{bmatrix} a_0 \\ \vdots \\ a_9 \end{bmatrix} = \begin{bmatrix} D_0 \\ \vdots \\ D_9 \end{bmatrix} \quad (5.34)$$

Similar equations can be developed for the flow angle where s is the sum of the squares for the difference between the calibrated angle and the surface fit.

$$s(b_o, b_1, b_2 \dots b_9) = \sum_{j=1}^n (\alpha cal_j - \alpha(E_1, E_2)_j)^2 \quad (5.35)$$

This results in a similar set of linear equations with different coefficients:

$$\begin{bmatrix} F_{11} & \cdots & F_{1\ 10} \\ \vdots & \ddots & \vdots \\ F_{10\ 1} & \cdots & F_{10\ 10} \end{bmatrix} \begin{bmatrix} b_0 \\ \vdots \\ b_9 \end{bmatrix} = \begin{bmatrix} G_0 \\ \vdots \\ G_9 \end{bmatrix} \quad (5.36)$$

A MATLAB function *fullcal2.m* was created to compute the **C**, **D**, **F**, and **G** matrices from a unique, custom, algorithm with a simple nested loop and only a few lines of code. The MATLAB *linsolve* function was used to solve the set of linear equations **Ca=D** and **Fb=G** for the coefficient matrices **a** and **b**. Additional information on the *linsolve.m* function can be found on the Mathworks web site [70]. The script *error_polysurf.m* for solving the polynomial surface coefficients and computing the normalized standard deviation are shown in Appendix B

5.5.3 Surface Interpolation with MATLAB

The third calibration method investigated was similar to the polynomial surface fit; however, MATLAB's *griddata.m* function was employed using the '-v4' option to specify a biharmonic spline interpolation technique. The algorithm is based on the Green function of the biharmonic operator and the interpolating surface is a linear combination of Green functions centered at each data point. The amplitudes of the Green function are adjusted to have the interpolating surface pass through the points. An advantage of this technique is that Green functions at inaccurate data points can be eliminated.

Additional information on the *griddata.m* function and options can be found on the Mathworks web site [71]. The MATLAB script for computing the velocity, angle, and the normalized standard deviation from calibration data using the *griddata.m* function is shown in Appendix B.

5.5.4 Method Comparison

The calibration procedure for the surface interpolation technique was identical to the polynomial surface fit method, and the same data sets were used for all comparisons. Since the *griddata.m* function uses the exact calibration points in the interpolation, an error analysis at those points resulted in zero error. To evaluate and compare methods, 15 of the 45 velocity values were selected over-all yaw angles to establish the calibration surfaces and 15 intermediate velocity values were used to compute the normalized standard deviation, ε_N . Figure 5-12 shows the points used for establishing the calibration grid and also the points (different velocity settings) used to evaluate ε_N .

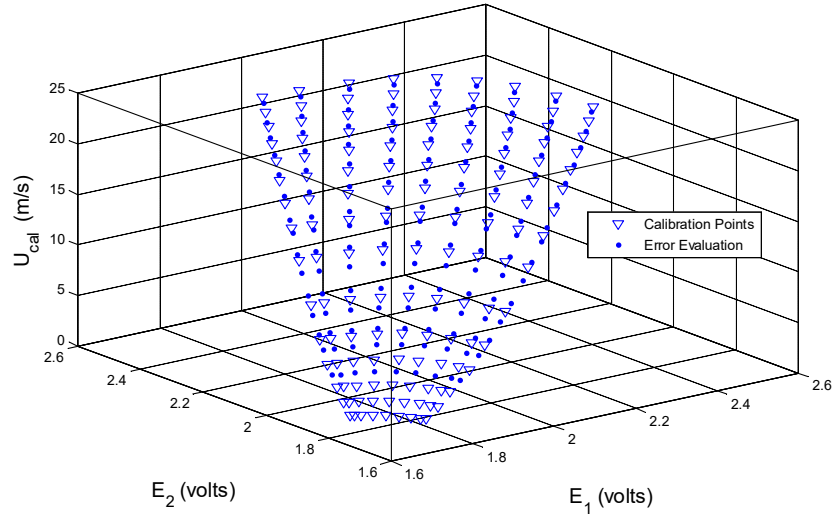


Figure 5-12. Points used to establish calibration surfaces and points used for error evaluation.

Table 5-2 shows the computed normalized standard deviation, ε_N , for the different calibration methods at all yaw angles along with the average error in yaw angle for all calibration points.

Computation time for converting the voltages to velocities is also shown. The values of ε_N are plotted for each method in Figure 5-13 to provide a visual comparison.

Table 5-2. Comparison of normalized standard deviation, yaw angle error, and computation time for different calibration methods.

| Yaw Angle [deg] | Effective Angle | | | Polynomial Surface Fit | | | Surface Interpolation | | |
|-----------------|-----------------|---------------------|-------------------|--------------------------|---------------------|-------------------|-----------------------|---------------------|-------------------|
| | ε_N | Average Angle Error | t_{comp} [msec] | Velocity ε_N | Average Angle Error | t_{comp} [msec] | ε_N | Average Angle Error | t_{comp} [msec] |
| -40 | 0.045 | 4.30 | 16.7 | 0.019 | 1.82 | 4.7 | 0.015 | 0.94 | 165.6 |
| -30 | 0.035 | 1.41 | 16.1 | 0.014 | 1.55 | 3.0 | 0.013 | 0.64 | 127.2 |
| -20 | 0.023 | 0.44 | 16.6 | 0.014 | 1.21 | 2.9 | 0.007 | 0.51 | 130.7 |
| -10 | 0.015 | 0.40 | 14.3 | 0.018 | 0.48 | 2.9 | 0.006 | 0.28 | 134.4 |
| 0 | 0.011 | 0.14 | 16.3 | 0.020 | 0.32 | 3.1 | 0.006 | 0.31 | 137.7 |
| 10 | 0.019 | 0.31 | 16.1 | 0.016 | 0.25 | 3.1 | 0.009 | 0.12 | 137.3 |
| 20 | 0.029 | 0.84 | 16.2 | 0.016 | 1.43 | 3.0 | 0.008 | 0.48 | 126.8 |
| 30 | 0.034 | 2.20 | 16.2 | 0.015 | 1.59 | 5.0 | 0.011 | 0.48 | 136.1 |
| 40 | 0.035 | 5.46 | 16.6 | 0.016 | 1.83 | 3.0 | 0.011 | 0.69 | 137.0 |
| Average | 0.027 | 1.72 | 16.1 | 0.016 | 1.163 | 3.4 | 0.010 | 0.49 | 136.98 |

From Figure 5-13, it is clear that the accuracy of the velocity measurement is more dependent on the yaw angle for the effective angle method. More importantly, the biharmonic interpolation method is shown to be as or more accurate as either of the more traditional effective angle or polynomial surface fit methods.

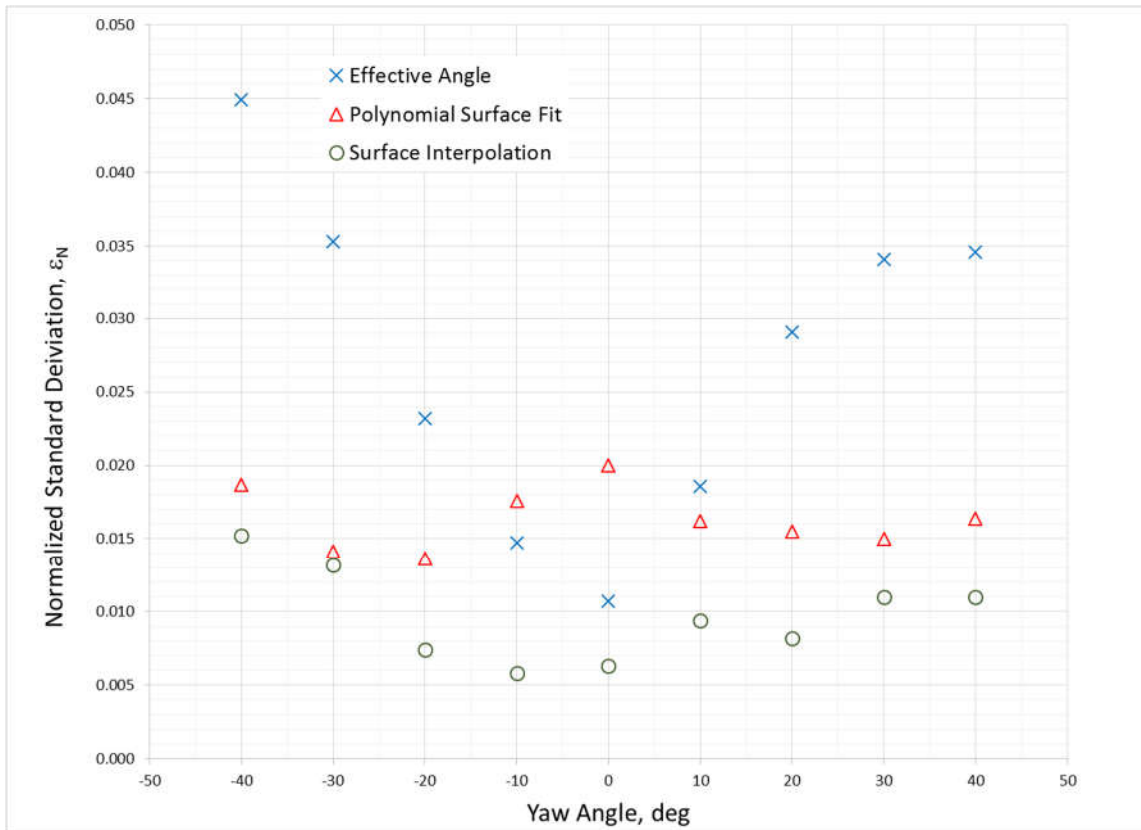


Figure 5-13. Comparison of normalized standard deviation for different hot wire calibration methods.

Converting voltages to velocity can be time consuming, especially for large file sizes and copious data files. The MATLAB *tic* and *toc* commands were used to estimate the time for converting the voltages to velocity and computing ϵ_N . The computation was performed on a 64-bit Windows Operating System with an Intel i7-3635QM processor and 16 GB of RAM. The computation time was determined after all coefficients and grid calibration values were loaded. The results show that the computation time using the *griddata.m* function was substantially longer than either the polynomial surface fit or effective angle method while the polynomial

surface fit method is an order of magnitude faster than the effective angle method. The main advantage of using the surface interpolation technique was its simplicity to implement; it was one command line of programming. The polynomial surface fit technique was mathematically rigorous and required a bit more programming ingenuity; however, the efficiency of the script made it computationally faster.

Another advantage of using the polynomial surface fit or surface interpolation method comes in reducing the uncertainty due to the hot wire probe angle when taking measurements in the wind tunnel. Before taking wind tunnel measurements, the 54H10 calibrator was placed in the wind tunnel with the axis of the nozzle aligned with the axis of the tunnel and the nozzle perpendicular to the probe support as shown in Figure 5-14.

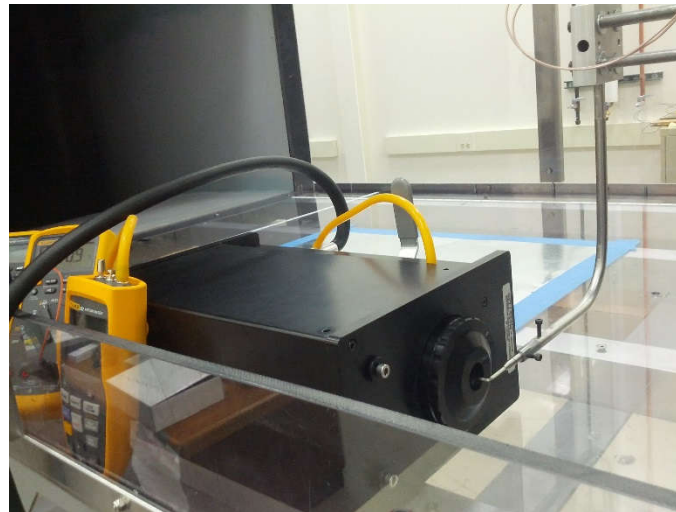


Figure 5-14. In-situ calibration of hot wire anemometer.

In almost every instance before starting wind tunnel experiments, plotting the in-situ calibration with the full calibration data indicated a slight misalignment of the probe, as shown in Figure 5-15. The probe angle was then adjusted such that the in-situ calibration matched the full calibration.

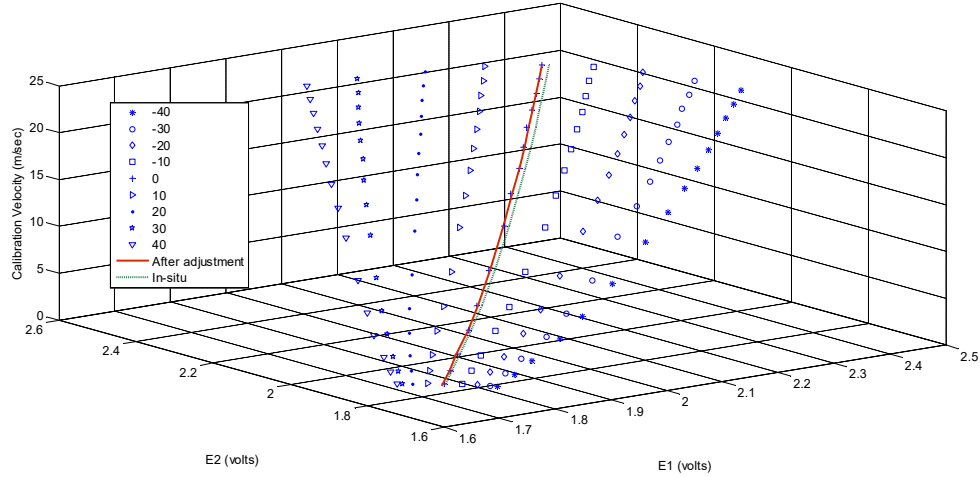


Figure 5-15. In-situ calibration correction for probe angle

5.6 Temperature Correction

With any hot wire anemometer, regardless of the calibration scheme, the effects of varying temperature must be accounted for, as discussed in Hultmark and Smits [46]. Temperature differences are the largest source of error in using HWA. For each wire, the voltage was corrected for the difference between the temperature during calibration, T_r , and the temperature during experimentation, T_o , by:

$$E_c = \left[\frac{T_w - T_r}{T_w - T_o} \right]^{\frac{1}{2}} \cdot E_a \quad (5.37)$$

where T_w is the wire temperature set in the anemometer, E_a is the acquired voltage, and E_c is the corrected voltage. In the experimental data, an additional factor was applied to correct for the differences in measurement between the thermistor in the calibrator and the temperature probe.

6 Model Wind Turbines-Experimental Results and Discussion

6.1 Empty Tunnel

As mentioned, the wind speed in the test section is controlled by the downstream fan speed which is controlled by a variable frequency motor drive. To set the desired wind speed, it was

necessary to know the relationship between the tunnel velocity and the fan motor drive frequency. Figure 6-1 shows the measured velocity at various motor drive settings.

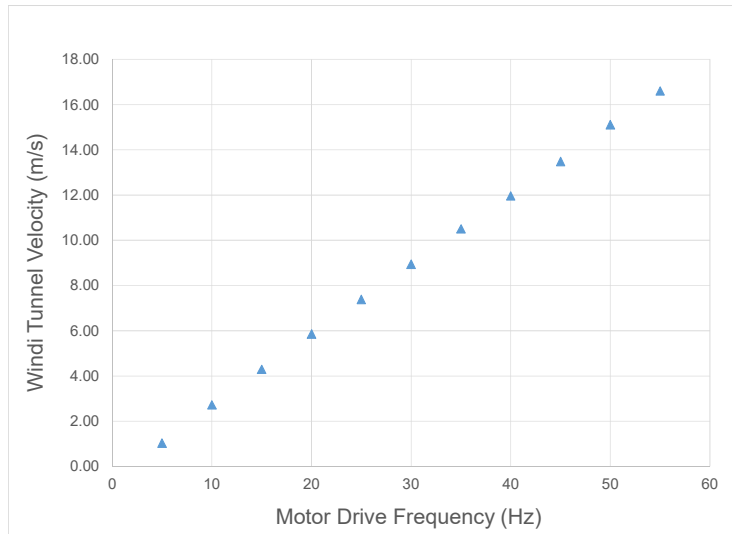


Figure 6-1. Wind tunnel velocity at different motor drive frequencies, $T_o=24.1\text{ C}$

The relationship was consistent and repeatable with minor adjustments made to the drive frequency depending on the freestream temperature and probe calibration.

6.1.1 Empty Tunnel Characterization

Before installing the model wind turbines in the test section, the flow at the inlet of the test section was assessed for ambient turbulence and the profile was measured at three different velocity settings. The inlet flow field was mapped approximately 21cm downstream of the inlet to the test section; this location was the maximum travel of the traverse with the hot wire probe installed.

Figure 6-2 shows a mapping of the velocity at three different drive frequency settings. The velocity at each vertical plane was essentially constant. Measurements were taken in 2.54 cm increments from the centerline of the wind tunnel and progressing toward the side. Since measurements with the wind turbines were only going to be in the half plane of the wind tunnel

to avoid interference between the turbines and the traverse, only half the wind tunnel velocity was mapped. The drive frequency settings were selected based on the range of planned wind turbine testing.

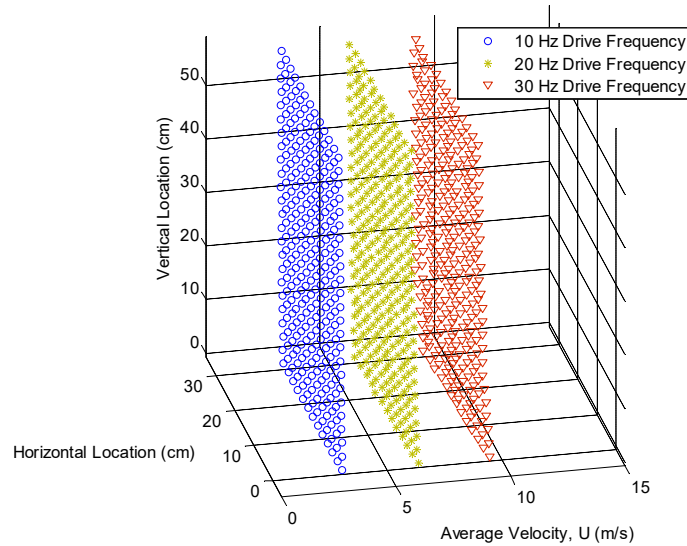


Figure 6-2. Half-plane inlet velocity measurements at three different motor drive frequencies; hot wire probe located 21 cm downstream of test section.

6.1.2 Turbulence measurements

To characterize the freestream inlet turbulence, the hot wire probe was positioned at the hub height, 19.8 cm, and approximately 21 cm downstream of the inlet to the test section. Hot wire measurements were recorded for 26.1 seconds at various motor drive frequencies using a 20 kHz sample rate. The 20 kHz sample rate was the Nyquist rate based on the 10 kHz cutoff setting in the CTA. A statistical analysis of the velocity yielded quantities used to assess turbulence in the flow. The equations listed below consider the velocity to be a discrete time series composed of a mean, \bar{U} , and a fluctuating component, u' .

$$U = \bar{U} + u' \quad (6.1)$$

A similar equation can be written for the V component:

$$V = \bar{V} + v' \quad (6.2)$$

Mean velocities are determined from:

$$\bar{U} = \frac{1}{N} \sum_1^N U_i \quad (6.3)$$

$$\bar{V} = \frac{1}{N} \sum_1^N V_i \quad (6.4)$$

The root mean square (RMS) velocities of the fluctuating component are defined as

$$u'_{rms} = \sqrt{\frac{1}{N-1} \sum_1^N (U_i - \bar{U})^2} \quad (6.5)$$

$$v'_{rms} = \sqrt{\frac{1}{N-1} \sum_1^N (V_i - \bar{V})^2} \quad (6.6)$$

The turbulent intensity, which indicates the fraction of the total energy of the flow that resides in the turbulent regime, can be estimated as relative turbulence intensity and total turbulence intensity. The relative turbulent intensity for each velocity component is

$$I_u = 100 \times \frac{u'_{rms}}{\bar{U}} \quad (6.7)$$

$$I_v = 100 \times \frac{v'_{rms}}{\bar{V}} \quad (6.8)$$

and the total turbulence intensity is computed from

$$I_T = 100 \times \sqrt{\frac{\frac{1}{2}(u'^2_{rms} + v'^2_{rms})}{\bar{U}^2 + \bar{V}^2}} \quad (6.9)$$

The turbulence kinetic energy (TKE) is the mean kinetic energy per unit mass and is defined as

$$TKE = \frac{1}{2} (\overline{u'u'} + \overline{v'v'} + \overline{w'w'}) \quad (6.10)$$

Other statistical parameters that can be of importance are the Skewness and Kurtosis:

$$S_u = \frac{1}{N} \sum_1^N \frac{(U_i - \bar{U})^3}{\sigma_u^3} \quad (6.11)$$

$$S_v = \frac{1}{N} \sum_1^N \frac{(V_i - \bar{V})^3}{\sigma_u^3} \quad (6.12)$$

$$K_u = \frac{1}{N} \sum_1^N \frac{(U_i - \bar{U})^4}{\sigma_u^3} \quad (6.13)$$

$$K_v = \frac{1}{N} \sum_1^N \frac{(V_i - \bar{V})^4}{\sigma_u^3} \quad (6.14)$$

The skewness, S_u and S_v , is a measure of the lack of statistical symmetry in the flow and values near zero indicate symmetry. Kurtosis, K_u and K_v a measure of the amplitude distribution (flatness factor) and low values indicate the amplitudes are clustered near the mean; high values suggest extreme peaks dominate the time series. Table 6-1 is a summary of the statistics at various drive frequencies.

Table 6-1 Empty tunnel turbulent flow statistics at different motor drive frequencies

| Drive Freq | U_{ave} | V_{ave} | I_t |
|------------|-----------|-----------|-------|
| [Hz] | [m/s] | [m/s] | [%] |
| 10 Hz | 2.80 | -0.09 | 0.44 |
| 15 Hz | 4.10 | -0.06 | 0.40 |
| 20 Hz | 5.49 | -0.09 | 0.41 |
| 30 Hz | 8.27 | -0.13 | 0.38 |
| 60 Hz | 16.42 | 0.08 | 0.38 |

The MATLAB script to compute the flow statistics, *emptyspectral.m*, is listed in Appendix B.

Figure 6-3 is the time series of the measured U velocity and Figure 6-3 is the measured V velocity with the fan motor drive frequency at 10 Hz.

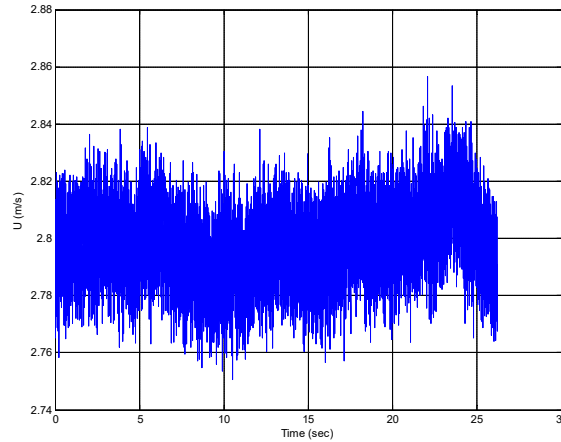


Figure 6-3. Time series of U -velocity at test section inlet, 10 Hz drive frequency

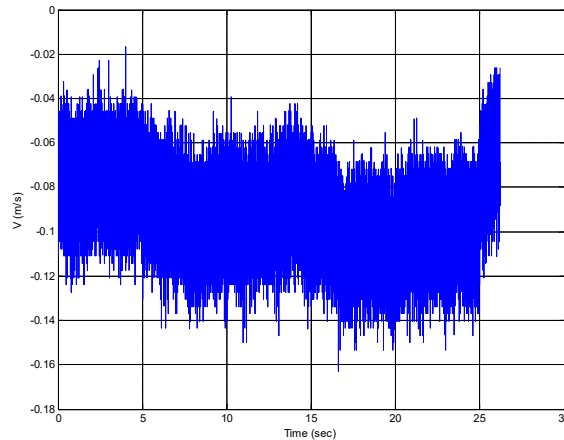


Figure 6-4. Time series of V -velocity at test section inlet, 10 Hz drive frequency

At each of the motor drive frequencies listed in Table 6-1, the fluctuating portion of the velocity signal, u' , was analyzed using the *pwelch.m* function in MATLAB. The *pwelch.m* function provides the power spectral density (PSD) at various frequencies. It can be considered as a measurement of the turbulent energy content at various frequencies. Figure 6-5 is a plot of the PSD at various drive frequencies. At low velocity (low drive frequency), the velocity is dominated by fluctuations less than 100 Hz. The dominant frequency range and turbulence energy increases with velocity.

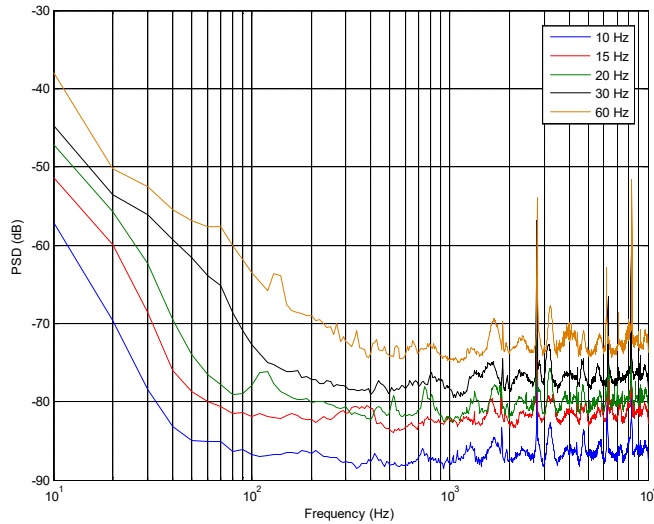


Figure 6-5. Power spectral density (PSD) of velocity signal in empty wind tunnel at various motor drive frequency settings

6.2 Experiments with Model Wind Turbines

Before discussing the experimental results, it is useful to review the aerodynamics of a horizontal-axis wind turbine wake. The wake is typically divided into a near wake and a far wake as shown in Figure 6-6.

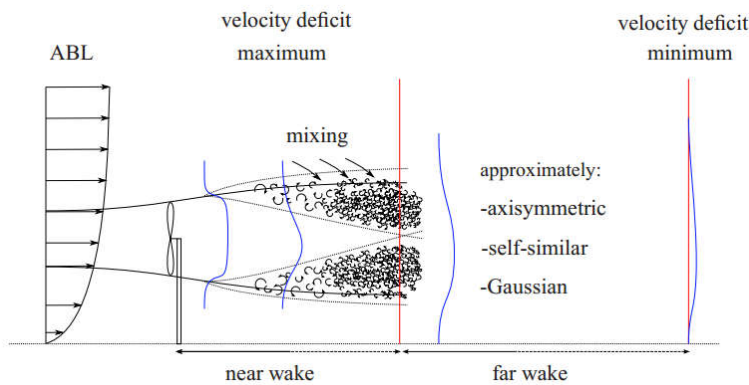


Figure 6-6. Wake profiles of a horizontal-axis wind turbine [72]

The near wake is defined as the area directly behind the rotor extending to 1-3 rotor diameters. This region is dominated by pressure and velocity gradients resulting from the extraction of mean flow energy by the rotor. In this region, the blade geometry dictates the shape of the flow field and the pressure gradient at the rotor is important in developing the wake velocity deficit.

The reduction in velocity in the near wake region is directly related to the thrust coefficient since this determines the momentum transferred from the free stream to the turbine. As the lower speed wake convects downstream, the velocity gradient between the wake and the free stream creates shear-generated turbulence, which transfers momentum into the wake and causes mixing. The mixing region spreads to the center of the wake and outward which erodes the velocity deficit and expands the wake. The wake velocity eventually recovers and the profile becomes axisymmetric and Gaussian in shape.

The wind tunnel at UWM was used to measure the velocity profiles and turbulence downstream of a model wind turbine. Two additional turbines were added in series to examine the effect of multiple turbines on the velocity deficit and the turbulence intensity. Model turbines were spaced two rotor diameters apart and downstream measurements were restricted to $x/D_{b1}=6.8$, $x/D_{b2}=4.7$, and $x/D_{b3}=2.7$ for one, two, and three turbines, respectively. These restrictions were due to the length of the wind tunnel and the allowable position of the traverse.

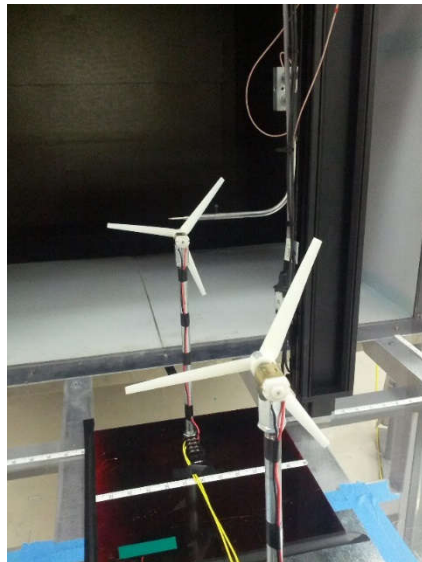


Figure 6-7. Dual turbine installation in test section

Figure 6-7 shows the two turbines installed in the wind tunnel with the hot-wire probe positioned at the rotor centerline, just ahead of the first turbine. In the last stage, a third turbine was

installed in line with the previous two and 40.64 cm downstream of the first turbine. All hot-wire measurements were taken with the fan motor drive frequency set at 23 Hz which corresponded to 6.65 m/s.

6.2.1 Single Turbine Measurements

Hot-wire measurements with the single turbine were taken in 6.35 mm increments in both vertical (y) and horizontal (-z) directions at the planes shown in Figure 6-8.

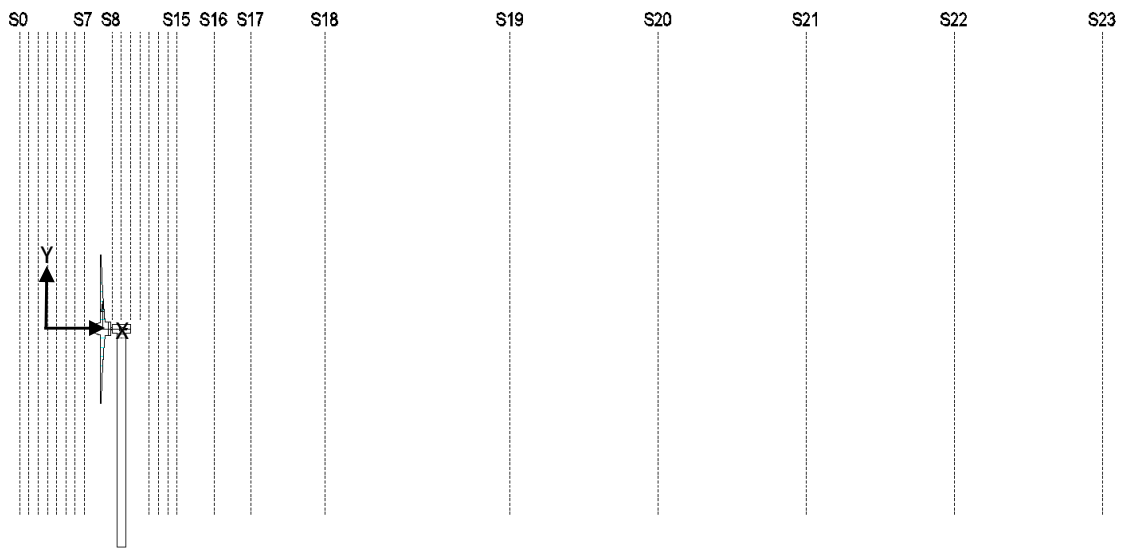


Figure 6-8. Measurement plane locations for single turbine experiments

The measurement planes have been identified as S0 through S23 and dimensions for plane locations are listed in Appendix D. Except at the planes immediately behind the rotor (S8-S11), vertical measurements were taken at the turbine centerline 20.3 cm below the hub height and extending 20.3 cm above the hub height. The horizontal measurements were taken at the hub height extending laterally 20.3 cm from the centerline. Lateral (horizontal) measurements were restricted to the half-plane to avoid interference between the turbine and the traverse. Directly behind the turbine, vertical measurements were taken from 1.27 cm above the rotor centerline extending to 20.3 cm; horizontal measurements were taken 2.54 cm from the rotor centerline extending 22.9 cm. At each measurement point, the hot-wire voltages were sampled for 0.5

seconds at 20 kHz and data for each point was saved to a unique text file. Before initiating hot-wire measurements in each plane, the blade speed was recorded with the hot wire probe positioned at the hub height as shown in Figure 6-7. The arm of the traverse was located approximately 10 cm downstream of the hot-wire probe and approximately 20 cm from the edge of the traverse arm. It was noted that the blade speed was dependent on the position of the traverse.

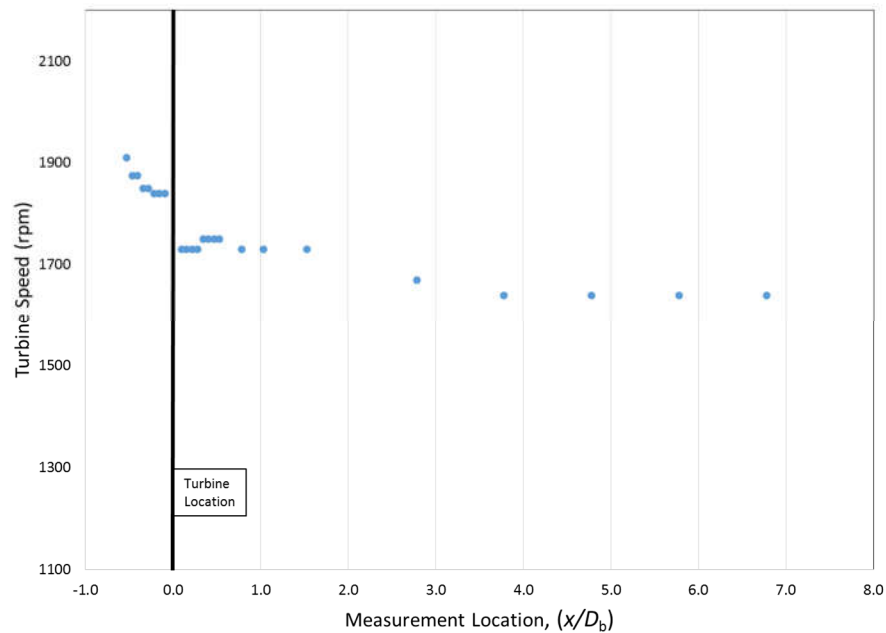


Figure 6-9. Measured blade speed with hot-wire probe positioned at the hub height and at planes shown in Figure 6-8.

Figure 6-9 shows the closer the traverse arm is to the turbine, the higher the rotational speed. The highest rotational speeds occurred when the traverse arm was even or ahead of the turbine. The position of the traverse arm in the lateral direction also affected the blade speed, but the effect was not documented. The rotational speed increase is caused by more air flow to the turbine as it is re-directed around the traverse arm and the area between the turbine and the traverse is reduced; this effect was also seen in measurements with multiple turbines.

The air temperature was recorded at each measurement plane and values were used to correct for the difference between measurements and hot-wire calibration. Temperature changes were less than 0.4 °C throughout all measurements.

Figure 6-10 shows velocity deficit profiles in three different regions from vertical measurements on a single turbine. The velocity deficit is plotted as $\Delta U = 1 - U/U_\infty$ which indicates a lower measured velocity has a higher deficit. The vertical axis has been normalized by the blade radius with $y=r=0$ equal to the hub height and rotational centerline.

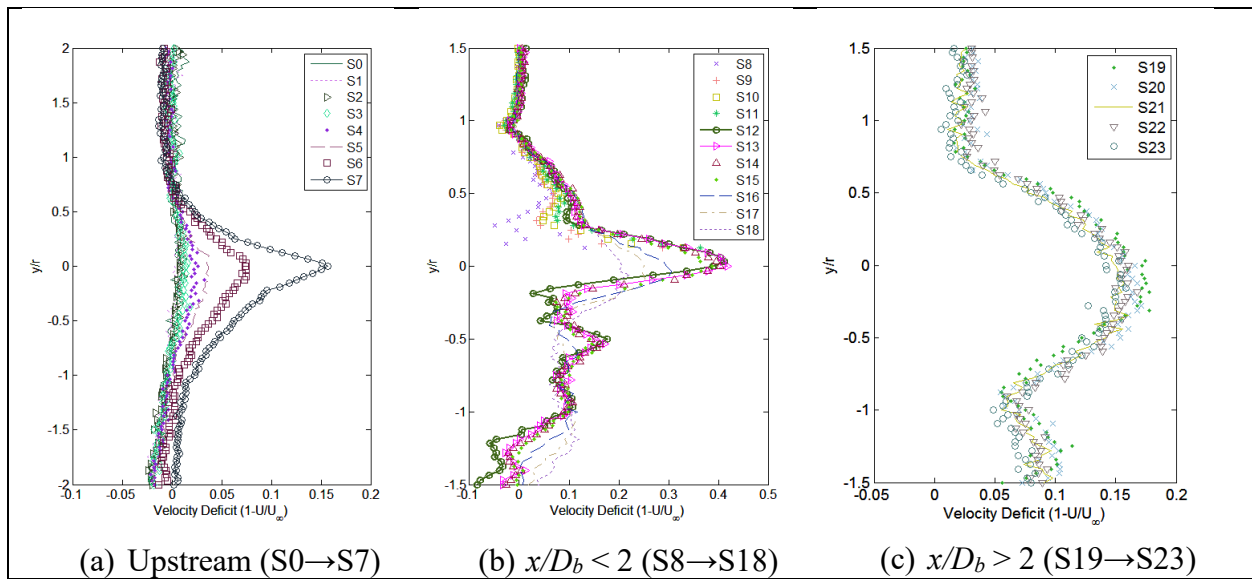


Figure 6-10. Velocity deficit profiles for three vertical measurement regions at locations shown in Figure 6-8, $U_\infty = 6.6$ m/s.

For the upstream measurements in Figure 6-10(a) the deficit increases as the flow approaches the rotor and the deficit is symmetric about the rotational axis ($y/r=0$). As expected, the highest deficit occurs closest to the hub (plane S7) as the flow stagnates near the center of the hub. With the outer edge of the hub at $y/r \sim 0.1$, the spread in the upstream deficit between $y/r = \pm 0.5$ suggests the blades are creating a substantial pressure gradient in the radial direction. The pressure gradient is specific to the blade design and results from the larger blade width and blending near the root (i.e. higher local solidity). Downstream and within two rotor diameters,

Figure 6-10(b) shows a non-symmetric deficit about the rotational axis; the deficit pattern below the hub height is more erratic and the deficit magnitude is higher due to turbulence generated from the tower and interaction with the rotating blades. Above the hub centerline, there are three distinct regions created by shear layers and pressure gradients in the wake. Above $y/r \sim 1$, the deficit is near zero as the velocity is equal to the free stream velocity. A shear layer is present at the outer edge of the blade near $y/r=1$ where the wake and free stream interact. Between $y/r \sim 0.3$ and $y/r \sim 1$, the deficit increases for lower y/r values due to momentum extracted from the flow and turbulence created by the turbine blades. Figure 6-10 also shows the largest deficit occurs at $y/r=0$ and between $y/r \pm 0.3$ which is likely due to the combination of turbulence created at the blade, pressure gradient from the solid hub, and pressure gradient from the blades. As the turbulence dissipates and the free stream flow mixes with the wake flow, pressure and velocity gradients erode and the deficit profile becomes Gaussian as shown in Figure 6-10(c).

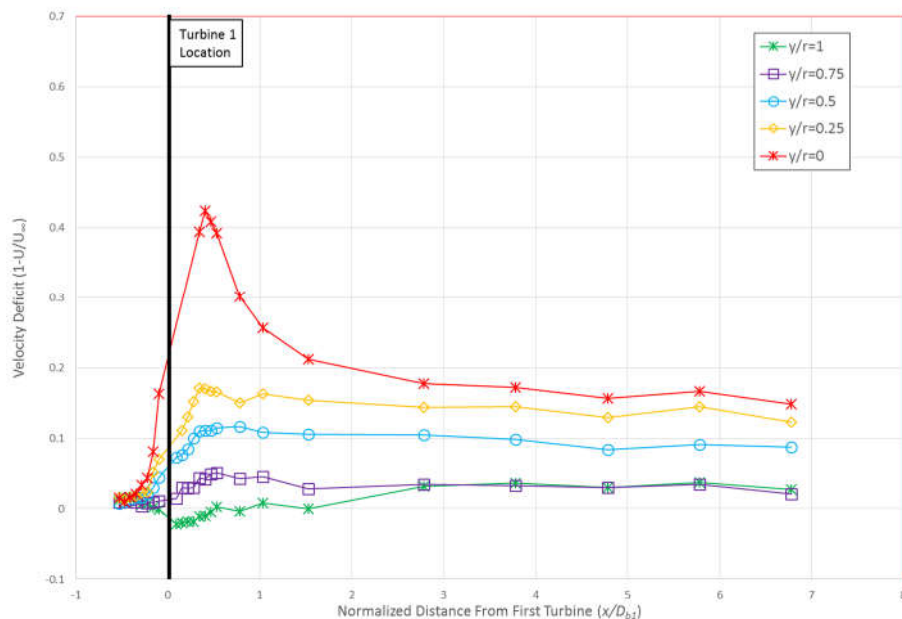


Figure 6-11. Downstream velocity deficit from vertical measurements at various y/r values, $U_\infty=6.6$ m/s.

The wake does not appear to expand as expected which may be due to lack of turbulent energy in the freestream flow and insufficient mixing in the shear layer. Note there is still an additional deficit created due to the presence of the tower far downstream. Figure 6-11 shows there is very little change in the deficit beyond three rotor diameters where the majority of the turbulence and pressure gradients have dissipated.

Figure 6-12 shows the corresponding velocity deficit profiles for lateral (horizontal) measurements at the same plane locations. Comparison to Figure 6-10 shows similarity in the shape and magnitude of the deficit for $z/r > 0$ and indicates the flow would be axisymmetric without the tower. As with measurements in the vertical direction, there are three distinct regions where the shape is different; however, the gradient at the edge of the the blade appears to be near $z/r \sim 0.8$ which suggests the wake may have shifted toward $z/r=0$ due to air flow around the traverse.

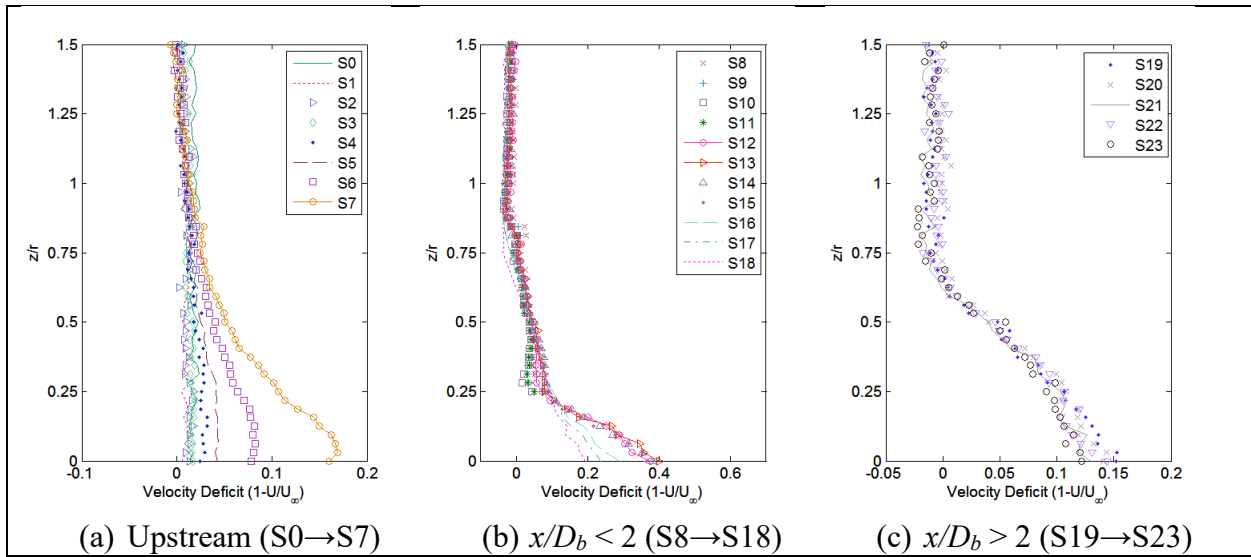


Figure 6-12. Velocity deficit profiles for three horizontal measurement regions at locations shown in Figure 6-8, $U_\infty=6.6$ m/s

The total turbulence intensity (%) at each measurement plane, calculated from equation 6.8, is shown in Figure 6-13.

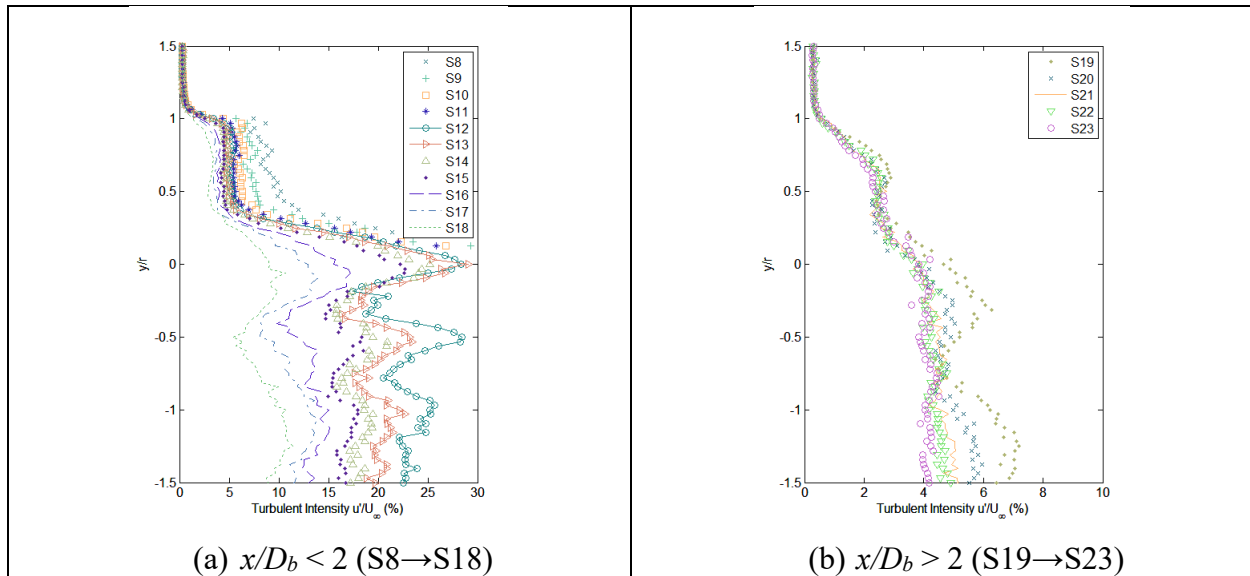


Figure 6-13 Turbulence intensity from two measurement regions in the vertical direction at x/D_b locations shown in Figure 6-8, $U_\infty=6.6$ m/s.

Within the first two rotor diameters, the turbulence intensity (TI) is highest directly behind the turbine at planes, S8-S18, and at y/r values closer to zero (closer to the hub). For $y/r < 0$, there is significant turbulence generated by the tower and the interaction with the rotating blade. As with the velocity deficit, there are three regions of interest for $y/r > 0$. At $y/r=1$, there is a sharp gradient in TI due to the shear layer between the rotating wake and the free stream. While there appears to be slight spike in the intensity at the S8 plane, a higher turbulence intensity was expected at this location. Bartel, et al. [73] and Chamarro and Porte'Angel [30] reported enhancement of the turbulence intensity at the tip due to a helical vortex. A helical vortex structure was seen in high speed images and will be discussed in Section 6.3. Hot-wire anemometry is unable to capture the structure of the helical tip vortex, unlike PIV [32]. Between $y/r \sim 0.3$ and $y/r=1$, the turbulence intensity is higher near the blades in planes S8-S11, but quickly dissipates to a near constant 5% value in the radial direction. Figure 6-14 shows there is little change in the TI beyond one rotor diameter in the downstream direction for this y/r range. Turbulence in this region is likely created by boundary layer separation and shear stresses at the

surface of the turbine blades. Between $y/r=0$ and $y/r\sim 0.3$, the TI is greatest closer to the turbine blades and dissipates more slowly in the freestream direction compared to $y/r > 0.3$. Turbulence in this region is dominated by pressure gradients, but also from general turbulence from surfaces of the hub, blades, and nacelle (DC motor in this case). From Figure 6-14, the turbulence intensity does not dissipate until 3 rotor diameters downstream. There is a strong correlation in the profiles of the turbulence intensity and the velocity deficit where regions of higher turbulence intensity have a higher deficit; deficit recovery in the freestream x/D_b direction also corresponds with a reduction in turbulence intensity.

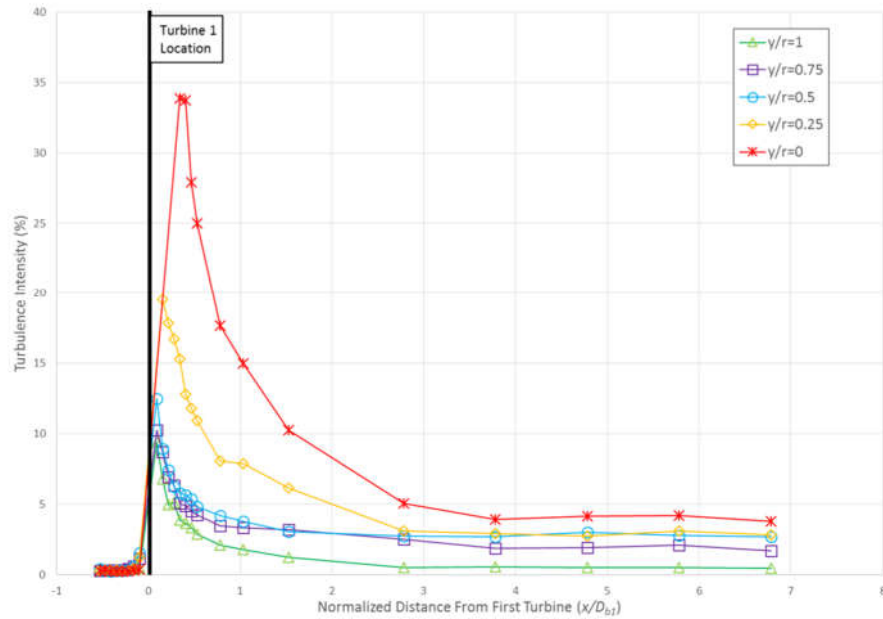


Figure 6-14. Downstream turbulence intensity from vertical measurements at various y/r values, $U_\infty=6.6$ m/s

Turbulence created by the tower and the interaction with the rotating turbine blades is significant and is of the same order or higher than turbulence generated by the blade itself. The turbulence generated from interaction with the tower does not appear to dissipate as quickly as the turbulence generated from the blade. The greater turbulence intensity and velocity deficit in this

region ($y/r < 0$) suggests the tower geometry should not be neglected in wake studies and CFD simulations.

6.2.2 Dual Turbine Results

Hot-wire measurements, with two turbine spaced two blade diameters apart, were taken in 3.18 mm increments in both vertical (y) and horizontal ($-z$) directions at the planes shown in Figure 6-15. The measurement planes have been identified as D0 through D43 and dimensions for plane locations are listed in Appendix D.

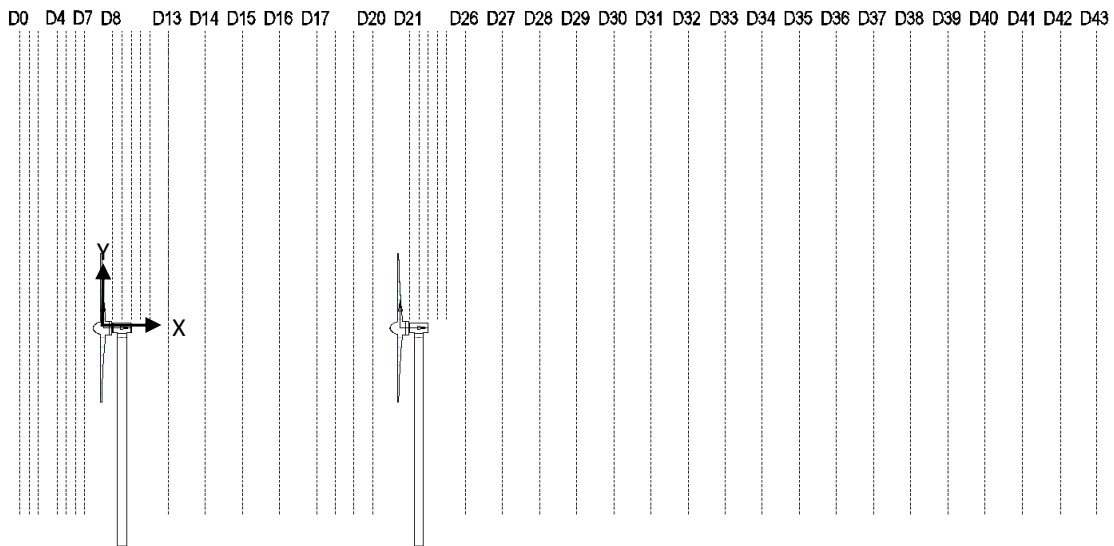


Figure 6-15. Measurement plane locations for dual turbine experiments.

Additional measurement planes were added after experiments with the single turbine to get a better mapping of the profiles along the length of the tunnel. Except at the planes immediately behind the rotors (D8-D12 and D21-D25), vertical measurements were taken at the turbine centerline 25.4 cm below the hub height and extending 25.4 cm above the hub height. The horizontal measurements were taken at the hub height extending laterally 25.4 cm from the centerline. As in the single turbine testing, the rotational speed of each turbine was recorded with the hot-wire probe positioned at the hub height as shown in Figure 6-7. Figure 6-16 clearly shows the location of the traverse affected the turbine speeds with the speed of the second

turbine exceeding the speed of the first turbine during most measurement points between the two turbines. The speed increase indicates momentum is added to the wake of the first turbine as flow is re-directed around the traverse.

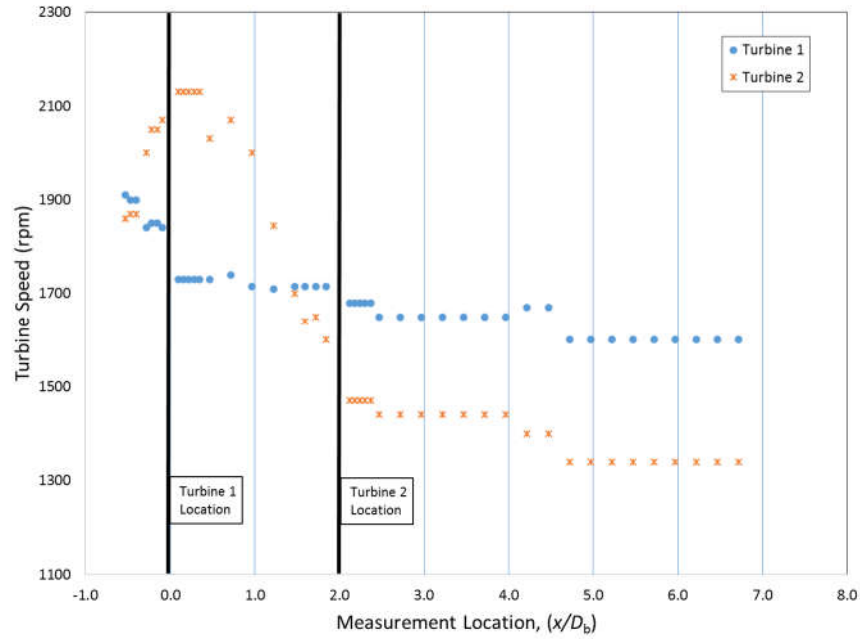


Figure 6-16. Measured blade speed with hot-wire probe positioned at the hub height and at planes shown in Figure 6-15.

Figure 6-17(a) shows the deficit profiles from vertical measurements between the first and second turbines and Figure 6-17(b) shows the profiles after the second turbine, but only up to two rotor diameters downstream. Figure 6-17(c) shows the profile after two rotor diameters; if not for the tower, the profile would be Gaussian-shaped about the rotational centerline. Measurements upstream of the first turbine are not shown, but they were nearly identical to the values from experiments using a single turbine. The general shape of the vertical profiles between the first and second turbines are very similar to the profile shapes after the second turbine. The profiles after the first turbine are nearly identical to the single turbine measurements which would be expected. As with testing with a single turbine, the velocity

deficit profiles do not change appreciably after two rotor diameters downstream of the second turbine.

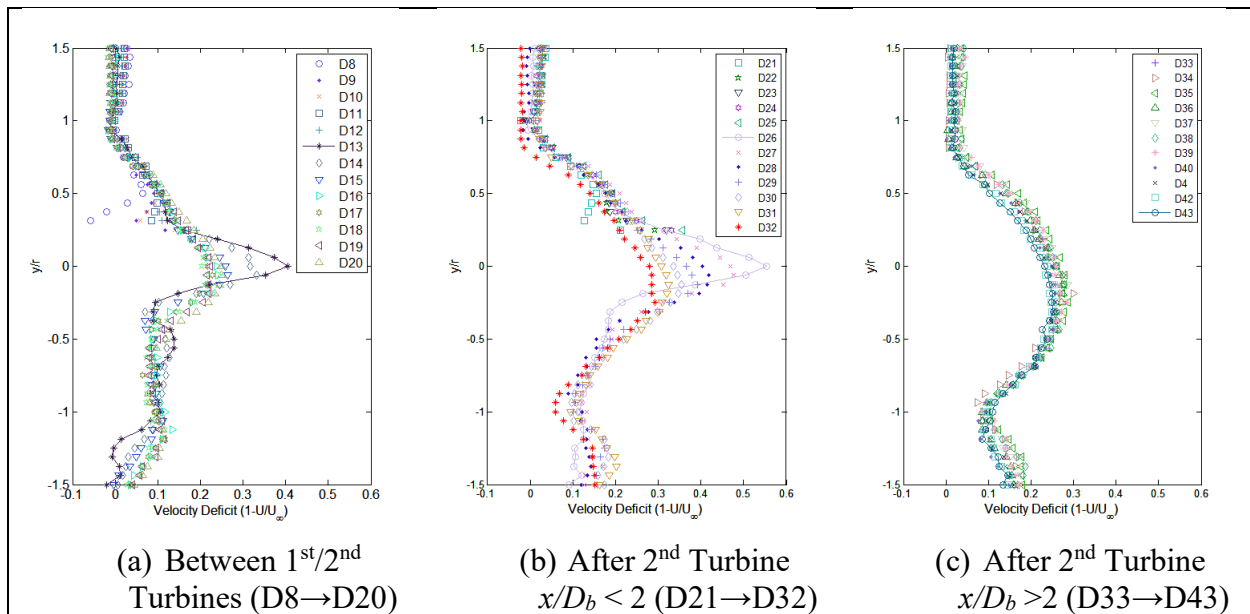


Figure 6-17. Velocity deficit profiles for three vertical measurement regions at locations shown in Figure 6-15.

There are distinct gradients in the profiles near $y/r=0.3$ and $y/r=1$, much like in the single turbine tests. The maximum deficits occurred at planes D13 and D26 which correspond to $x/D_b \sim 0.5$.

At $x/D_b > 2$, the deficit profiles show the wake is Gaussian-shaped after the second turbine.

Looking at the deficit at several y/r values in the freestream direction, Figure 6-18 shows how the second turbine adds to the deficit. There is a sharp gradient in the deficit after each turbine as momentum is extracted from the flow and pressure gradients are created across the turbines.

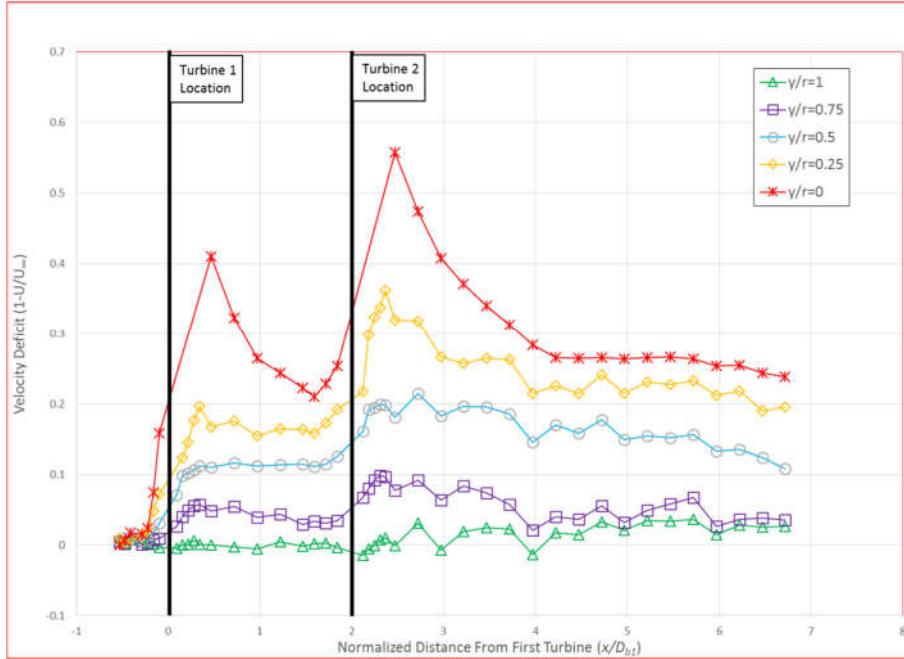


Figure 6-18. Downstream velocity deficit from vertical measurements at various y/r values, $U_\infty=6.6$ m/s

Figure 6-19 shows the corresponding horizontal measurements with two inline turbines. In comparing to Figure 6-17, the profiles indicate the flow is axisymmetric. Similar to experiments with a single turbine, the curves also indicate a shift in the wake with the gradient at zero deficit near $z/r=0.8$.

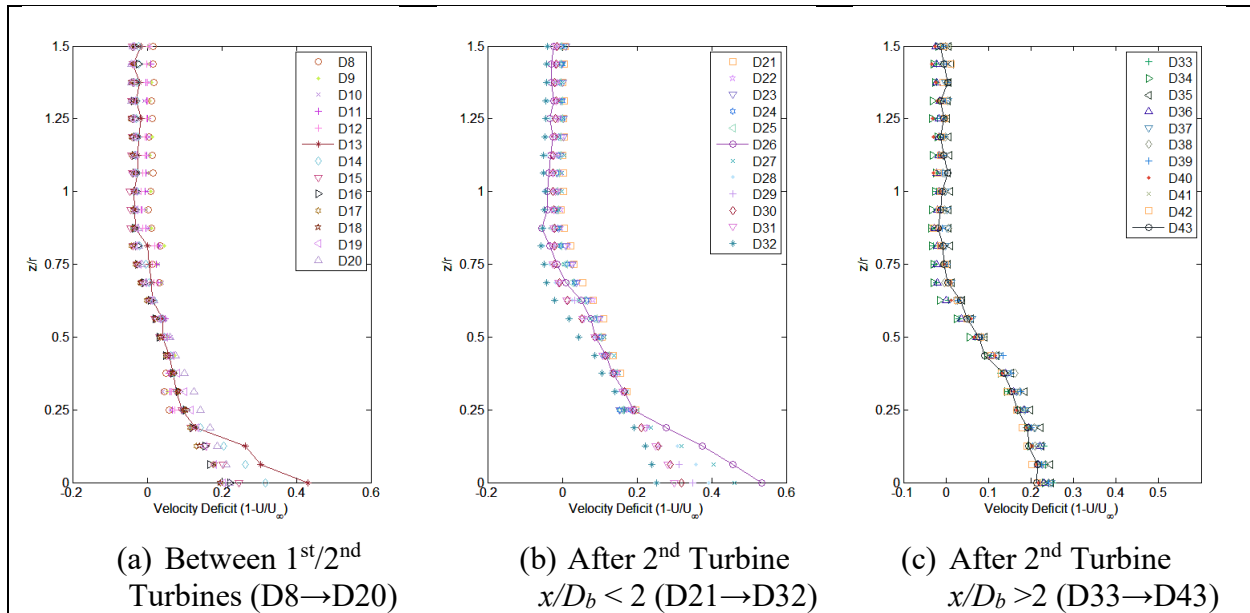


Figure 6-19. Velocity deficit profiles for three horizontal measurement regions at locations shown in Figure 6-15.

The turbulent intensity for each region is shown in Figure 6-20. The trends are the same as in the single turbine testing with the highest turbulence near the blade and very little change beyond three rotor diameters.

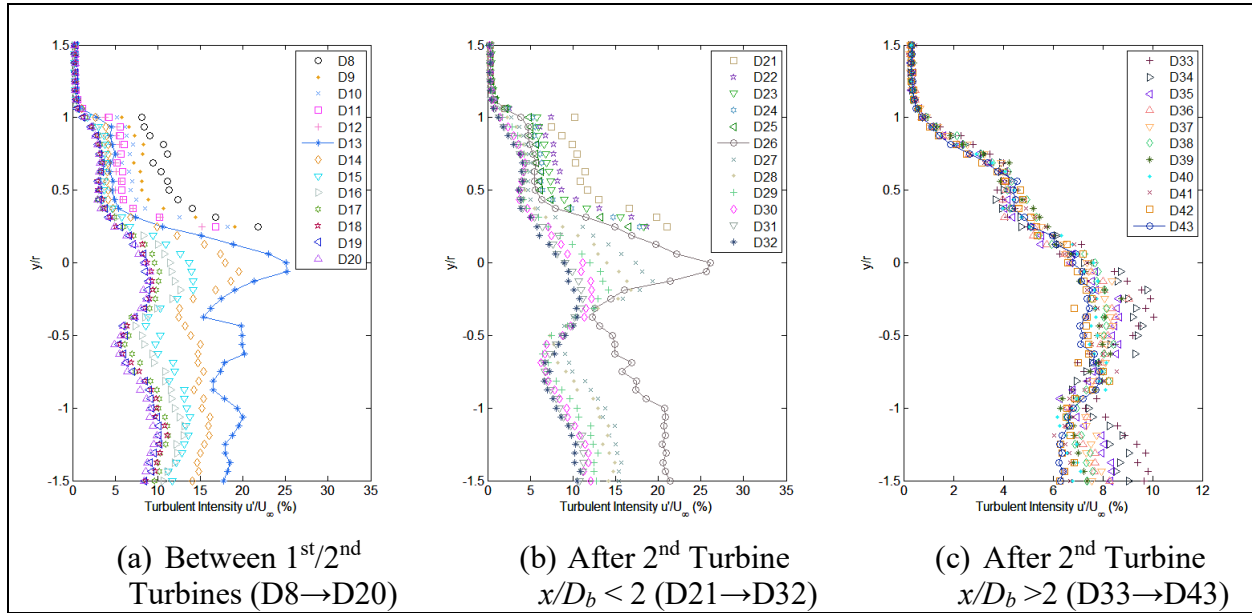


Figure 6-20. Turbulent intensity profiles from vertical measurements at locations shown in Figure 6-15.

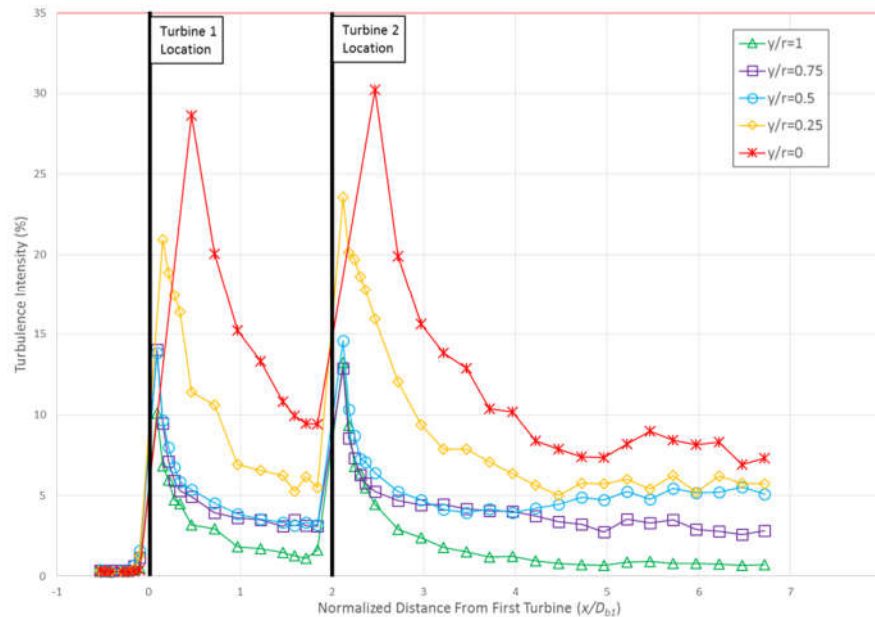


Figure 6-21. Downstream turbulence intensity from vertical measurements at various y/r values, $U_{\infty}=6.6$ m/s

The effect of the additional turbine can be seen clearly in Figure 6-21 with a sharp rise in the turbulence intensity after the second turbine and a sharp decay within one rotor diameter. The sharp decay in intensity within one rotor diameter is a result of dissipation of higher frequency turbulence generated by the turbine blades and tip vortices.

6.2.3 Triple Turbine Results

A third turbine was added 40.6 cm downstream of the second turbine. Hot wire measurements, with the three turbine spaced two blade diameters apart, were taken in 3.18 mm increments in both vertical (y) and horizontal (-z) directions at the planes shown in Figure 6-22. The measurement planes have been identified as T0 through T48 and dimensions for plane locations are listed in Appendix D.

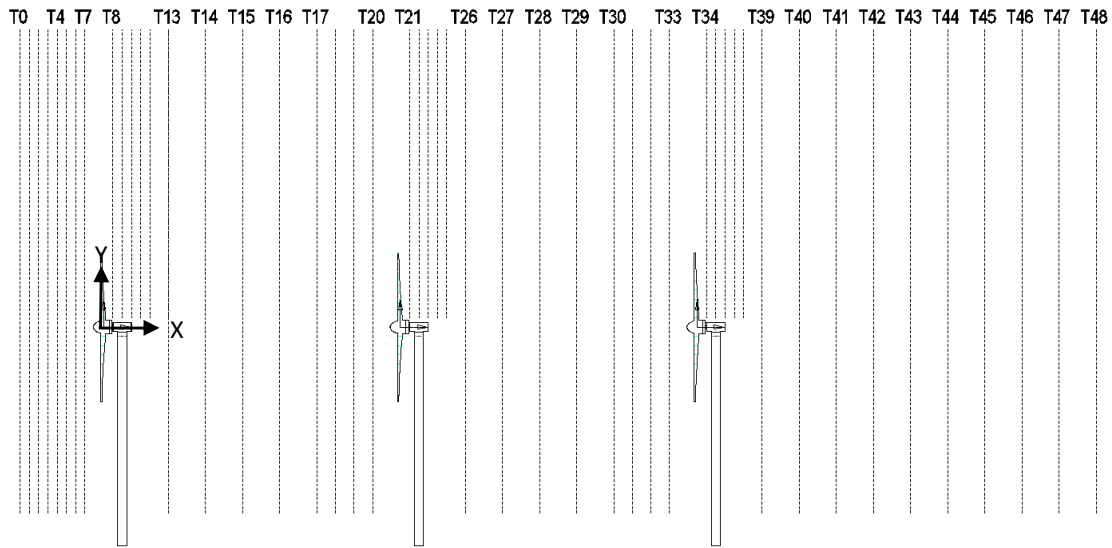


Figure 6-22. Measurement plane locations for measurements using three turbines

Except at the planes immediately behind the rotors (T8-T12, T21-T25, and T34-T38), vertical measurements were taken at the turbine centerline 25.4 cm below the hub height and extending 25.4 cm above the hub height. The horizontal measurements were taken at the hub height

extending laterally 25.4 cm from the centerline. As in the single turbine testing, the rotational speed of each turbine was recorded with the hot-wire probe positioned at the hub height. Figure 6-23 is a photograph of the turbines installed in the wind tunnel looking toward the inlet flow. The photograph shows the location of the hot-wire probe relative to the traverse with the traverse positioned as far from the turbines as possible in the lateral direction. The support tube attached to the probe is located approximately 10.2 cm in front of the traverse (toward the inlet).

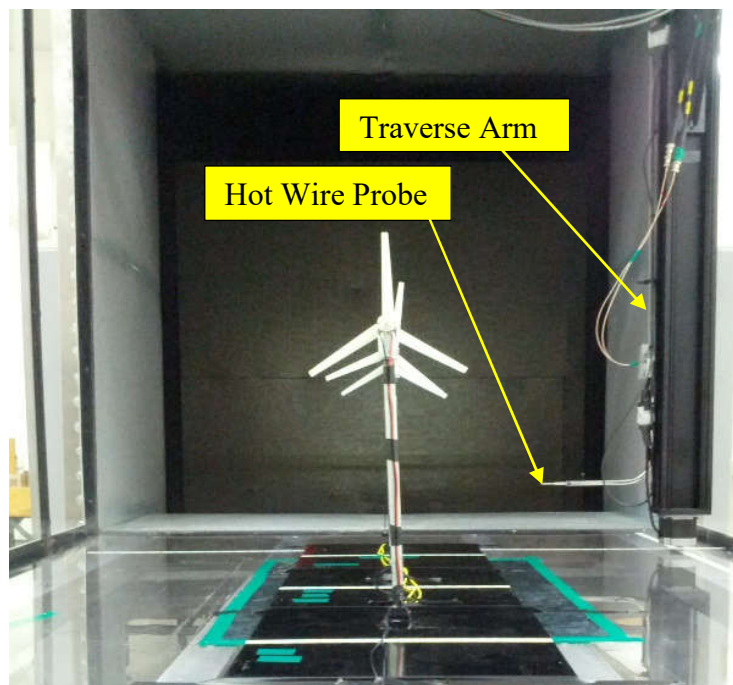


Figure 6-23. Three model turbines aligned in the wind tunnel with hot wire probe positioned at maximum distance from turbine centerline.

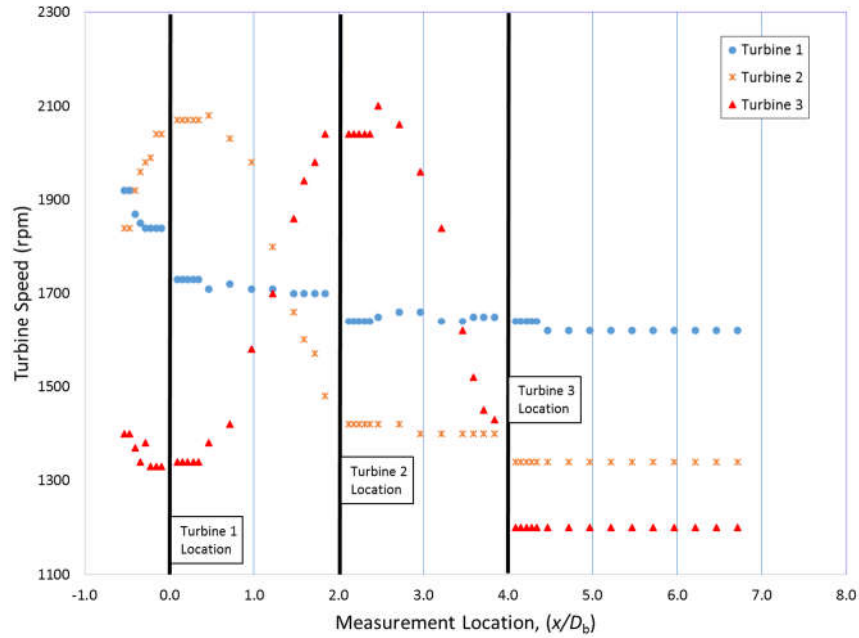


Figure 6-24. Measured blade speed with hot-wire probe positioned at the hub height and at planes shown in Figure 6-22

The location of the hot-wire probe and traverse affected all turbine speeds with flow directed around the traverse adding momentum to the flow to each downstream turbine.

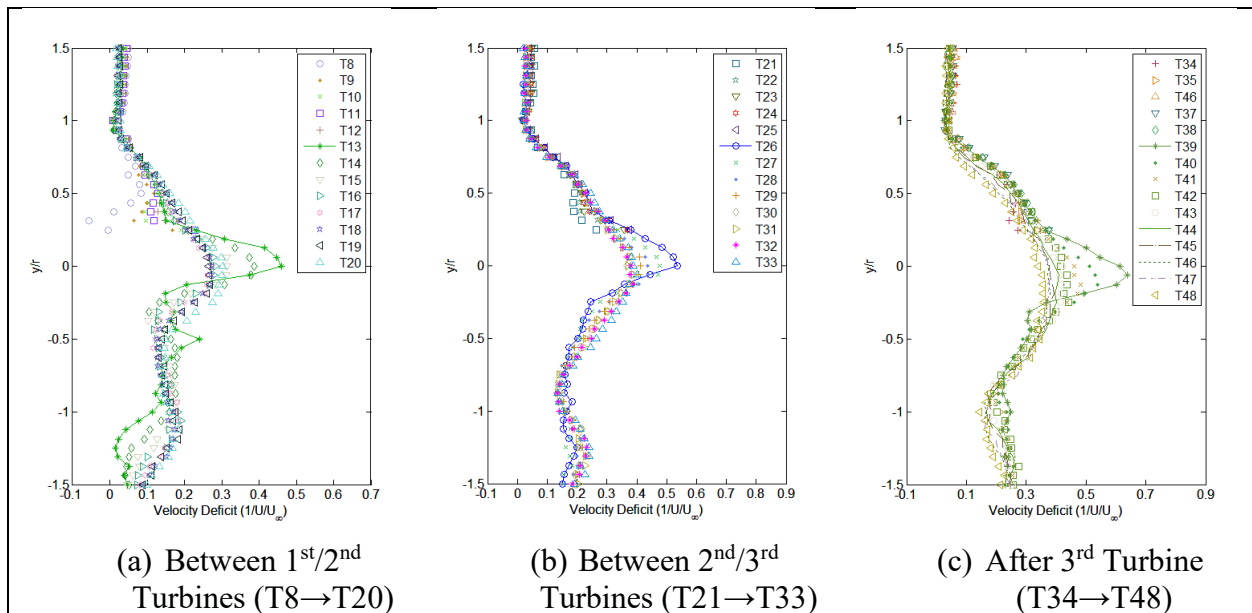


Figure 6-25. Velocity deficit profiles for three vertical measurement regions along turbine center line at locations shown in Figure 6-22

The velocity deficit profiles for vertical measurements are shown in Figure 6-25 for three different regions with the probe positioned in line with the center of the turbine. Measurement

upstream of the first turbine are not shown, but they were nearly identical to the values from experiments using a single turbine. The profiles between the first and second turbines are similar to the profiles between the second and third turbines. There are distinct gradients in the profiles near $y/r=0.3$ and $y/r=1$, much like in the single and dual turbine tests. The maximum deficits occurred at planes T13, T26, and T39 which correspond to $x/D_b \sim 0.5$. At $x/D_b > 2$, the deficit profiles show the deficit has eroded and the shape is Gaussian-shaped.

Figure 7-27 shows the effect of additional turbines on the velocity deficit. After each turbine, the deficit increased sharply for all y/r values less than one due to momentum being extracted from the flow and pressure gradients across the rotor.

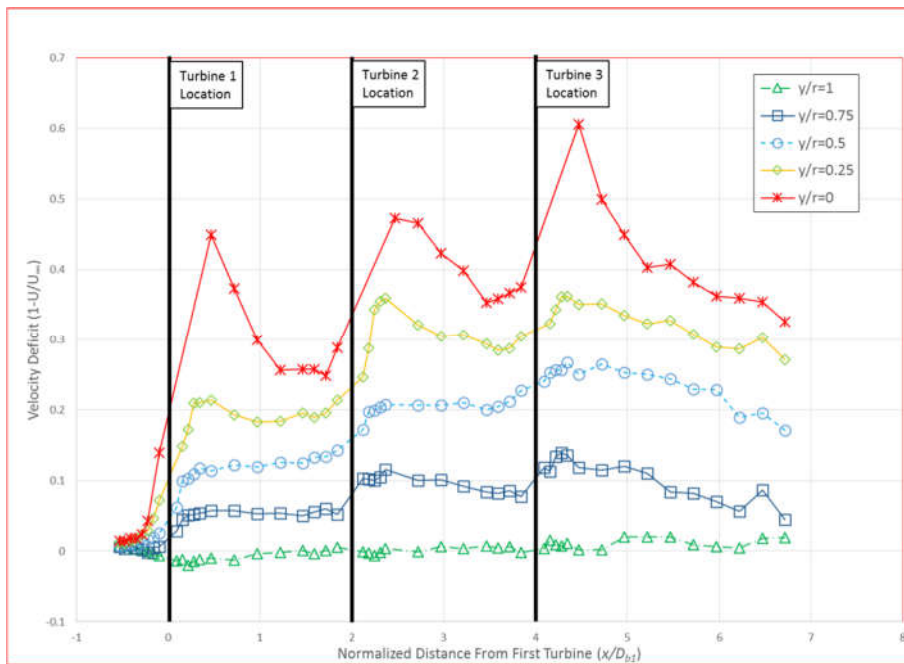


Figure 6-26. Downstream velocity deficit from vertical measurements at various y/r values, $U_\infty=6.6$ m/s

Figure 6-27 shows the corresponding horizontal measurements with three inline turbines. In comparing to Figure 6-25, the profiles indicate the flow is axisymmetric, but also show a shift in the wake with the gradient at zero deficit near $z/r=0.8$.

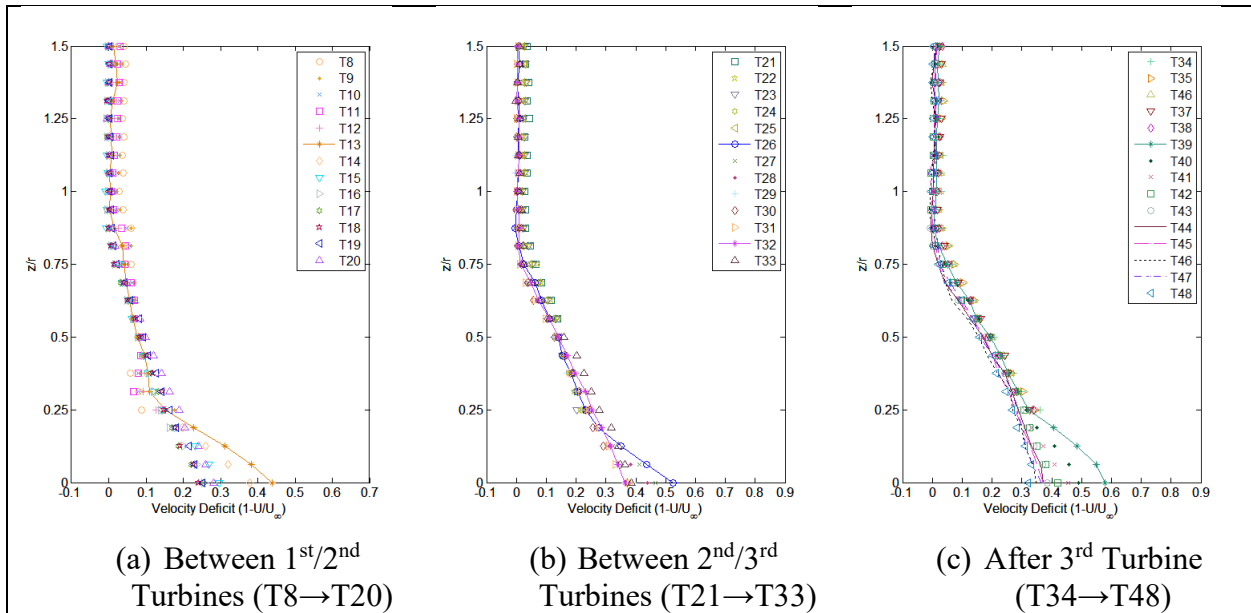


Figure 6-27 Velocity deficit profiles from horizontal measurements at locations show in Figure 6-22

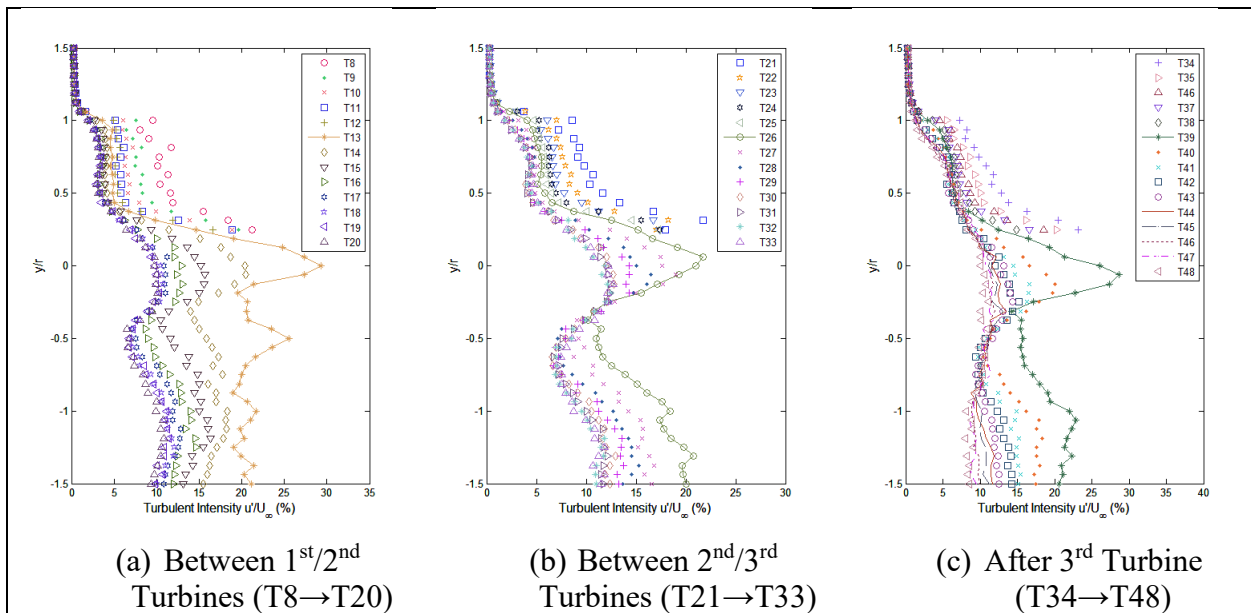


Figure 6-28. Turbulence intensity profiles for three vertical measurement regions at locations shown in Figure 6-16.

The turbulent intensity profiles shown similar trends as with the single and dual turbine tests.

The effect of multiple turbines on the velocity deficit and turbulent intensity can be better seen by plotting the deficit and intensity at normalized distances from the first turbine as shown in

Figure 6-29 and Figure 6-30.

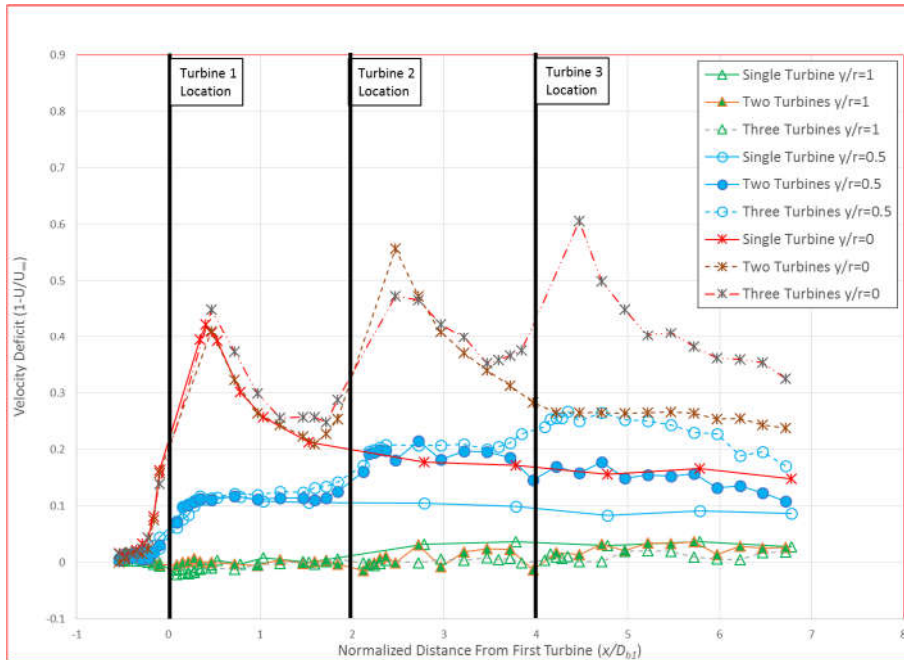
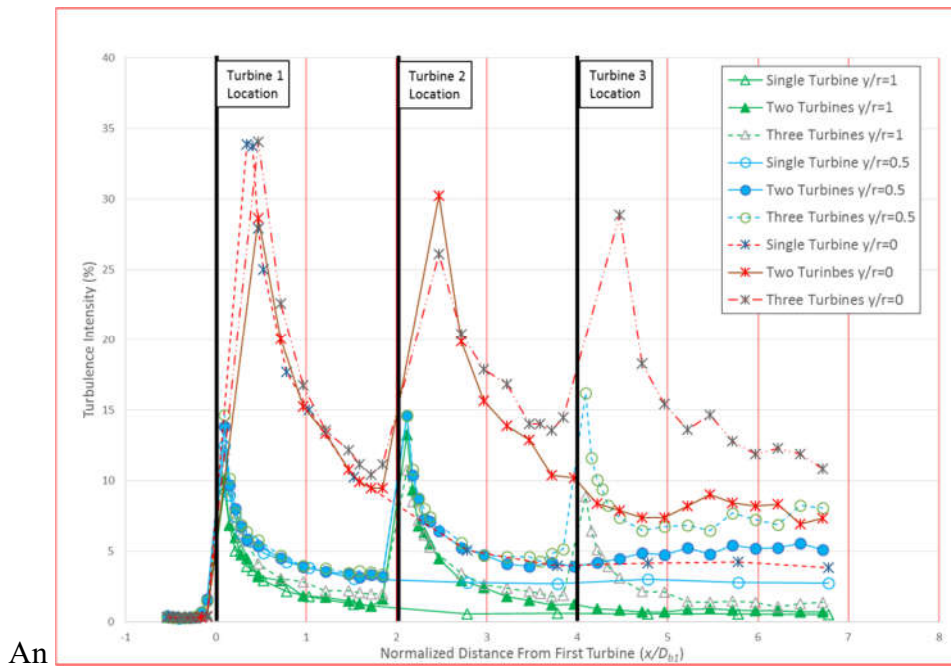


Figure 6-29. Comparison of velocity deficit with multiple turbines.



An

Figure 6-30. Comparison of turbulence intensity with multiple turbines.

Since experiments with multiple turbines and hot-wire calibrations were performed on different dates, the graphs show excellent repeatability in the measurements as indicated by nearly

identical values in the deficit and turbulence intensity values upstream of the first turbine, between the first and second turbine, and between the second and third turbine.

Figure 7-29 also shows the velocity deficit along the shear layer $y/r=1$ is unaffected by the number of turbines and the deficit at the centerline appears proportional to the number of turbines. For these experiments, turbulence generated from the tower was substantial and appeared to have a significant effect on the downstream deficit. The additional turbulence from the tower highlights the importance of including the tower in numerical studies.

6.3 High Speed Camera Imaging

In addition to hot wire measurements, high speed filming was performed using a Photron Mini UX50 camera set to record at 2000 frames/sec using 1280 x 1024 pixel resolution. The camera had a 4 GB internal hard drive which limited the recording time to 1.09 sec and 2180 total frames. A low cost fog machine was used to introduce a non-toxic, high density, oil-based mist at the inlet of the wind tunnel. Multiple trials were attempted to direct the mist toward the center of the hub, but that did not always occur. While the high speed imaging did not yield any quantitative results, it did provide qualitative information about the evolution of vortices in the wake and the turbulent structure in the wake. Figure 6-31 shows a clear vortex in the wake created from the rotor blades and the vortex appears to break down approximately 2-3 rotor diameters downstream.

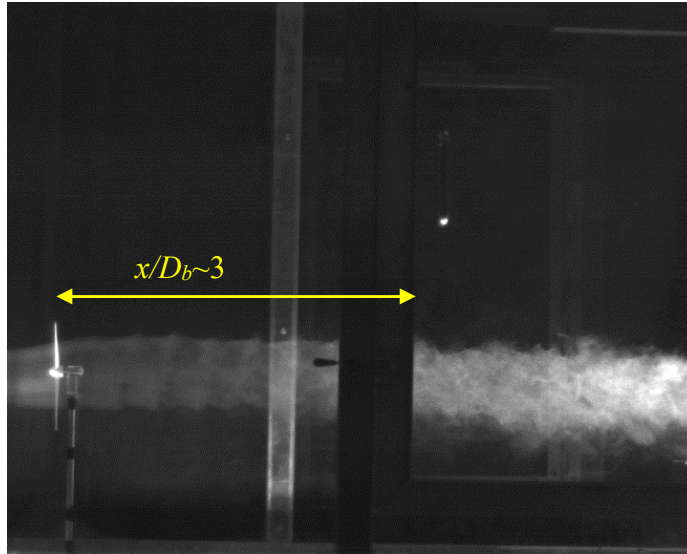


Figure 6-31. High speed images showing wake vortices from a single turbine

The wake is obscured by the frame of the test section access door shown in Figure 4-1; however, the vortex dissipation appears to coincide with the x/D_b location where velocity deficit and turbulence intensity become nearly constant as shown in Figure 6-11 and Figure 6-14. There appears to be a trend that the wake shifts downward after the vortices have dissipated. The apparent shift could be due to gravity, phase change in the oil mist, or a general meandering. Figure 6-32 shows the vortex and turbulence pattern in the wake of two turbines spaced two rotor diameters apart and Figure 6-33 shows the wake with three turbines at the same spacing. Figure 6-32 shows a distinct line of fluid in the free stream ahead of the first turbine and does not appear

to be significantly influenced by the first turbine and somewhat by the second turbine; this suggests some wake expansion is taking place after the second turbine.

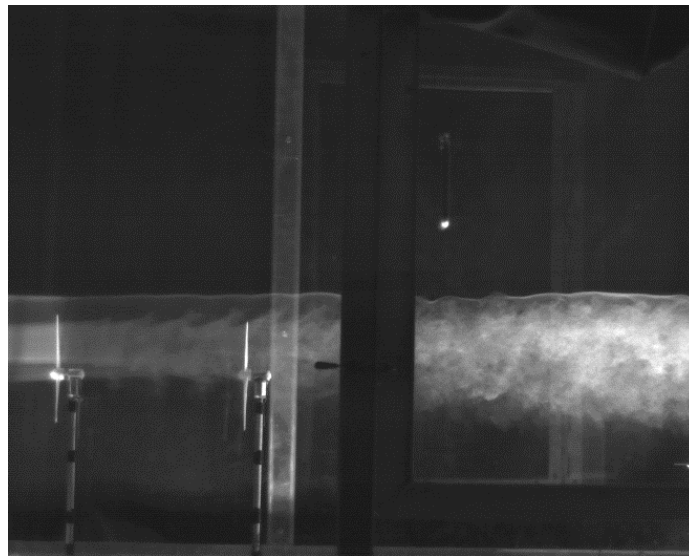


Figure 6-32. High speed image showing wake vortex and turbulence from two turbines spaced 2 rotor diameters apart



Figure 6-33. High speed image showing wake vortex and turbulence from three turbines spaced 2 rotor diameters apart

The wake growth may not be truly represented due to density changes of the oil mist. Figure 6-33 appears to show more interaction between the free stream and the turbine wakes, but all images are greatly influenced by the initial location of the oil mist stream. The location of the

mist was difficult to control and required considerable trial and error to get the stream in line with the turbines.

7 Computational Study

For this study, two different methods were used to simulate the wind turbine: a direct model approach and an actuator disk method. In the direct model method, the computational domain was divided into rotating and stationary subdomains with the blade surfaces discretized in the rotating subdomain. In the actuator disk method, the rotating blades were simulated using the Virtual Disk model available within Star CCM+.

7.1 Computational Domains and Boundary Conditions-Direct Model

Experimental results, discussed in Section 6, indicated the wind turbine rotational speed was dependent on the location of the vertical arm of a 3-axis traverse system used to automate positioning of a hot wire probe. With the traverse arm located near the wind turbine and the wake, flow directed around the traverse arm affected the blade speed and wake velocity. Having the blade speed and wake dependent on the traverse arm location creates a challenge for CFD simulations in that the location of the traverse has to be accounted for at each measurement location. In essence, the computational domain would have to be unique for each measurement point made in the vertical and lateral directions. As a compromise, multiple CFD models were created with a simulated traverse arm at specific downstream locations and only measurements in the vertical plane were used for comparison. Figure 7-1 to Figure 7-4 show the computational domains for each of the simulations with the traverse arm located at specific positions.

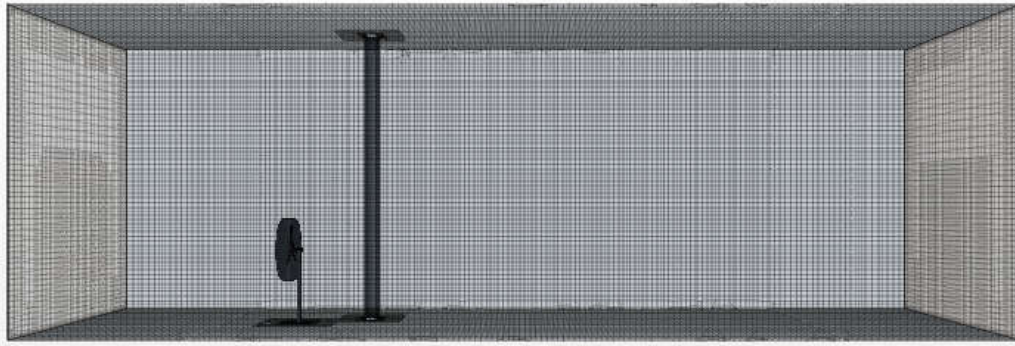


Figure 7-1. Computational domain of direct rotor model with traverse arm located at $x/D_b \sim 1$

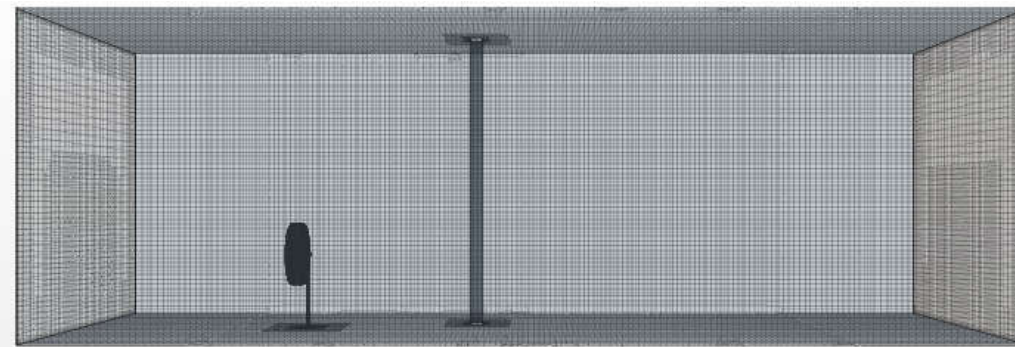


Figure 7-2. Computational domain of direct rotor model with traverse arm located at $x/ D_b \sim 3$

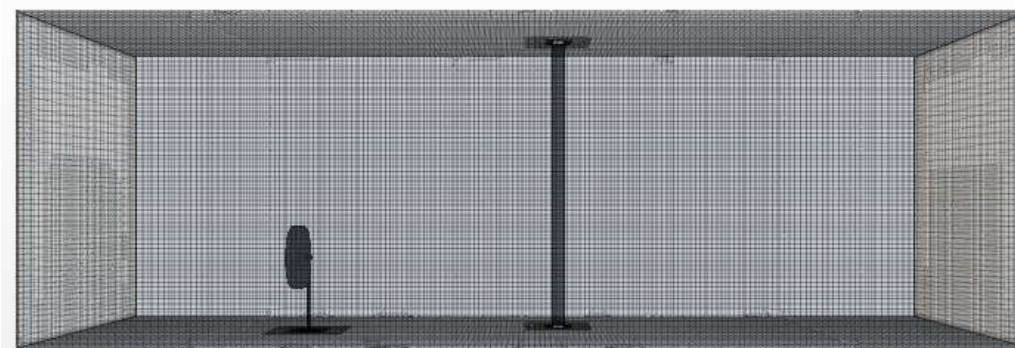


Figure 7-3. Computational domain of direct rotor model with traverse arm located at $x/ D_b \sim 5$.

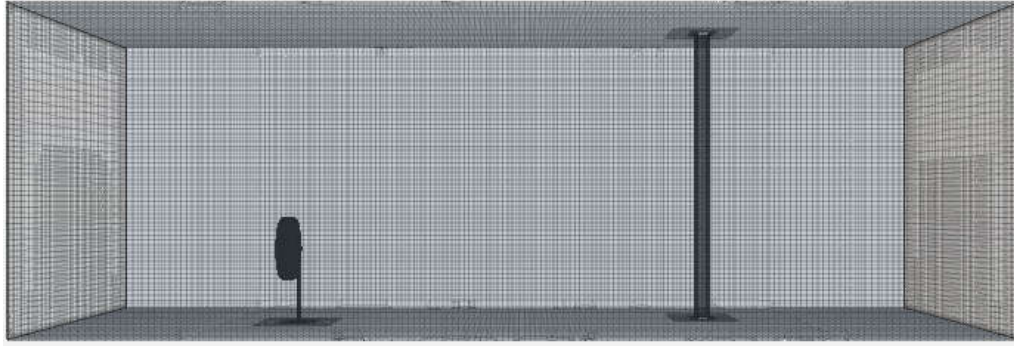


Figure 7-4. Computational domain of direct rotor model with traverse arm located at $x/D_b \sim 8$.

The domains were chosen to simulate the turbine installed in a wind tunnel with dimensions of 1.21m x 1.21m x 2.44m. The turbine blade is located 0.30 m downstream of the inlet. Each domain was separated into two subdomains to facilitate simulating the rotation of the blade using steady state Moving Reference Frame (MRF) and transient Rigid Body Motion (RBM) approaches.

The MRF model is a steady state approximation in which cell regions move at different rotational or translational speeds. The flow in the moving region is solved using transformed continuity and momentum equations. It is important to note that the MRF does not change the position of the cell vertices and the rotor blades are frozen in space; forces are imposed on the cells that are induced by the rotation. The ‘frozen rotor’ approach results in a solution that represents the time-averaged flow. At the interface between the regions, the local reference frame is transformed to allow flow variables in one region to be used to calculate fluxes at the boundary of adjacent regions. In the RBM method, the mesh vertices of the rotor region move to provide a time-accurate transient solution. The results from the steady state MRF solution were used as the initial condition for the transient RBM solution.

The rotating subdomain shown in Figure 7-5 contains the grid elements of the blade and a 0.25 m region enclosing the blade. A new rotating reference frame was established for this

subdomain with the axis of rotation set through the blade centerline and parallel to the 2.44 m tunnel length. The stationary subdomain included the tunnel, inlet and outlet sections, tunnel walls, tower, and nacelle. A mass flow boundary condition was applied at the inlet with the initial turbulence kinetic energy, k , and turbulent dissipation rate, ε , specified as 6.69E-04 J/kg and 1.0E-04 m²/s³, respectively. The initial values for k and ε were determined from:

$$k = \frac{3}{2}(IU_{\infty})^2 \quad (7.1)$$

$$\varepsilon = \frac{C_{\mu}^{3/4}k^{3/2}}{\ell} \quad (7.2)$$

$$\ell = 0.07L \quad (7.3)$$

The turbulence length scale, ℓ , in equation (7.3) is a physical quantity that represents the size of the large eddies that contain energy in turbulent flows. The 0.07 factor is based on the maximum mixing length in turbulent pipe flows. The characteristic length, L , is often taken as the hydraulic diameter, but in this research, the characteristic length was set to the height of the wind turbine. The turbulence intensity, I , was set to 0.0032 based on wind tunnel measurements and the turbulence model constant is usually given as $C_{\mu} = 0.09$. With the traverse arm located at the farthest position from the inlet, CFD simulations were performed using the parameters listed in Table 7-1. The Reynolds number listed was calculated based on the blade diameter as

$$Re = \frac{\rho U_{\infty} D_b}{\nu} \quad (7.4)$$

with $\rho=1.8415$ kg/m³, $D_b= 20.32$ cm, and $\nu=1.85508E-05$ Pa-s. The tip speed ratio, λ , is defined as

$$\lambda = \frac{\omega D_b}{2U_{\infty}} \quad (7.5)$$

For other simulations where the traverse arm was located at various x/D_b location, only the 11.62 kg/s and 1640 rpm parameters were used.

Table 7-1. Mass flow inlet and turbine speed rotation settings for CFD simulations

| Mass Flow [kg/s] | Free Stream Velocity [m/s] | Turbine Speed [rpm] | Turbine Reynolds Number, Re | Tip Speed Ratio, λ |
|------------------|----------------------------|---------------------|-------------------------------|----------------------------|
| 6.29 | 3.57 | 800 | 7.21E+04 | 2.37 |
| 8.74 | 4.97 | 1200 | 1.00E+05 | 2.56 |
| 11.62 | 6.60 | 1640 | 1.33E+05 | 2.63 |
| 13.65 | 7.75 | 2000 | 1.56E+05 | 2.73 |

A pressure outlet boundary condition was applied at the outlet and smooth wall, no-slip boundary conditions were applied to the tunnel walls, nacelle, traverse, tower, and blade surfaces.



Figure 7-5. Rotating subdomain using trimmed mesh model with prism layer meshing at rotor surfaces

7.2 Grid Generation-Direct Model

Meshing in Star CCM+ is mostly automated and based on the meshing model selected and cell size, cell growth, and refinement settings. For this research, the trimmer mesh model was chosen

because the domain contains a substantial number of cells where the flow direction is aligned with the Cartesian coordinate system and because it produces a fast, high-quality mesh.

A region-based meshing scheme was employed to coincide with the different physics models used for the rotating and stationary regions; however, additional constraints were added to the surfaces for boundary layer resolution and to improve the mesh quality. The rotor region consisted of predominantly hexahedral cells, but the automated meshing routine also created a mix of hexahedral, wedge, pyramid, and polyhedral cells based on localized prism meshing and mesh size definitions.

Six layers of orthogonal prismatic cells, as shown in Figure 7-6, were added next to the turbine blade surfaces to ensure the boundary layer was well defined for laminar flow conditions and to ensure the wall $y^+ < 5$ for turbulence modeling. Similar prism meshes were added to the surfaces of the tower, nacelle, tunnel walls, and traverse arm.

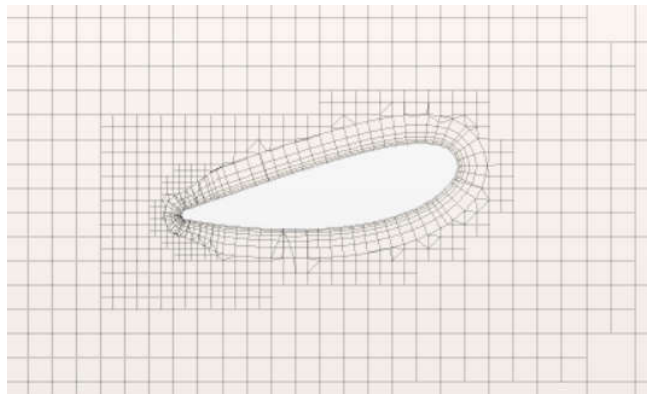


Figure 7-6. Prism layer meshes at blade surface

The base mesh size was initially set to 0.04 m and refinement through the domain was controlled by growth parameters. A rectangular grid refinement, as seen in Figure 7-7, was added to reduce the element volume in the wake. The mid-plane mesh also shows downstream refinement as a result of the traverse arm.

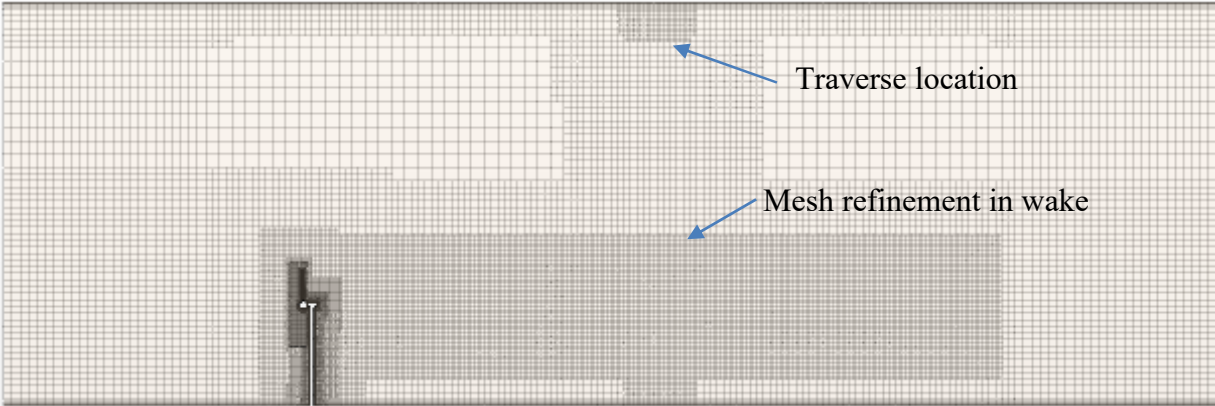


Figure 7-7. Mesh at vertical mid-plane of computational domain with traverse arm at $x/D \sim 5$

Mesh quality metrics was established for improved accuracy and convergence as follows:

- Maximum cell skewness angle $< 90^\circ$ for all cells
- Face validity > 0.95
- Face quality > 0.2
- Volume change $> 1E-10$

For cells that did not meet minimum quality criteria, the Cell Quality Remediation tool in Star CCM+ was used. The tool identifies low-quality cells and their neighbors and modifies the gradients in those cells to improve solution robustness. The remediation is confined to the immediate vicinity of bad cells, so the influence on the solution accuracy is minimal.

7.3 Computational Domains and Boundary Conditions-Actuator Disc

In the actuator disk method, which STAR-CCM+ refers to as the Virtual Disk model, the rotor subdomain was replaced with a thin disc. The main advantage of using an actuator disk method is the mesh size significantly reduced by not having to mesh the rotor. The lower mesh size makes the AD method well suited for simulating multiple wind turbines and using more resource intensive turbulence modeling methods such as LES. As with the direct rotor model for a single turbine, simulations were created with the traverse arm at specific locations. Figure 7-8

shows the domain for a single turbine with the traverse arm at its maximum distance from the turbine; domains with the traverse at other locations are not shown.

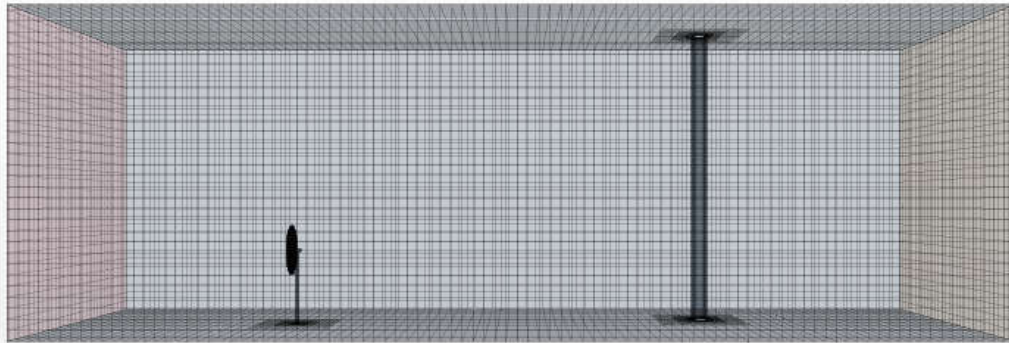


Figure 7-8. Computational domain using a Virtual Disk model and a single turbine; traverse located at max position $x/D \sim 7$

The boundary conditions for the AD simulations were identical to the direct model as far as inlet flow conditions, initial conditions, outlet conditions, and wall boundaries were concerned. Star CCM+ has three Virtual Disk options available to model the actuator disk, but only two are relevant to wind turbines. The simplest model is based on 1-D momentum theory with wake rotation and requires the tabular input of the thrust coefficient versus wind speed to generate momentum source terms. The model selected for this research is based on Blade Element Momentum (BEM) theory to generate momentum source terms. The model was primarily developed to study flow interaction between rotors and the fuselage in helicopters. With judicious selection of the rotating axis, the method can be applied to wind turbines. The model requires tabular input for the blade geometry and airfoil performance (i.e. lift and drag coefficients). The Virtual Disk model parameters were entered into the simulation based on the blade characteristics established in Section 3 and using lift and drag coefficients generated from QBlade. Disk rotation speeds were matched with experimental values as best as possible given the dependence on traverse arm location.

7.4 Grid Generation-Actuator Disk

Except for the rotor, the meshing parameters for the AD method were nearly identical to the direct mesh for all boundaries. The disk in each model was meshed according to the guidelines suggested in the STAR-CCM+ documentation [74], where the resolution must be fine enough to allow proper generation of momentum forces at the disc cell volumes.

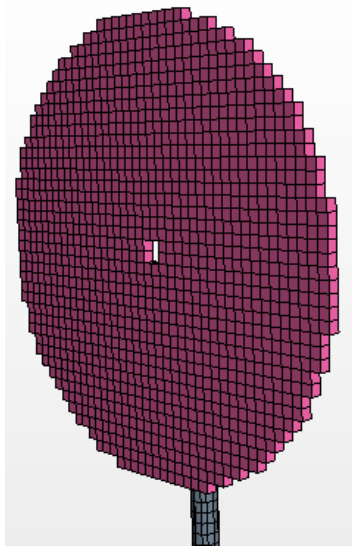


Figure 7-9. Virtual Disk mesh

Figure 7-9 shows a typical disk mesh. The disk thickness must be 10-15% greater than the cell size of the volume mesh where the disk is located. The software will generate an error if the resolution on the blade surface is too fine or too coarse. Figure 7-10 shows the mesh at the mid-plane of the computational domain with the traverse positioned at $x/D_b \sim 8$. As with the direct model, a rectangular refinement area was added downstream of the disk.

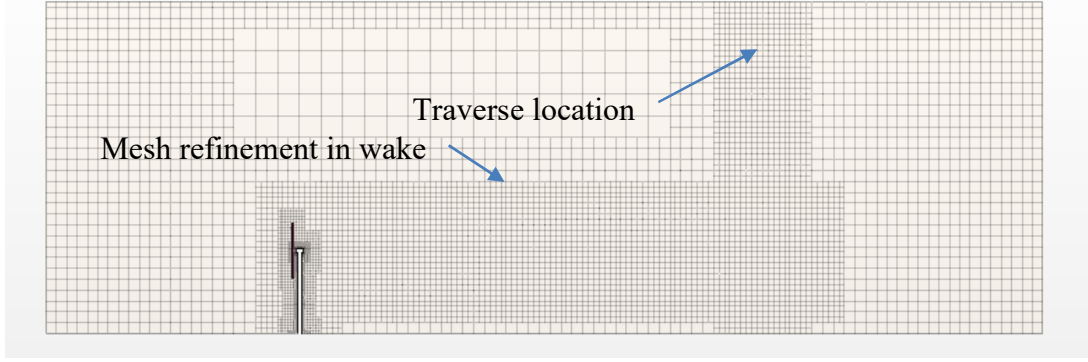


Figure 7-10. Computational grid using actuator disk and traverse located at $x/D_b \sim 8$

7.5 Governing Equations

All CFD studies are based on the fundamental equations of continuity, momentum, and energy. For this study, the fluid domain is considered isothermal and incompressible, so the energy equation is ignored. The conservation of mass and momentum yields the governing equations (written in index notation) for the flow of a compressible, Newtonian fluid:

Continuity Equation:

$$\frac{\partial \rho}{\partial t} + \frac{\partial}{\partial x_j} (\rho u_j) = 0 \quad (7.6)$$

Momentum (Navier-Stokes):

$$\frac{\partial (\rho u_i)}{\partial t} + \frac{\partial}{\partial x_j} (\rho u_i u_j) = \frac{\partial}{\partial x_j} \left(-p \delta_{ij} + \mu \left(\frac{\partial u_i}{\partial x_j} + \frac{\partial u_j}{\partial x_i} \right) - \frac{2}{3} \mu \frac{\partial u_k}{\partial x_k} \delta_{ij} \right) \quad (7.7)$$

The momentum equation (7.7) is developed by applying Newton's second law of motion to a three-dimensional fluid particle and is referred to as the Navier-Stokes (N-S) equations. These equations form a close set of four equations with four unknowns (component velocities u , v , w , and pressure, p). A full 3-D analytical solution to these nonlinear equations does not exist, but exact solutions are available for a variety of flows with simplifying assumptions. When using the MRF and RBM methods with a rotating region, the absolute velocity vector \vec{u} is replaced by a velocity relative to the rotating reference frame \vec{u}_r with the relation:

$$\vec{u} = \vec{u}_r + \vec{\omega} \times \vec{r} \quad (7.8)$$

so that the transformed Navier-Stokes equations, in terms of \vec{u}_r include terms for the Coriolis acceleration and centripetal acceleration; the transformed equations are not presented here. For turbulent flows, the instantaneous velocity and pressure variables are considered to be comprised of a time-averaged mean and a perturbation:

$$u_i = \bar{u}_i + u'_i \quad (7.9)$$

$$p = \bar{p} + p' \quad (7.10)$$

Inserting the instantaneous velocities and pressures into the N-S equations and time averaging yields a set of Reynolds Averaged Navier-Stokes (RANS) equations:

$$\frac{\partial \bar{u}_i}{\partial x_j} = 0 \quad (7.11)$$

$$\frac{\partial(\rho \bar{u}_i)}{\partial t} + \frac{\partial}{\partial x_j}(\rho \bar{u}_i \bar{u}_j) = \frac{\partial}{\partial x_j} \left(-\bar{p} \delta_{ij} + \mu \left(\frac{\partial \bar{u}_i}{\partial x_j} + \frac{\partial \bar{u}_j}{\partial x_i} \right) - \rho \overline{u'_i u'_j} \right) \quad (7.12)$$

The momentum equation (7.12) has an additional six unknown terms representing the convective momentum due to the velocity fluctuations. The other terms, $-\rho \overline{u'_i u'_j}$, are called the turbulent stresses and without the density, $\overline{u'_i u'_j}$, they are referred to as the turbulent kinematic stresses or Reynolds stresses. The main goal in turbulence modeling is to develop a suitable closure method to predict the Reynolds stresses. Different types of turbulence closure methods have been developed, each with its own set physics, advantages, disadvantages, and applicability for certain types of flows. Versteeg and Malalasekera [75] provide a good summary of the most popular methods.

In this research, the Reynolds Stress Model (RSM), also referred to as the Reynolds Stress Transport (RST) model, was selected for turbulence closure because it accounts for the anisotropy in the wake due to strong swirling motion and streamline curvature. Few studies exist using the

RSM closure method for wind turbine analysis because it is a more advanced technique than one or two-equation turbulence models, often numerically unstable, and computationally expensive. Studies that do exist use an actuator disk to simulate the rotor. In addition to six equations needed to solve for the Reynolds stress components, an additional model equation is needed for the turbulent dissipation, ε . The RSM modeling strategy originated from Launder, et al. [76] and variations of the transport equations have been developed over the years. Star CCM+ offers a choice of four different Reynolds stress transport models: a linear pressure strain, quadratic pressure strain, two-layer linear pressure strain, and elliptic blending. For this research, the linear pressure strain was selected for stability and because it allows for a hybrid y^+ wall treatment for coarse and fine meshes.

Beginning with the exact transport model discussed in Sarkar and Balkrishnan [77], a set of differential equations for the transport of the kinematic Reynolds stresses can be written, assuming incompressible, isothermal flow, as

$$\begin{aligned}
 \underbrace{\frac{D(\overline{u'_i u'_j})}{Dt}}_{\text{Convection}, C_{ij}} &= - \underbrace{\left(\overline{u'_i u'_k} \frac{\partial \bar{u}_j}{\partial x_k} + \overline{u'_j u'_k} \frac{\partial \bar{u}_i}{\partial x_k} \right)}_{\text{Production}, P_{ij}} + \underbrace{\frac{\overline{p'}}{\rho} \left(\frac{\partial u'_i}{\partial x_j} + \frac{\partial u'_j}{\partial x_i} \right)}_{\text{Pressure Strain}, \phi_{ij}} \\
 &- \underbrace{\frac{\partial}{\partial x_k} \left(\overline{u'_i u'_j u'_k} + \frac{\overline{p' u'_i}}{\rho} \delta_{jk} + \frac{\overline{p' u'_j}}{\rho} \delta_{jk} \right)}_{\text{Diffusion}, D_{ij}} - v \frac{\partial \overline{u'_i u'_j}}{\partial x_k} \\
 &+ \underbrace{\frac{\partial}{\partial x_k} \left(2\nu \frac{\partial \overline{u'_i u'_j}}{\partial x_k} \right)}_{\text{Dissipation}, \varepsilon_{ij}}
 \end{aligned} \tag{7.13}$$

In equation (7.13), the convection terms, C_{ij} , production terms, P_{ij} , and viscous diffusion terms (4th term in D_{ij}), require no additional modeling effort. The pressure diffusion terms (2nd and 3rd terms in D_{ij}) are neglected because the transport due to pressure fluctuations are negligible

compared to velocity fluctuations. The remaining portion of D_{ij} is modeled with the isotropic formulation from Lien and Leschziner [78] as

$$D_{ij} = \frac{\partial}{\partial x_k} \left(\left(\nu + \frac{\mu_t}{\sigma_k} \right) \frac{\partial \overline{u'_i u'_j}}{\partial x_k} \right) \quad (7.14)$$

where the Prandtl number for the turbulence kinetic energy is $\sigma_k = 0.82$ and the turbulent viscosity is computed from equation (7.15).

$$\mu_t = \rho C_\mu \frac{k^2}{\varepsilon} \quad (7.15)$$

The turbulent dissipation tensor, ε_{ij} , is modeled by assuming isotropy of the small dissipative eddies as shown in equation (7.16)

$$\varepsilon_{ij} = \frac{2}{3} \varepsilon \delta_{ij} \quad (7.16)$$

with the transport equation for the turbulent dissipation rate, ε , computed from equation (7.17).

$$\frac{D(\rho\varepsilon)}{Dt} = \frac{\partial}{\partial x_j} \left(\left(\mu + \frac{\mu_t}{\sigma_\varepsilon} \right) \frac{\partial \varepsilon}{\partial x_j} \right) + C_{\varepsilon 1} \rho \frac{\varepsilon}{k} \frac{1}{2} P_{ii} - C_{\varepsilon 2} \rho \frac{\varepsilon^2}{k} \quad (7.17)$$

The pressure-strain correlation term, ϕ_{ij} , is modeled based on the linear formulation of Gibson and Launder [79] with components for the slow pressure-strain, rapid pressure-strain, slow wall-reflection, and rapid wall-reflection:

$$\phi_{ij} = \phi_{ij,1} + \phi_{ij,2} + \phi_{ij,1w} + \phi_{ij,2w} \quad (7.18)$$

The terms in equation (7.18) are given as

$$\phi_{ij,1} = -C_1 \frac{\varepsilon}{k} \left(\overline{u'_i u'_j} - \frac{2}{3} k \delta_{ij} \right) \quad (7.19)$$

$$\phi_{ij,2} = \phi_{ij,1} = -C_2 \left(P_{ij} - \frac{1}{3} P_{kk} \delta_{ij} \right) \quad (7.20)$$

$$\phi_{ij,1w} = C_{1w} \frac{\varepsilon}{k} \left(\overline{u'_i u'_m} n_k n_m \delta_{ij} - \frac{3}{2} \overline{u'_i u'_k} n_j n_k - \frac{3}{2} \overline{u'_j u'_k} n_i n_k \right) F_w \quad (7.21)$$

$$\phi_{ij,2w} = C_{2w} \frac{\varepsilon}{k} \left(\phi_{km,2} n_k n_m \delta_{ij} - \frac{3}{2} \phi_{im,2} n_j n_k - \frac{3}{2} \phi_{jk,2} n_i n_k \right) F_w \quad (7.22)$$

The coefficient, F_w , is function of the normal distance to the nearest wall, d_m .

$$F_w = \min \left[\frac{k^{\frac{3}{2}}}{C_l \varepsilon d_m}, 1.4 \right] \quad (7.23)$$

The pressure-strain interaction serves to promote a reversion toward isotropy of the stress field and redistribute energy amongst the normal Reynolds stresses. Corrections are made to account for influence of wall proximity on the pressure-strain terms. Values for the constants and coefficients used for the linear pressure-strain RSM equations are listed in Table 7-2.

Table 7-2 Coefficients for the linear pressure-strain model

| C_μ | σ_ε | σ_k | $C_{\varepsilon 1}$ | $C_{\varepsilon 2}$ | C_1 | C_2 | C_{1w} | C_{2w} | C_l |
|---------|----------------------|------------|---------------------|---------------------|-------|-------|----------|----------|-------|
| 0.0655 | 1 | 0.82 | 1.44 | 1.92 | 1.8 | 0.6 | 0.5 | 0.3 | 2.5 |

7.6 Numerical Method

Both steady and unsteady incompressible flow simulations were performed on the direct-modeled wind turbine. Since the actuator disk concept requires time averaging to estimate body forces, the actuator disk simulation was only performed as a steady incompressible flow. The segregated solver of Star CCM+ was used which solves the flow equations (one for each velocity component and one for pressure) in a second-order, uncouple fashion. The under-relaxation factors were set to 0.7 for velocity and 0.2 for pressure. Full details of the segregated solver are not provided in the documentation; however, the segregated solver is described as a ‘‘Rhie-and-Chow-type coupling combined with a SIMPLE-type algorithm’’. The solver description is in reference to a momentum interpolation method for non-staggered grids proposed by Rhie and

Chow [80] and an iterative solution strategy developed by Patankar and Spalding [81]. For implicit unsteady simulations, the results of the steady simulations were used as initial conditions. A second-order temporal discretization scheme was used with a 2.083E-04 second time step and 20 inner iterations. The total simulation time was set at 0.375 seconds which represents ten revolutions of the rotor at the set rotation speed; each time step represented 2 degrees of blade rotation. The convective Courant Numbers were kept below 1 in the non-rotating region and less than 3 in the rotating region to maintain numerical stability and prevent the solution from diverging. For all simulations, values of the residuals, rotor thrust, rotor moment, inlet mass flow, outlet mass flow, and average blade surface pressures (direct model only) were monitored for convergence. The MRF and actuator disk simulations were allowed to run for 10,000 iterations. A typical residual plot is shown in Figure 7-11 for an MRF simulation and in Figure 7-12 for an actuator disk simulation.

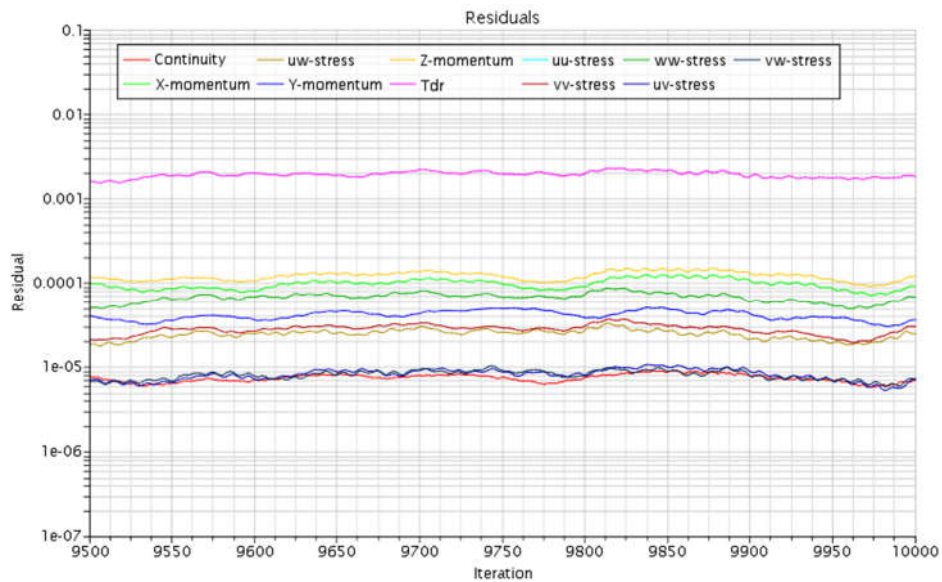


Figure 7-11. Typical residuals for last 500 iterations in direct model MRF simulations

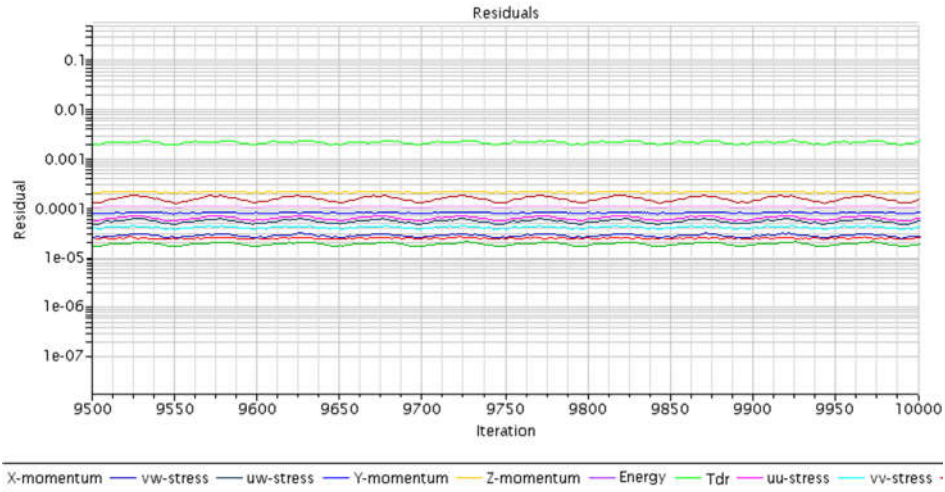


Figure 7-12. Typical residuals for last 500 iterations in actuator disk simulations

All simulations were performed on the High-Performance Computing (HPC) cluster at the University of Wisconsin-Milwaukee. The HPC cluster includes 142 computing nodes with 8 cores per node for a total of 1136 cores 3616 GB total RAM. Batch processing was utilized to take advantage of the parallel computing architecture in Star CCM+.

7.7 Grid Sensitivity

A grid sensitivity analysis was performed to ensure the grid size did not influence the simulation results. Table 7-3 is a summary of the meshes used for the direct model method. Since the blade surface grid, wake refinement grids, and prism layer thickness were defined as a percentage of the base size, those cell sizes were reduced and the cell density increased. For each grid size, the thrust force and rotor torque were evaluated, and the velocity at the hub height at $x/D_b \sim 3$ was also evaluated. The thrust force and rotor torque changed less than 4% for all mesh sizes which was acceptable for this study. Changes in the velocity downstream were also acceptable given steady state convergence oscillations discussed earlier. For all grid resolutions, $y^+ < 5$ to ensure the boundary layer could be solved in the viscous sublayer. The medium mesh

density scheme was used for all transient simulations and simulations at different flow rates, blade speeds, and traverse arm locations.

Table 7-3. Grid sensitivity summary for direct modeled simulation with traverse located a maximum distance from turbine

| Grid | Rotating Domain Base Grid Size (m) | Stationary Domain Base Grid Size (m) | Wake Refinement Grid Size (%) | Rotating Subdomain Cell Count | Stationary Subdomain Cell Count | Thrust Force (N) | Rotor Torque (N-m) | Velocity $x/D_b \sim 3$ (m/s) |
|--------|------------------------------------|--------------------------------------|-------------------------------|-------------------------------|---------------------------------|------------------|--------------------|-------------------------------|
| Course | 0.035 | 0.050 | 40 | 1168423 | 1226284 | 0.299 | 0.0052 | 3.47 |
| Medium | 0.025 | 0.040 | 40 | 1885600 | 1837728 | 0.287 | 0.0051 | 3.81 |
| Fine | 0.025 | 0.030 | 40 | 1885611 | 3284888 | 0.298 | 0.0053 | 3.74 |

Table 7-4 is a summary of the meshes used in the actuator disk method. The approach was similar to the direct method and the medium mesh density scheme was also used for all simulations at different flow rates, blade speeds, and traverse arm locations. For the tower and nacelle, prism layer meshing was defined so that $y^+ < 5$ to ensure the boundary layers could be resolved.

Table 7-4. Grid sensitivity summary for the actuator disk simulation with traverse located a maximum distance from turbine

| Grid | Domain Base Grid Size (m) | Wake Refinement Base Grid Size (%) | Disk Surface Grid Size (%) | Cell Count | Thrust Force (N) | Rotor Torque (N-m) | Minimum Velocity $x/D_b \sim 3$ (m/s) |
|--------|---------------------------|------------------------------------|----------------------------|------------|------------------|--------------------|---------------------------------------|
| Course | 0.04 | 50 | 15 | 372646 | 0.36 | 0.011 | 3.92 |
| Medium | 0.03 | 25 | 10 | 726121 | 0.344 | 0.011 | 4.16 |
| Fine | 0.025 | 25 | 10 | 1671959 | 0.354 | 0.010 | 4.25 |

7.8 CFD Results and Comparison to Experimental Data

Figure 7-13 shows a series of line probes added to the simulation that correspond to experimental measurement locations listed in Appendix D. The measurement locations have been designated as S8, S9...S16 for measurement locations where $x/D_b < 1$. Figure 7-14 shows the similar line probes for measurement locations where $x/D_b > 1$ and measurement locations have been designated as S17, S18,...S23.

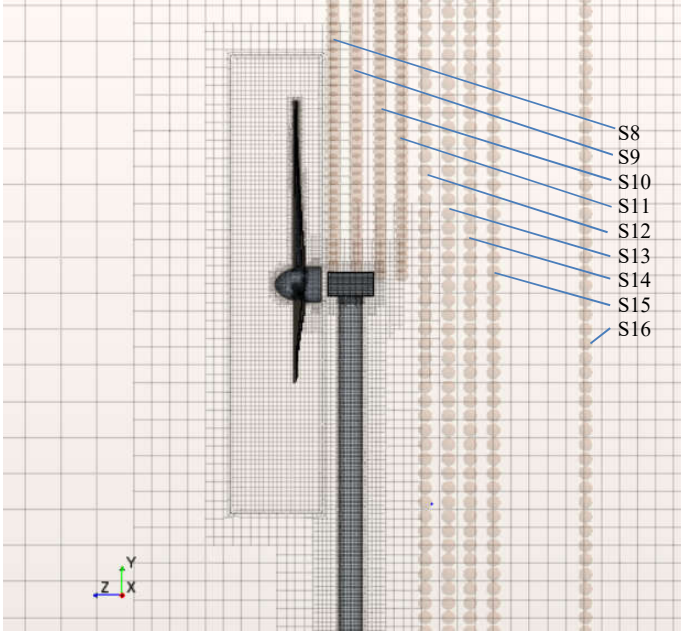


Figure 7-13. Experimental measurement locations for $x/D_b < 1$

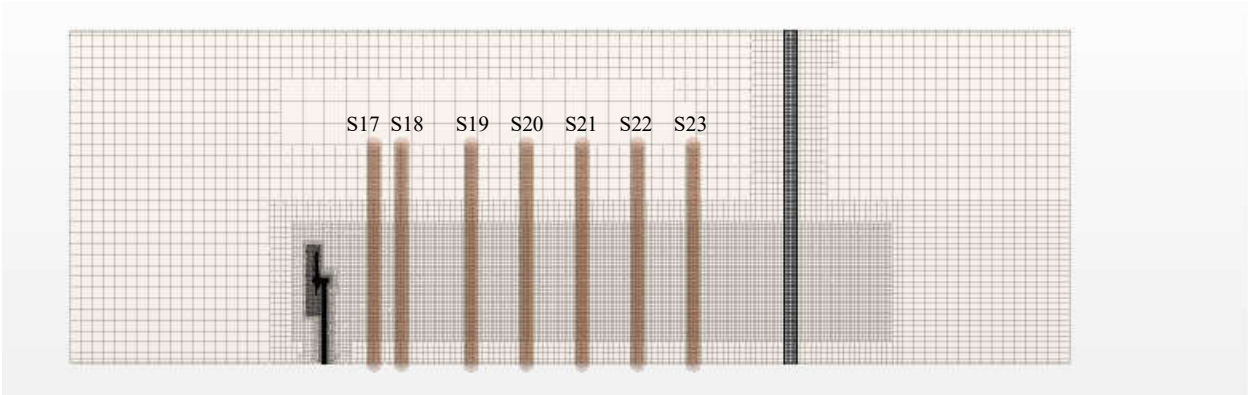


Figure 7-14. Experimental measurement locations for $x/D_b > 1$

As mentioned, the location of the traverse affected the velocity measurement at each location. To validate the application of the Reynolds stress model using experimental data, simulations were performed to compensate for the traverse location. Three additional models were created with the traverse positioned to correspond to measurements at $x/D_b \sim 1$, $x/D_b \sim 3$, $x/D_b \sim 5$. The locations were selected based on three regions having different turbulence characteristics. At $x/D_b \sim 1$, the vortex structure created at the blade tips is strong, while, in the $x/D_b \sim 3$ region, the vortices are mixing with the free stream the process of dissipating. At $x/D_b \sim 5$, the tip vortices have completely dissipated. Comparative measurement planes, as noted in Figure 7-14, are S17, S19, and S21.

Transient Rigid Body Motion (RBM) simulations were performed on the direct-modeled turbine using the 2-equation $k-\varepsilon$ and $k-\omega$ (SST) turbulence closure models for comparison to the RST closure method. Figure 7-15 shows the velocity deficit for each closure method at three different wake locations compared to the experimental measurements. There does not appear to be a significant difference in the closure method, but this could be due to the lack of turbulence in the free stream flow. It is believed the RST method would show improved results if the free stream flow contained turbulence and swirling motion consistent with real atmospheric conditions or if the velocity approached the turbine from different directions. The RST method does offer information on the Reynolds stresses which could prove more beneficial in evaluating real-world wake turbulence. As mentioned, a direct model simulation using RST has never been created. Thus, the focus of the remainder of this chapter is to present results of the simulations using RST and to show how well the RST method correlates to the experimental data.

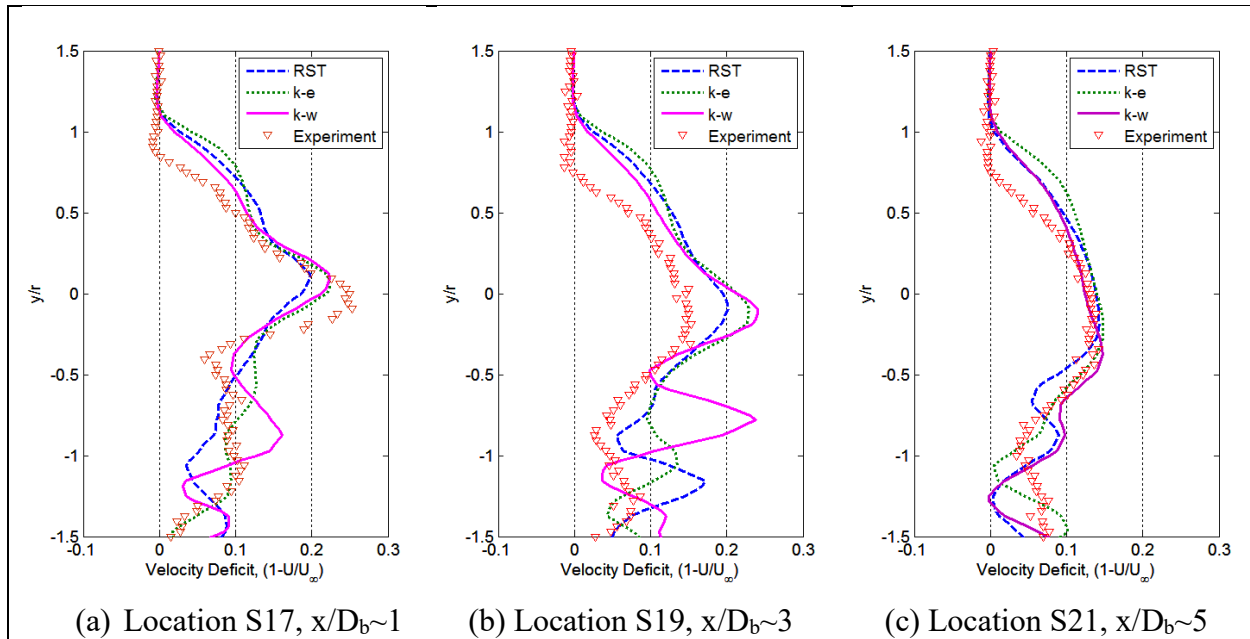


Figure 7-15. Comparison of turbulence closure models in predicting the velocity deficit using a Rigid Body Motion (RBM) method at three different wake locations.

Figure 7-16 through Figure 7-19 show velocity contours for each MRF simulation for a plane parallel to the bottom of the wind tunnel and a through the rotor centerline. The velocity contours represent the component parallel to the free stream. The magnitude of the free stream velocity for all contour plots was 6.6 m/s. In the simulation, the positive z-axis was defined toward the inlet of the wind tunnel; therefore, negative velocity values indicate flow direction parallel to the free stream toward the outlet of the wind tunnel.

Each velocity contour plot also shows the location of the experimental measurement location noted in Figure 7-13 and Figure 7-14. The velocity deficit behind the turbine is evident in the wake and there is a significant deficit behind the traverse arm. Comparing Figure 7-16, Figure 7-17, and Figure 7-18 with Figure 7-19, it is clear that flow directed around the traverse allows the wake velocity to recover faster than if the traverse was not there.

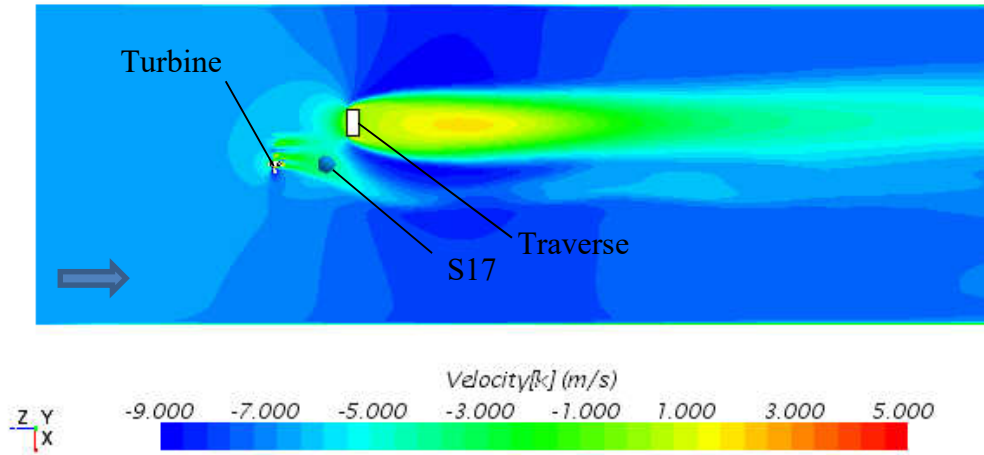


Figure 7-16. Plan view of velocity contour from MRF simulation with traverse located at $x/D_b \sim 1$

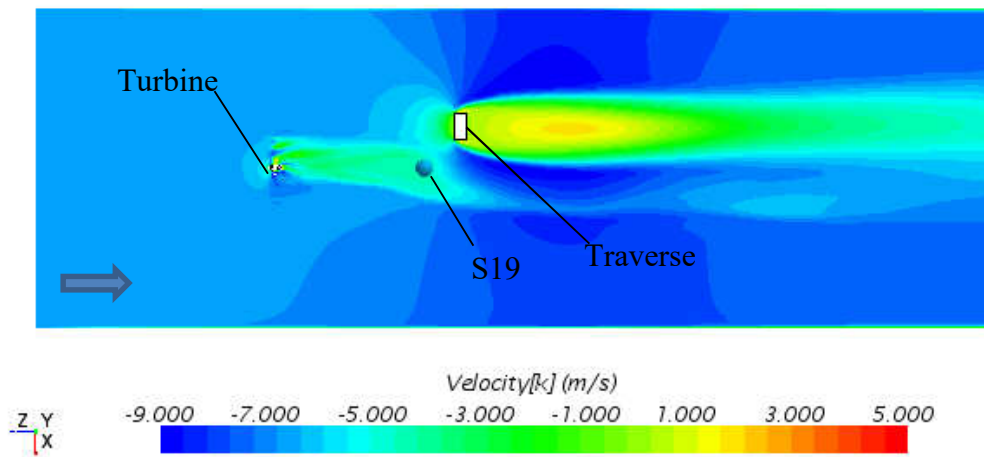


Figure 7-17. Plan view of velocity contour from MRF simulation with traverse located at $x/D_b \sim 3$

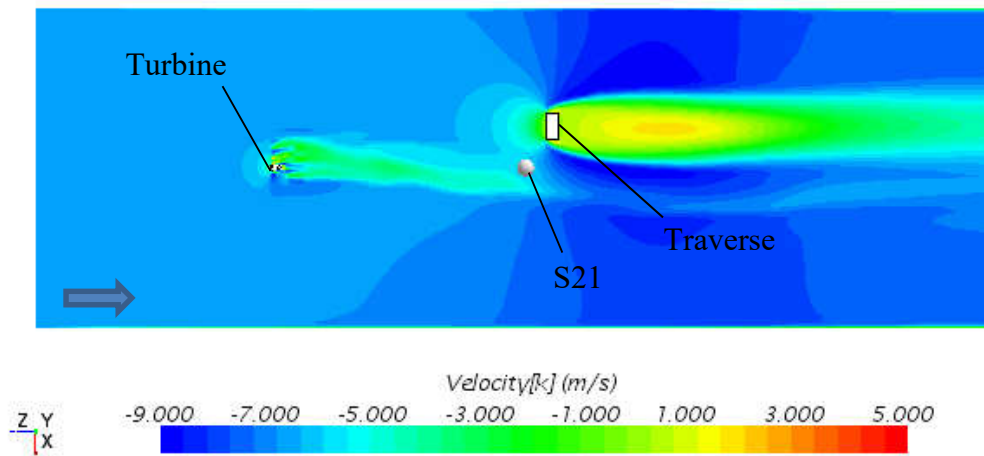


Figure 7-18. Plan view of velocity contour from MRF simulation with traverse located at $x/D_b \sim 5$

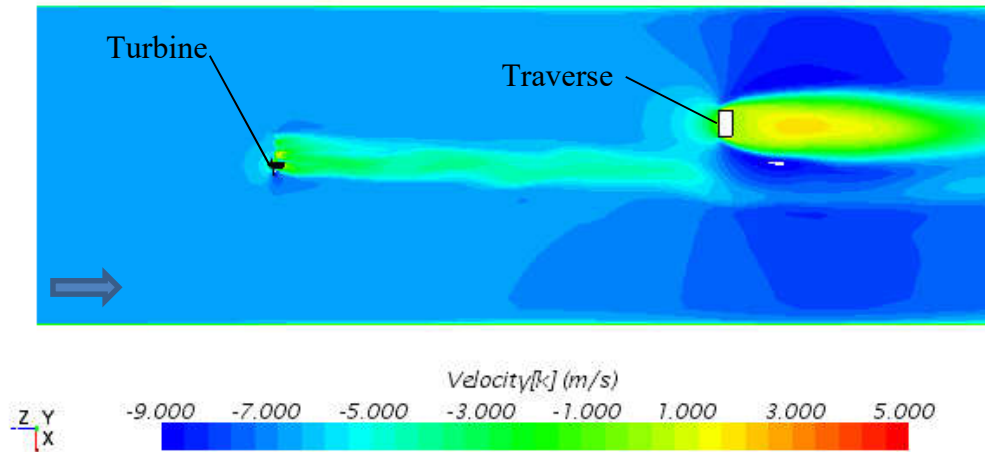


Figure 7-19. Plan view of velocity contour from MRF simulation with traverse located at $x/D_b \sim 8$.

In the RBM simulations, vortices in the wake are captured due to the time-dependent nature of the analysis. Vorticity is a vector field and a measure of the local rotation of the fluid. Figure 7-20 through Figure 7-22 show contour plots of the z-direction vorticity component with the traverse arm located at $x/D_b \sim 1$, $x/D_b \sim 3$, and $x/D_b \sim 5$, respectively. In the contour plots, positive values indicate rotation in the same direction as the turbine blades and negative values indicate rotation in the opposite direction of the turbine blades.

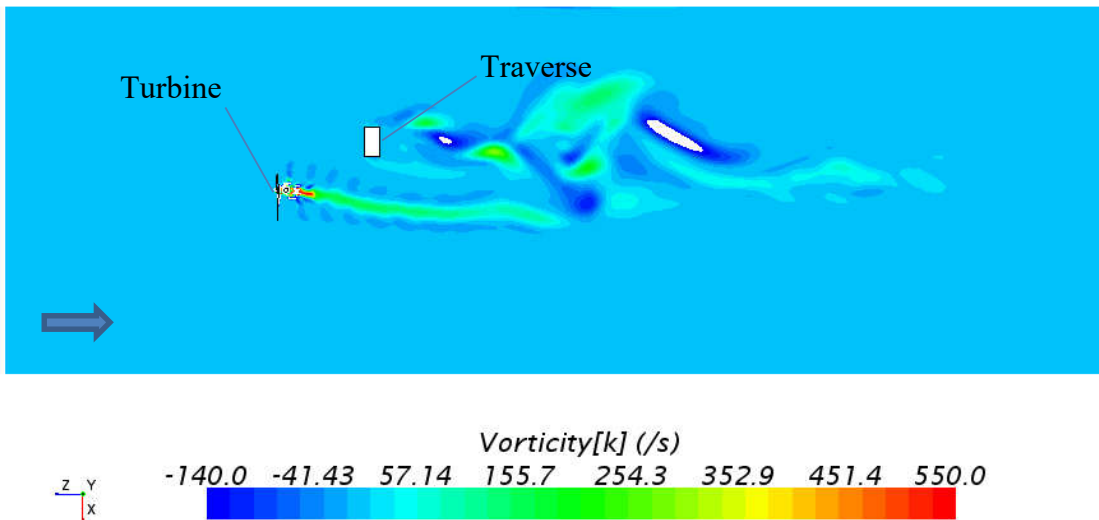


Figure 7-20. Plan view of z-axis vorticity contour from RBM simulation with traverse located at $x/D_b \sim 1$

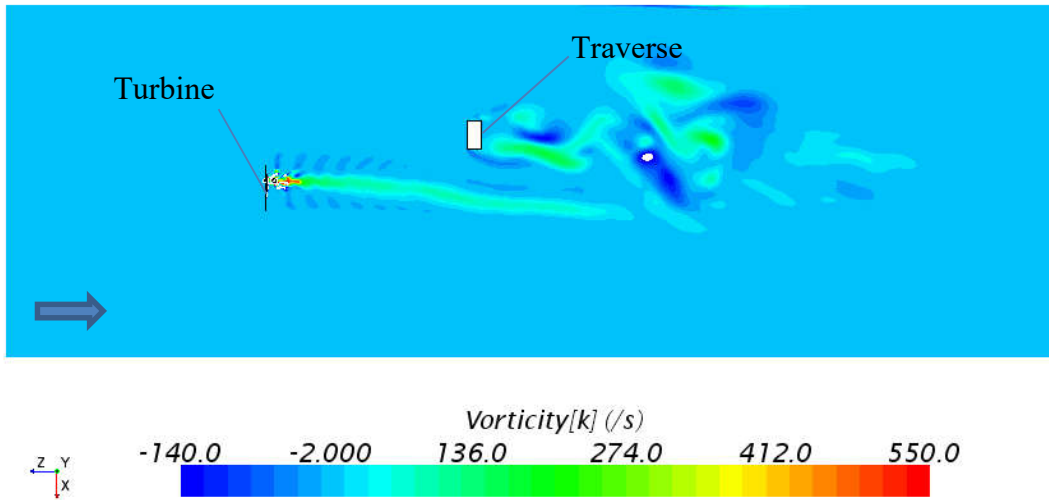


Figure 7-21. Plan view of z-axis vorticity contour from RBM simulation with traverse located at $x/D_b \sim 3$. The contour plots show the helical vortex structure in the wake that results from vortices shed at the blade tips. The helical vortex rotates in the opposite direction as the turbine blades. The contour plots also show vortices shed from the traverse arm.

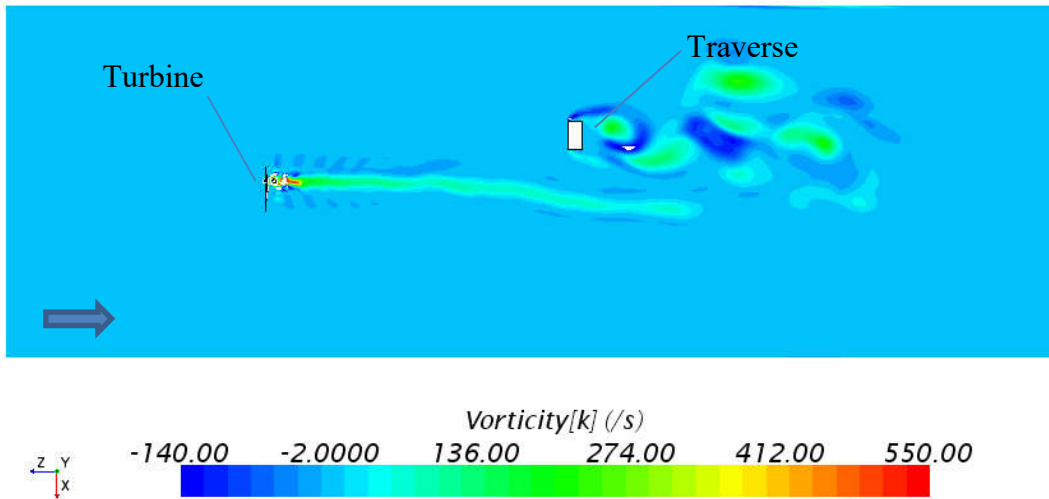


Figure 7-22. Plan view of z-axis vorticity contour from RBM simulation with traverse located at $x/D_b \sim 5$. As the traverse is moved farther away from the turbine, the turbine wake straightens and the wake behind the hub is extended as there is less mixing with the free stream flow. The wake behind the traverse appears to shorten, but this is likely a numerical effect due to the proximity to

the outlet boundary. The velocity contours for the actuator disk simulation show similar patterns as the direct model MRF simulation with flow directed around the traverse and the wake recovering sooner than without the traverse. Figure 7-23 shows an example of the velocity contour in the actuator disk simulation with the traverse located at $x/D_b \sim 5$. As with the direct model simulation, rotation of the disk was clock-wise when facing the ($-z$) direction. Streamlines have been added to show how the wake rotates in the opposite direction as the rotor disk.

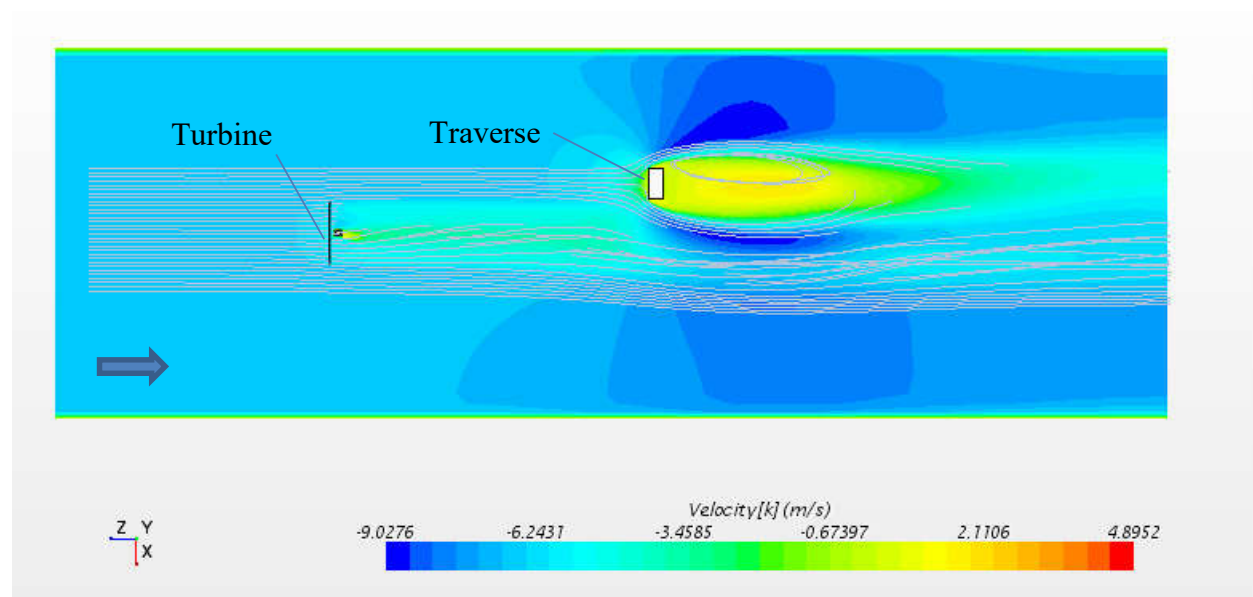


Figure 7-23. Plan view of velocity contour from actuator disk method with traverse located at $x/D_b \sim 5$

As a wind turbine extracts energy from the wind, there is a resulting wind speed decrease in the wake. The wake deficit is defined as the change in wind speed divided by the free stream wind speed, $\Delta U/U_\infty$. For this study, the different CFD methods of simulating the wind turbine are compared using velocity deficit profiles and experimental data at locations designated in Figure 7-13 and Figure 7-14. For the MRF simulations, the residuals and values of the thrust and torque tended to oscillate around a slightly meandering steady state value (see Figure 7-11) which indicates that the influence of flow transients (i.e. separation and vortex shedding at the blade)

may not allow the solution to converge completely in the steady state solution. The velocity profiles also tended to change slightly even after 10,000 iterations. In the actuator disk method, the residuals also oscillated slightly (see Figure 7-12), but the velocity profiles did not change after approximately 1500 iterations.

Figure 7-24 shows a velocity deficit profile comparison at locations just behind the wind turbine. The RBM and actuator disc (BEM) methods show distinct profile gradients due to the shear layer between the wake and the free stream near $y/r=1$ and due to interference with the nacelle (DC motor) near $y/r\sim 0.3$. The RBM method is a better match since it also includes turbulent effects from the blade root and tip vortices.

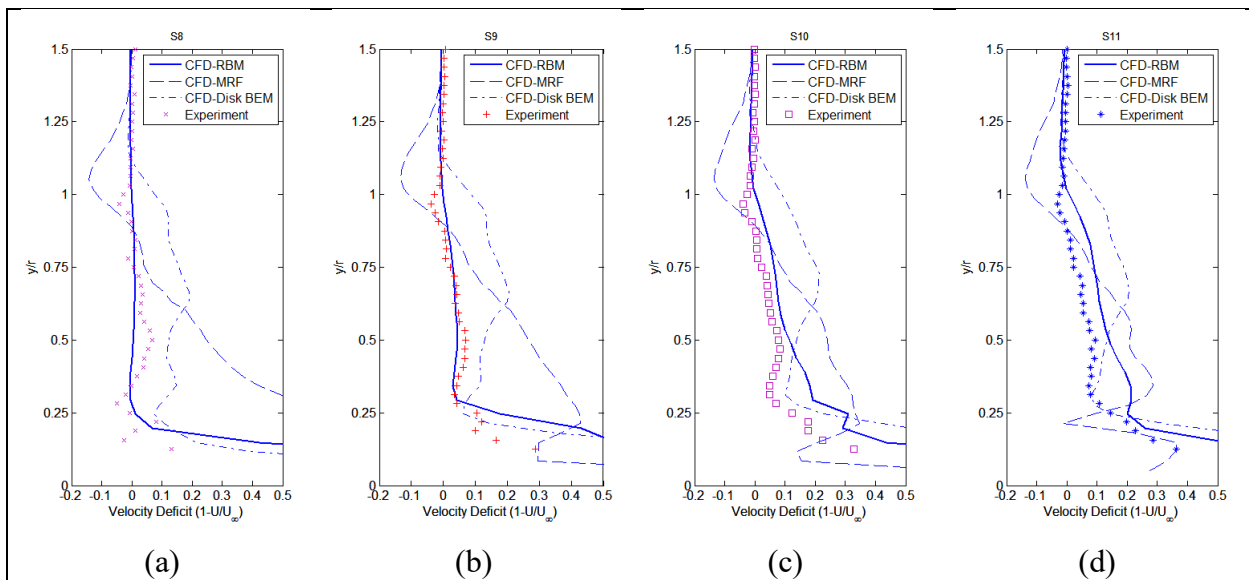


Figure 7-24. Comparison of velocity deficit to experimental data at several vertical measurement planes using different CFD modeling methods: (a) S8 (b) S9 (c) S10 (d) S11, $U_\infty=6.60$ m/s, traverse arm positioned at $x/D_b\sim 8$.

Figure 7-25 shows the profile at locations up to the end of the near-wake region ($x/D_b < 1$). The RSM turbulence model appears to over-predict the deficit from the rotor and from the tower for all methods in this region; however, the shape of the RBM profile is a better match to the experimental measurements. The RBM is a particularly good match at $y/r > 0.3$, even though the effects of the traverse have not been accounted for in the simulation. It is not clear why there is

not as good a match below $y/r < 0.3$, but it may be due to the strong dependence of the wake on the geometry of the blades in the near wake and the presence of the tower and hub disrupts the dependence. The MRF profiles show a lower deficit region at $y/r \sim 1$ which could be due to the failure of the steady state model to predict the vortices in the tip region, resulting in a larger error. There could also be an effect from the meshing between the rotating sub-domain and the stationary domain were the cells have a lower mesh quality; the MRF may be more sensitive to the quality of the cells in that region.

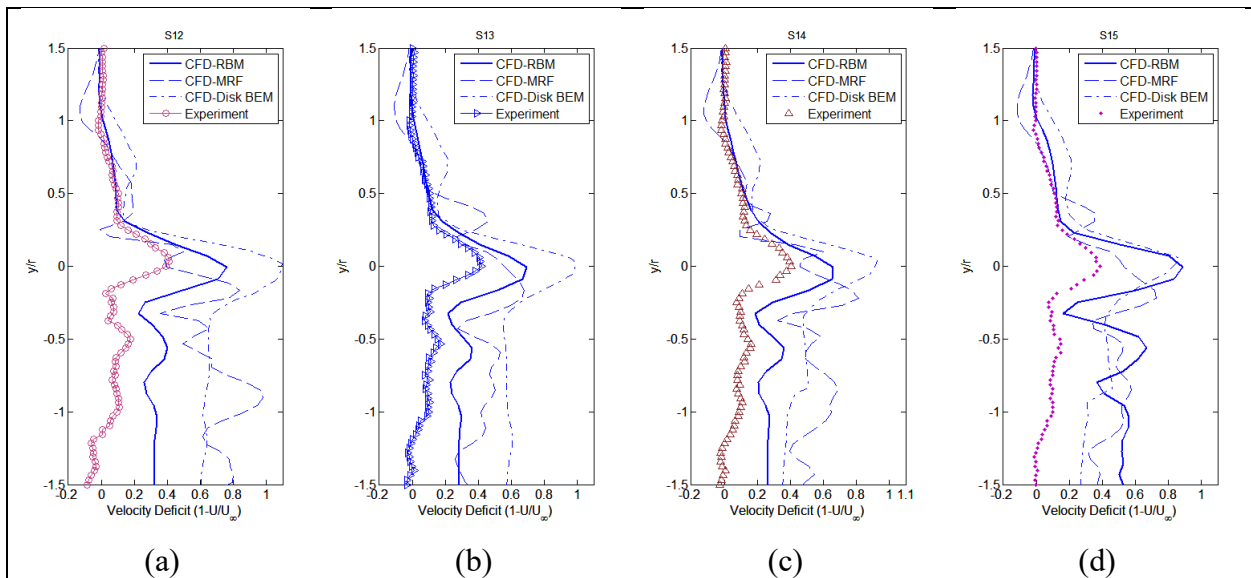


Figure 7-25. Comparison of velocity deficit to experimental data at several vertical measurement planes using different CFD modeling methods: (a) S12 (b) S13 (c) S14 (d) S15, $U_\infty = 6.60$ m/s, traverse arm positioned at $x/D_b \sim 8$.

Moving downstream and further and into the far-wake region ($x/D_b > 1$), the experiment data shows a trend toward an axisymmetric Gaussian profile. Figure 7-26 shows all CFD methods continue to over-predict the deficit and continue to show a much greater deficit between $y/r = -0.3$ and $y/r = 0.3$.

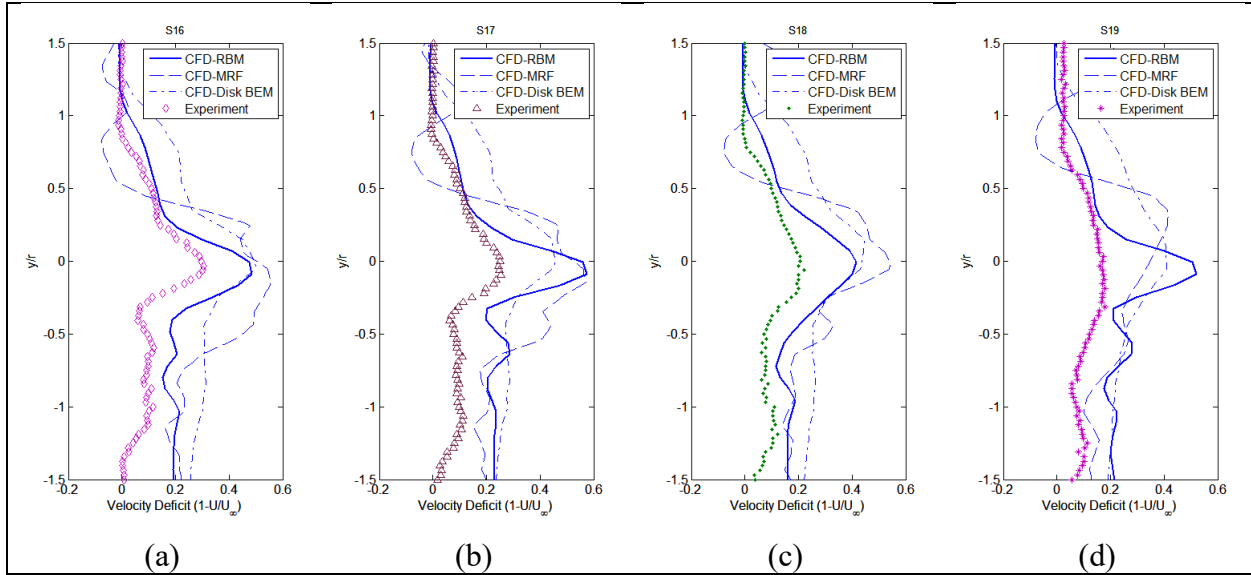


Figure 7-26. Comparison of velocity deficit to experimental data at several vertical measurement planes using different CFD modeling methods: (a) S16 (b) S17 (c) S18 (d) S19, $U_\infty=6.60$ m/s, traverse arm positioned at $x/D_b \sim 8$.

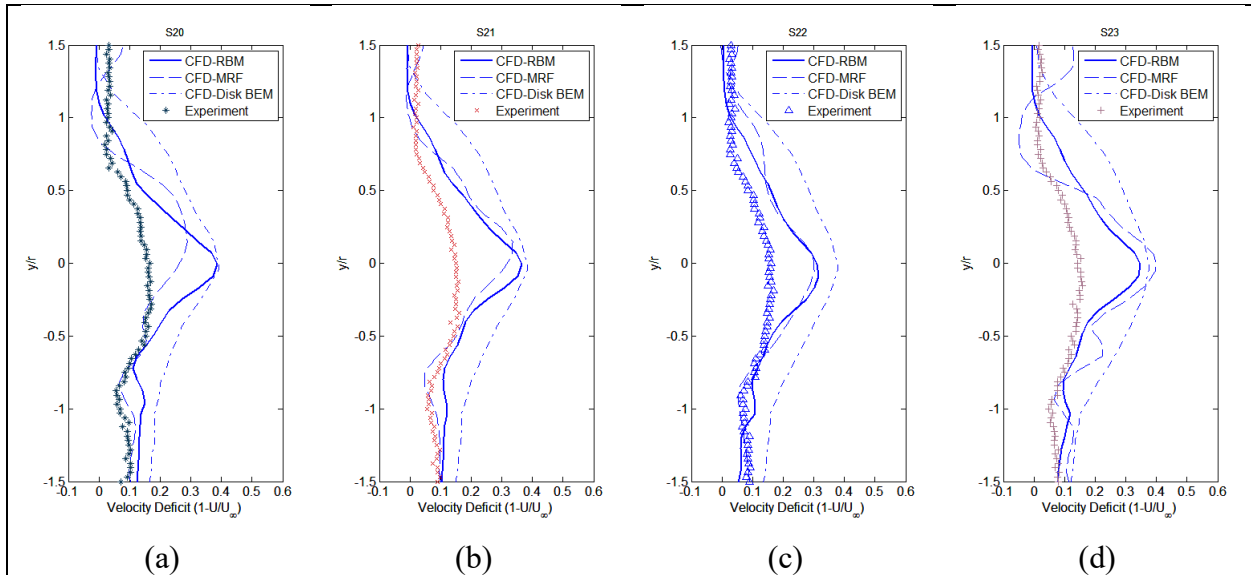


Figure 7-27. Comparison of velocity deficit to experimental data at several vertical measurement planes using different CFD modeling methods: (a) S20 (b) S21 (c) S22 (d) S23, $U_\infty=6.60$ m/s, traverse arm positioned at $x/D_b \sim 8$

In Figure 7-27, the CFD profiles have approached an axisymmetric and Gaussian shape, but continue to over-predict the deficit. At most locations, the BEM simulation shows a higher deficit than the MRF and the RBM. This is likely due to errors in the predicted lift and drag coefficients that are used in the BEM simulation. The actuator disk model relies on accurate

estimates of the lift and drag coefficients to determine momentum forces applied in solving the RANS equations (7.12). The local blade Reynolds numbers for this simulation range from ~ 4000 to $\sim 20,000$ and there is no published data for lift and drag coefficients for the NACA 4424 airfoil for such low Reynolds numbers. The Reynolds numbers for this research were calculated using QBLADE/XFOIL, but the ability of the software to accurately predict lift and drag coefficients at such low Reynolds numbers has not been verified.

It is important to emphasize that the predicted velocity deficit profiles in Figure 7-24 through Figure 7-27 were taken from simulations where the traverse arm was located at $x/D_b \sim 8$. Thus the simulation results do not account for the location of the traverse. Velocity contour plots have shown the traverse location will affect the wake deficit. Experimental observation of turbine speed relative to the traverse position has also been noted.

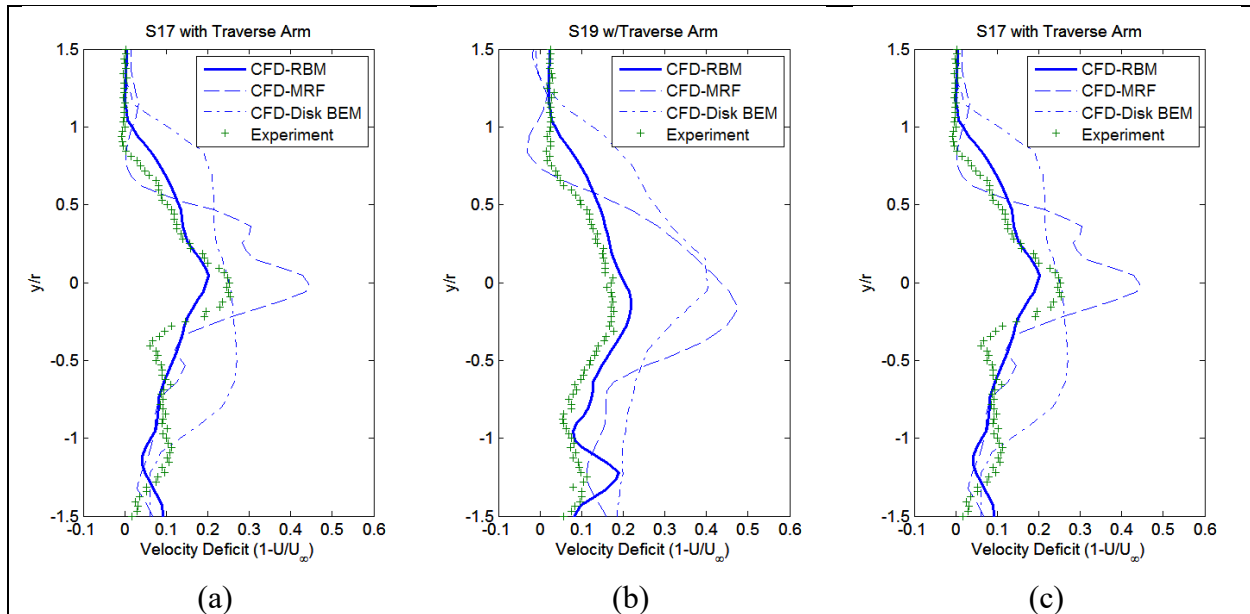


Figure 7-28. Comparison of velocity deficit to experimental data for the RBM method with the traverse arm positioned at: (a) $x/D_b \sim 1$ (b) $x/D_b \sim 3$ (c) $x/D_b \sim 5$; $U_\infty = 6.60$ m/s.

Figure 7-28 shows the effect of including the traverse arm in the simulations. With the traverse included in the simulation, flow diverted toward the wake created more mixing between free stream flow and wake flow which eroded the velocity deficit. The RSM turbulence model

combined with the rigid body motion method shows excellent agreement with experimental data. Improvements were made in the actuator disk method and MRF methods when including the traverse in the simulation, but the improvements are more difficult to recognize. Figure 7-29 shows the percent difference between the experimental data and the simulation results with the traverse location corresponding to measurements. Clearly, the RBM method is better at predicting the deficit with simulation results within 12% of the experimental results when accounting for the effects of the traverse.

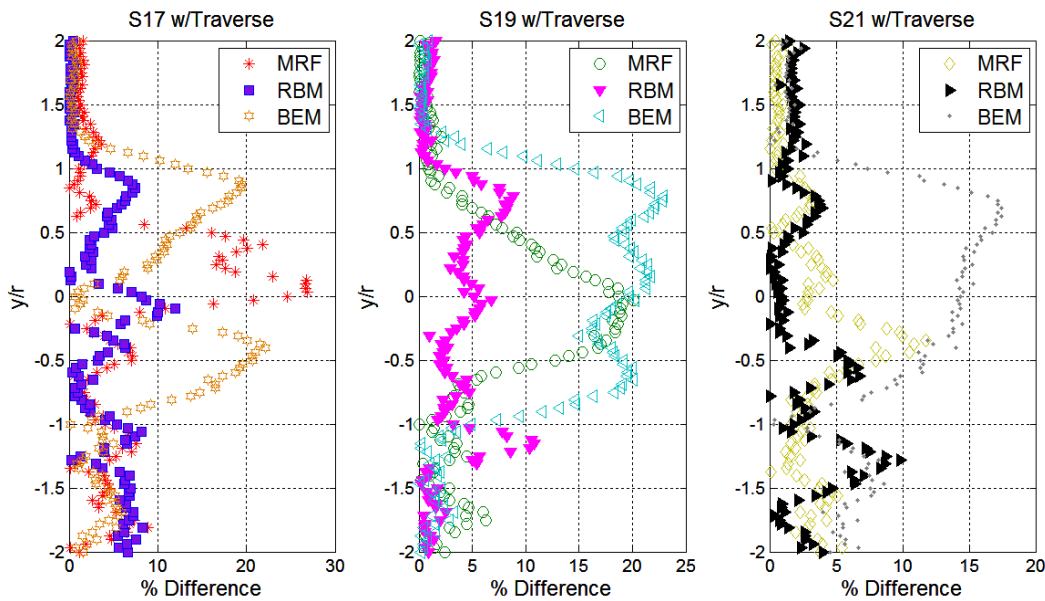


Figure 7-29. Percent difference between simulation and experiment when accounting for the traverse location.

In addition to the strong agreement in the velocity deficit profiles using the Reynolds Stress Model with the transient RBM method, there is strong visual correlation between high speed images and the numerical results. Figure 7-30 shows the isosurface of the Q-criterion scalar variable colored by vorticity magnitude. The Q-criterion [82] represents regions where rotation dominates strain in the flow. This compares well with the high speed image shown in Figure

7-31. The simulation showed the tip vortices dissipated approximately 3 rotor diameters downstream, which coincides with the high speed images. Additional details on high speed image tests are presented in Section 6.3.

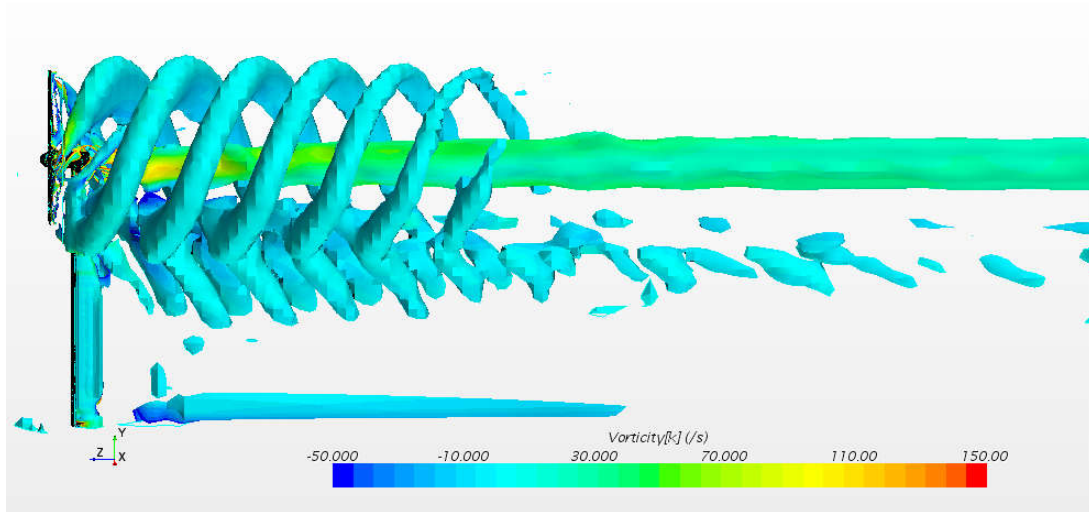


Figure 7-30. Isosurface of Q -criterion, colored by vorticity, from a transient RBM simulation

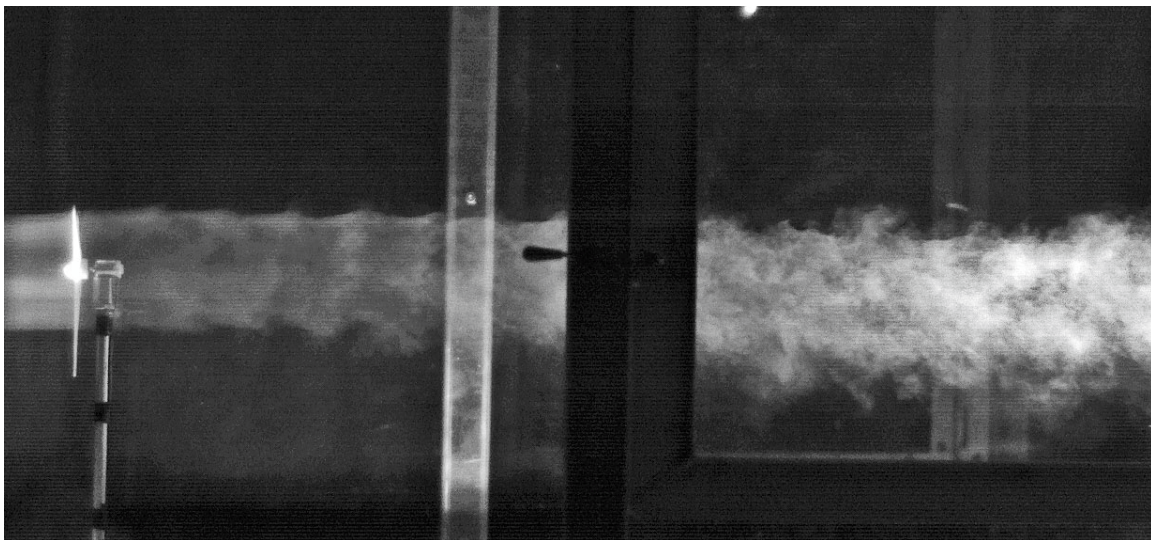


Figure 7-31. High speed camera frame capture showing wake vortex structure and eventual dissipation

8 Conclusions and Recommendations

This research has shown that the Reynolds Stress Model (RSM) for turbulence closure can be successfully applied to a fully discretized wind turbine and produce an accurate, numerically stable solution. In providing a solution to the RANS equations, RSM provides direct computation of the Reynolds shear stress components, as opposed to the eddy viscosity approach used in $k-\varepsilon$ or $k-\omega$ turbulence models. Knowledge of the Reynolds stresses can help wind turbine designers and wind farm designers understand where regions of high turbulence kinetic energy occur in the wake by correlating to the degree of anisotropy of the Reynolds stresses. Transient effects, such as vortex shedding at the blade tips or from the tower can be simulated and help mitigate noise or structural vibration concerns in the blades. With adequate estimation of lift and drag coefficients and the inherent reduction in the mesh size, the actuator disk method is more practical in simulating multiple wind turbines in a wind farm. Wind tunnel experiments have shown the interaction between the tower and the rotor can create significant turbulence that can be present in the far wake. Thus, the effects of the tower should not be ignored in CFD simulations. Recommendations for further study include determination of lift and drag coefficients at low Reynolds numbers and simulation of multiple turbines to compare to experimental results.

References

- [1] A. W. E. Association, "Fourth Quarter 2014 Market Report," AWEA, Washington, D.C., 2015.
- [2] A. Crespo, J. Hernandez and S. Frandsen, "Survey of modeling methods for wind turbine wakes and wind farms," *Wind Energy*, vol. 2, pp. 1-24, 1999.
- [3] L. Vermeer, J. Sorenson and A. Crespo, "Wind turbine wake aerodynamics," *Progress in Aerospace Sciences*, vol. 39, pp. 467-510, 2003.
- [4] M. Hansen, J. Sorensen, S. Voutsinas, N. Sorensen and H. A. Madsen, "State of the art in wind turbine aerodynamics and aeroelasticity," *Progress in Aerospace Sciences*, vol. 42, pp. 285-330, 2006.
- [5] B. Sande, S. van der Pijl and B. Koren, "Review of computational fluid dynamics for wind turbine wake aerodynamics," *Wind Energy*, vol. 14, pp. 799-819, 2011.
- [6] J. Sumner, C. Watters and C. Masson, "CFD in Wind Energy: The Virtual Multiscale Wind Tunnel," *Energies*, vol. 3, pp. 989-1013, 2003.
- [7] A. Miller, B. Chang, R. Issa and G. Chen, "Review of computer-aided numerical simulation in wind energy," *Renewable and Sustainable Energy Reviews*, vol. 25, pp. 122-134, 2013.
- [8] P. Ma, M. Li, J. Jilesen, F. Lien, E. Yee and H. Harrison, "A comparison of coarse-resolution numerical simulation with experimental measurements of wind turbine aerodynamic performance," *Precedia Engineering*, vol. 79, pp. 17-27, 2014.
- [9] E. Sagol, M. Reggio and A. Ilinca, "Assessment of two-equation turbulence models and validation of the performance characteristic of an experimental wind turbine by CFD," *ISRN Mechanical Engineering*, vol. 2012, p. 10, 2012.
- [10] M. Carrion, R. Steijl, M. Woodgate, G. Barakos, X. Munduate and S. Gomez-Iradi, "Computational fluid dynamics analysis of the wake behind the Mexico rotor in axial flow conditions," *Wind Energy*, vol. 18, no. 6, pp. 1023-1045, 2014.
- [11] A. AbdelSalam and V. Ramalingam, "Wake prediction of horizontal-axis wind turbine using full-rotor modeling," *Journal of Wind Engineering and Industrial Aerodynamics*, vol. 124, pp. 7-19, 2014.
- [12] P. Rocha, F. Moura Carnerio, M. Vieira da Silva and H. Barbosa Rocha, "k-w SST (shear stress transport) turbulence model calibration: A case study on a small scale horizontal axis wind turbine," *Energy*, vol. 65, pp. 412-418, 2014.
- [13] T. Tran, D. Kim and J. Song, "Computational fluid dynamic analysis of a floating offshore wind turbine experiencing platform pitching motion," *Energies*, vol. 7, pp. 5011-5026, 2014.
- [14] M. Lawson, Y. Li and D. Sale, "Development and verification of a computational fluid dynamics model of a horizontal axis tidal current turbine," in *30th International Conference on Ocean, Offshore, and Arctic Engineering*, Rotterdam, The Netherlands, 2011.

- [15] J. Seydel and A. Aliseda, "Wind turbine performance in shear flow and in the wake of another turbine through high fidelity numerical simulations with moving mesh technique," *Wind Energy*, vol. 16, pp. 123-138, 2013.
- [16] F. Castellani and A. Vignaroli, "An application of the actuator disc model for wind turbine calculations," *Applied Energy*, vol. 101, pp. 432-440, 2013.
- [17] F. Castellani, A. Gravdahl, G. Crasto, E. Piccioni and A. Vignaroli, "A practical approach in the CFD simulation of off-shore wind farms through the actuator disc technique," *Energy Procedia*, vol. 35, pp. 274-284, 2013.
- [18] L. Martinez Tossas and S. Leonardi, "Wind turbine modeling for computational fluid dynamics," National Renewable Energy Laboratory (NREL), Golden, CO, 2012.
- [19] R. Storey, S. Norris and J. Cater, "An actuator sector method for efficient transient wind turbine simulation," *Wind Energy*, vol. 18, pp. 699-711, 2015.
- [20] S. Aubrun, S. Loyer, P. Hancock and P. Hayden, "Wind turbine wake properties: comparison between a non-rotating simplified wind turbine model and a rotating model," *Journal of Wind Engineering and Industrial Aerodynamics*, vol. 120, pp. 1-8, 2013.
- [21] S. Aubrun, S. Loyer, G. Espana, P. Hayden and P. Hancock, "Experimental study on the wind turbine wake meandering with the help of a non-rotating simplified model and of a rotating model," in *AIAA Aerospace Sciences Meeting including the New Horizons Forum and Aerospace Exposition*, Orlando, FL, 2011.
- [22] D. Medici, "Experimental Studies of Wind Turbine Wakes-Power Optimisation and Meandering," KTH Mechanics, Royal Institute of Technology, 2005.
- [23] D. Medici, "The upstream flow of a wind turbine: blockage effect," *Wind Energy*, vol. 14, pp. 691-617, 2011.
- [24] S. Barber, N. Chokani and R. Abhari, "Effect of wake flow non-uniformity on wind turbine performance and aerodynamics," in *Proceedings of ASME Turbo Expo*, Vancouver, B.C., Canada, 2011.
- [25] L. Chamorro and F. Porte-Agel, "A wind-tunnel investigation of wind-turbine wakes: boundary layer effects," *Boundary-Layer Meteorology*, vol. 132, no. 1, pp. 129-149, 2009.
- [26] D. Medici and P. Alfredsson, "Measurements on a wind turbine wake: 3D Effects and bluff body vortex shedding," *Wind Energy*, vol. 9, pp. 219-236, 2006.
- [27] T. Maeda, Y. Kamada, M. Junsuke, S. Yonekura, T. Ito, A. Okawa and T. Kogaki, "Wind tunnel study on wind and turbulent intensity profiles in wind turbine wake," *Journal of Thermal Science*, vol. 20, no. 2, pp. 127-132, 2011.
- [28] L. Chamorro, R. A. Aarndt and F. Sotiropoulos, "Reynolds number dependence of turbulence statistics in the wake of wind turbines," *Wind Energy*, vol. 15, pp. 733-742, 2012.
- [29] S. McTavish, S. Rodrigue, D. Feszty and F. Nitzsche, "An investigation of in-field blockage effects in closely spaced lateral wind farm configurations," *Wind Energy*, 2014.
- [30] L. Chamorro and F. Porte-Agel, "Turbulent flow inside and above a wind farm: a wind tunnel study," *Energies*, vol. 4, pp. 1916-1936, 2011.
- [31] J. Hu, M. Guala, J. Sheng and L. Chamorro, "High speed PIV measurement of impinging flow on a horizontal axis wind turbine," in *Proceedings of ASME 2012 Fluids Engineering Summer Meeting*, Rio Grande, Puerto Rico, 2012.

- [32] Z. Yang, P. Sarkar and H. Hu, "An experimental investigation on the wake characteristic of a wind turbine in an atmospheric boundary layer wind," in *29th AIAA Applied Aerodynamics Conference*, Honolulu, HI, 2011.
- [33] F. Massouh and I. Dobrev, "Investigation of flow downstream of a horizontal axis wind turbine," in *ISEIMA '06-First International Symposium on Environment Identities and Mediterranean Area*, Corte-Ajaccio, France, 2006.
- [34] R. Cal, J. Lebron, L. Castillo, H. Kang and C. Meneveau, "Experimental study of the horizontally averaged flow structure in a model wind turbine array boundary layer," *Journal of Renewable and Sustainable Energy*, vol. 2, 2010.
- [35] J. Lebron, L. Castillo, R. Cal, H. Kang and C. Meneveau, "Interaction between a wind turbine array and a turbulent boundary layer," in *48th AIAA Aerospace Sciences Meeting Including the New Horizons Forum and Aerospace Exposition*, Orlando, FL, 2010.
- [36] D. Cabezon, E. Migoya and A. Crespo, "A semi-parabolic wake model for large offshore wind farms based on the open source CFD solver OpenFOAM," *ITM Web of Conferences-First Symposium on OpenFOAM in Wind Energy*, vol. 2, p. 14, 2014.
- [37] A. Makridis and J. Chick, "CFD Modeling of the wake interactions of two wind turbines on a Gaussian hill," in *EACWE 5*, Florence, Italy, 2009.
- [38] D. Marten, J. Wendler, G. Pechlivanoglou, C. Nayeri and C. Paschereit, "QBLADE: An open source tool for design and simulation of horizontal and vertical axis wind turbines," *International Journal of Emerging Technology and Advanced Engineering*, vol. 3, no. 3, pp. 264-269, 2013.
- [39] M. Drela, "XFOIL: An analysis and design system for low Reynolds number airfoils," *Lecture Notes in Engineering 54*, in *Low Reynolds Number Aerodynamics*, Springer-Verlag 1989.
- [40] T. Burton, N. Jenkins, D. Sharpe and E. Bossanyi, *Wind Energy Handbook*, 2nd Edition, Wiley & Sons, 2011.
- [41] A. Welsh, "Low turbulence wind tunnel design and wake characterization," University of Wisconsin Milwaukee Digital Commons-Theses and Dissertations, Milwaukee, WI, 2013.
- [42] A. Gupta, "Development of novel passive control techniques for more uniform temperature at combustor exit and hybrid LES/RANS modeling," University of Wisconsin-Milwaukee, PhD Thesis, Milwaukee, WI, 2014.
- [43] M. Ibrahim, A. Alsultan, S. Shen and R. Amano, "Advances in horizontal axis wind turbine blade designs: introduction of slots and tubercle," *Journal of Energy Resources Technology*, vol. 137, no. 5, 2015.
- [44] M. Manshadi, B. Keshavarz, M. Soltani and K. Ghorbanian, "An innovative genetic algorithm approach for direct calibration of X-probe hot wires," *Experimental Techniques*, vol. 36, no. 1, pp. 50-60, 2012.
- [45] J. Moro, P. Vukoslavcevic and V. Blet, "A method to calibrate a hot-wire X-Probe for applications in low-speed, variable-temperature flow," *Measurement Science and Technology*, vol. 14, pp. 1054-1062, 2003.
- [46] M. Hultmark and A. Smits, "Temperature corrections for constant temperature and constant current hot-wire anemometers," *Measurement Science and Technology*, vol. 21, 2010.

- [47] M. Ndoye, J. Delville, D. Heitz and G. Arroyo, "Parameterizable constant temperature anemometer: a new method for the analysis of velocity-temperature coupling in turbulent heat transfer," *Measurement Science and Technology*, vol. 21, 2010.
- [48] M. T. Wylie, A. W. Brown and B. G. Colpitts, "Distributed hot-wire anemometry based on Brillouin optical time-domain analysis," *Optics Express*, vol. 20, no. 14, pp. 15669-15678, 2012.
- [49] N. Rotamy, D. Sumner, S. Akbari and D. Bergstrom, "Calibration of triple-wire probes using an artificial neural network," *Proceedings of the ASME Fluids Engineering Division Summer Conference-2010*, vol. 2, pp. 217-214, 2010.
- [50] R. Zhao, J. Li and A. Smits, "A new calibration method for crossed hot wires," *Measurement Science and Technology*, vol. 15, pp. 1926-1931, 2004.
- [51] Dantec Dynamics, "Installation and User's Guide for Mini CTA 54T30, Publication No. 9040U6094," Dantec Dynamics, Skovlunde, Denmark, 2010.
- [52] K. Bremhorst and J. Listijono, "Static pressure effects on calibration of velocity transducers at nozzle exits," *Experiments in Fluids*, vol. 5, pp. 344-348, 1987.
- [53] Dantec Dynamics, "User's Guide for Hot-Wire Calibrator 54H10, Publication No. 9040U4401," Dantec Dynamics, Skovlunde, Denmark, 2003.
- [54] T. H. Stannov, "A new calibrator for improved performance of hot-wires," in *International Congress on Instrumentation in Aerospace Simulation Facilities*, Piscataway, NJ, IEEE, 1993, pp. 44.1-44.5.
- [55] L. Browne, R. Antonia and L. Chua, "Calibration of X-probes for turbulent flow measurements," *Experiments in Fluids*, vol. 7, pp. 201-208, 1989.
- [56] D. Sandwell, "Biharmonic spline interpolation of GEOS-3 and SEASAT altimeter data," *Geophysical Research Letters*, vol. 14, no. 2, pp. 139-142, 1987.
- [57] M. Foster and A. Evans, "An evaluation of interpolation techniques for reconstructing ionospheric TEC maps," *Geoscience and Remote Sensing*, vol. 46, no. 7, pp. 2153-2164, 2008.
- [58] V. Chemoray and J. Hjarne, "Improving the accuracy of multihole probe measurements in velocity gradients," in *Proceedings of ASME Turbo Expo 2008: Power for Land, Sea and Air*, Berlin, Germany, 2008.
- [59] P. Burrattini and R. Antonia, "The effect of different X-wire calibration schemes on some turbulent statistics," *Experiments in Fluids*, vol. 38, no. 1, pp. 80-89, 2005.
- [60] F. E. Jorgensen, "How to measure turbulence with hot-wire anemometers," Dantec Dynamics - Publication No. 9040U6151, Skovlunde, Denmark, 2002.
- [61] H. Bruun, *Hot-wire Anemometry-Principles and Signal Analysis*, Oxford University Press, 1987.
- [62] A. Perry, *Hot-wire Anemometry*, Clarendon Press, 1982.
- [63] P. Bradshaw, *An Introduction to Turbulence and its Measurement*, Oxford, U.K.: Pergamon Press, 1971.
- [64] Y. Chew and S. Ha, "The directional sensitivities of crossed and triple hot-wire probes," *Journal of Physics E Scientific Instruments*, vol. 21, no. 6, pp. 613-619, 1988.

- [65] O. Bakken and P. Krogstand, "A velocity dependent effective angle method for calibration," *Experiments in Fluids*, vol. 37, pp. 146-152, 2004.
- [66] H. Bruun, M. Khan, H. Al-Kayiem and A. Fardad, "Velocity calibration relationships for hot-wire anemometry," *Journal of Physics E Scientific Instruments*, vol. 21, pp. 225-232, 1988.
- [67] L. King, "On the convection of heat from small cylinders in a stream of fluid: determination of the convection constants of small platinum wires with applications to hot-wire anemometry," *Philosophical Transactions A*, vol. 214, no. 509-522, pp. 373-432, 1914.
- [68] M. Swaminathan, R. Bacic, G. Rankin and K. Sridhar, "Improved calibration of hot-wires anemometers," *Journal of Physics E: Scientific Instruments*, vol. 16, 1983.
- [69] D. Oster and I. Wygnanski, "The forced mixing layer between parallel streams," *Journal of Fluid Mechanics*, vol. 123, pp. 91-130, 1982.
- [70] Mathworks, Inc., "Matlab Documentation," 2015. [Online]. Available: www.mathworks.com/help/ref/linsolve.html. [Accessed April 2014].
- [71] Mathworks, Inc., "Matlab Documentation," 2015. [Online]. Available: www.mathworks.com/help/matlab/ref/griddata.html. [Accessed January 2014].
- [72] B. Sanderse, "Aerodynamics of wind turbine wakes: literature review," ECN, Report ECN-E-09e016, 2009.
- [73] J. Bartl, F. Pierella and L. Sietran, "Wake Measurements Behind An Array of Two Model Wind Turbines," *Energy Procedia*, vol. 24, pp. 305-312, 2012.
- [74] CD-adapco, STAR-CCM+ Users Guide, v9.06.
- [75] H. Versteeg and W. Malalasekera, *An Introduction to Computational Fluid Dynamics-The Finite Volume Method*, Prentice Hall, 1995.
- [76] B. Launder, G. Reece and W. Rodi, "Progress in the development of a Reynolds-stress turbulence closure," *Journal of Fluid Mechanics*, Vols. 38, Pt. 3, pp. 537-566, 1975.
- [77] S. Sarkar and L. Balakrishnan, "Application of a Reynolds stress turbulence model to the compressible shear layer," in *21st Fluid Dyn., Plasma Dyn, and Lasers Conference, AIAA-90-1465*, Seattle, WA, June 1990.
- [78] F. Lien and M. Leschziner, "Assessment of turbulence-transport models including non-linear RNG eddy-viscosity formulation and second-moment closure for flow over a backward-facing step," *Computers Fluids*, vol. 23, no. 8, pp. 983-1004, 1994.
- [79] M. Gibson and B. Launder, "Ground effects on pressure fluctuations in the atmospheric boundary layer," *Journal of Fluid Mechanics*, vol. 83, no. 3, pp. 491-511, 1978.
- [80] C. Rhie and W. Chow, "Numerical study of the turbulent flow past an airfoil with trailing edge separation," *AIAA Journal*, vol. 21, no. 11, pp. 1525-1535, 1983.
- [81] S. Patankar and D. Spalding, "A calculation procedure for heat, mass, and momentum transfer in three-dimensional parabolic flows," *Int. J. Heat Mass Transfer*, vol. 15, p. 1787, 1972.
- [82] J. Hunt, A. Wray and P. Moin, "Eddies, stream, and convergence zones in turbulent flows," Center for Turbulent Research, Report CTR-S88, 1988.

- [83] BIPM Joint Committee for Guides in Metrology, JCGM 100:2008, Evaluation of measurement data-Guide to the expression of uncertainty in measurement JCGM100:2008 (GUM 1995 with minor corrections), Paris: JCGM, 2008.
- [84] A. S. Hussein, "Modeling and simulation of micro-scale wind farms using high performance computing," *International Journal of Computational Methods*, Vol.9, No. 2 2012.
- [85] A. Makridis, "Validation of a CFD model of wind turbine wakes with terrain effects," *Journal of Wind Engineering and Industrial Aerodynamics*, pp. 12-29, 2013.
- [86] I. Abbott, A. von Doenhoff and L. J. Stivers, "Summary of Airfoil Data-NACA Report 824," 1945.
- [87] A. Bechmann, N. Sorenson and F. Zahle, "CFD simulations of the Mexico rotor," *Wind Energy*, vol. 14, pp. 677-689, 2011.
- [88] M. van der Laan, R. Storey, N. Sorensen, S. Norris and J. Cater, "A CFD code comparison for wind turbine wakes," *Journal of Physics: Conference Series*, vol. 524, 2014.
- [89] M. van der Laan, N. Sorensen, P. Rethore, J. Mann, M. Kelly and J. Schepers, "ICOWES2013 Conference," Lyngby, Denmark, 2013.
- [90] D. Medici, "The upstream flow of a wind turbine: blockage effect," *Wind Energy*, v14, pp. 691-617, 2011.
- [91] K. Hanjalic and B. Launder, "A Reynolds stress model of turbulence and its application to thin shear flows," *Journal of Fluid Mechanics*, Vols. 52, Pt. 4, pp. 609-638, 1972.
- [92] P. Lissaman, "Energy Effectiveness of Arbitrary Arrays of Wind Turbines," Aerovironment, Inc. Report AV FR 7058, Pasadena, CA, 1977.
- [93] A. Liddell, G. Smith, W. Schlez, A. Neubert and A. Pena, "Advanced wake model for very closely spaced turbines," in *European Wind Energy Conference*, Athens, Greece, 2006.

Appendix A. LabVIEW Instruments

LabVIEW virtual instruments (.vi's) were constructed to acquire data for hot wire calibration, spectral analysis, and wind turbine testing. Block diagrams of the instruments are shown in through Figure A-. For hot wire calibration using the Dantec 54H10 Calibrator, the hot wire voltage signals were averaged and stored along with user input for the thermistor resistance (ohms), ambient air air temperature (C), barometric pressure (kPa), nozzle differential pressure (Pa), and flow flow angle (deg). The hot wire voltages were sampled at 20 kHz for 0.5 sec. Each time the instrument was run with a different velocity or angle setting, the calibration text file was appended with new data. A sample calibration file is shown in Table A-1.

Table A-1. Sample calibration file.

| Mean Wire 1 Voltage | Mean Wire 2 Voltage | Micro-Manometer Differential Pressure | Thermistor Resistance | Atmospheric Pressure | Yaw Angle | Ambient Temperature |
|---------------------|---------------------|---------------------------------------|-----------------------|----------------------|-----------|---------------------|
| [volts] | [volts] | [Pa] | [ohms] | [kPa] | [deg] | [C] |
| 1.71586 | 1.77386 | 1 | 11880 | 101.4 | 0 | 21 |
| 1.76737 | 1.82782 | 2 | 11880 | 101.4 | 0 | 21 |
| 1.81227 | 1.87477 | 4 | 11880 | 101.4 | 0 | 21 |
| 1.88322 | 1.94797 | 8 | 11880 | 101.4 | 0 | 21 |
| 1.946 | 2.01278 | 15 | 11880 | 101.4 | 0 | 21 |
| 2.02227 | 2.09199 | 30 | 11890 | 101.4 | 0 | 21 |
| 2.1064 | 2.17848 | 60 | 11890 | 101.4 | 0 | 21 |
| 2.15961 | 2.23333 | 90 | 11890 | 101.4 | 0 | 21 |
| 2.20044 | 2.27474 | 120 | 11900 | 101.4 | 0 | 21 |
| 2.23361 | 2.30857 | 150 | 11900 | 101.4 | 0 | 21 |
| 2.26085 | 2.33655 | 180 | 11910 | 101.4 | 0 | 21 |
| 2.28437 | 2.36061 | 210 | 11910 | 101.4 | 0 | 21 |
| 2.30515 | 2.38176 | 240 | 11920 | 101.4 | 0 | 21 |
| 2.32379 | 2.4013 | 270 | 11930 | 101.4 | 0 | 21 |
| 2.34048 | 2.41839 | 300 | 11940 | 101.4 | 0 | 21 |

For spectral analysis tests the instrument was the same as the hot wire calibration instrument except the raw hot wire voltage signals (time series) were saved along with an average turbine

speed. The number of samples acquired was also increased, but was limited based on the buffer size. The instrument had to be run consecutively several times to get a long enough sample time. Since the system was in steady state during these tests, appending the data in consecutive runs would not affect the final results and may provide some level of ensemble averaging.

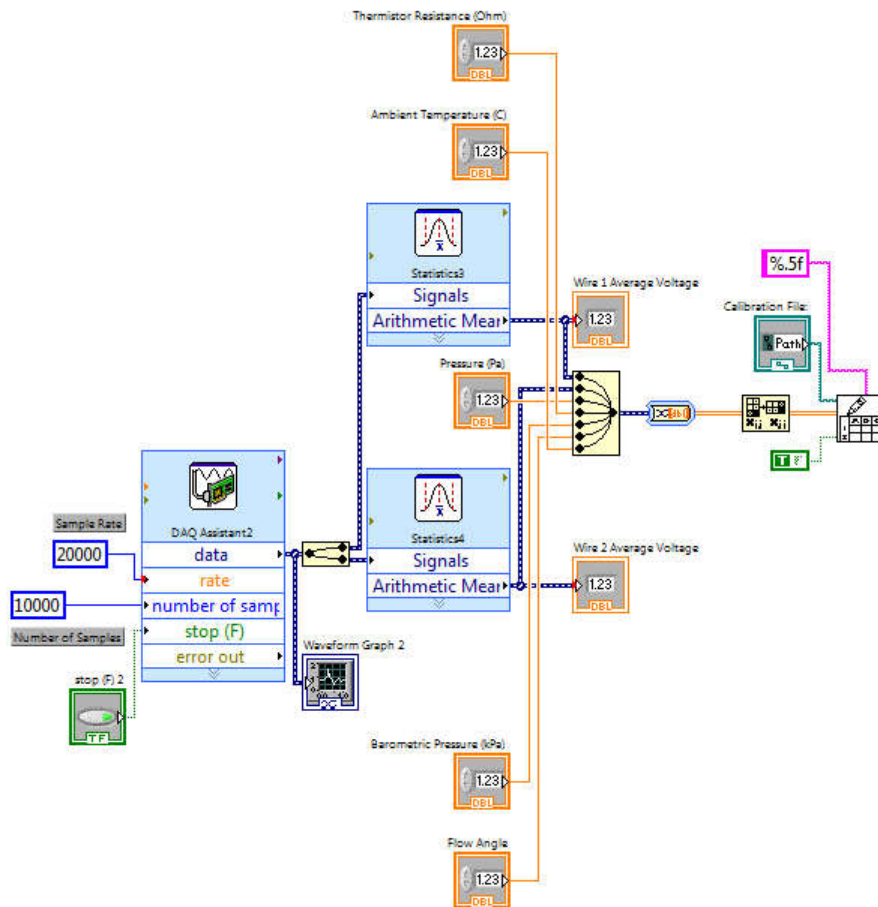


Figure A-1 LabVIEW instrument for hot wire calibration

The LabVIEW block diagram for velocity measurements in the wind tunnel is too large to show in one figure, so it is shown sequentially in Figure A-2 through Figure A-. It was created as a stack and execution is from left to right. The first portion of the instrument, shown in Figure A-2, initializes the Velmex controller and sets the initial position of the hot wire probe before taking measurements.

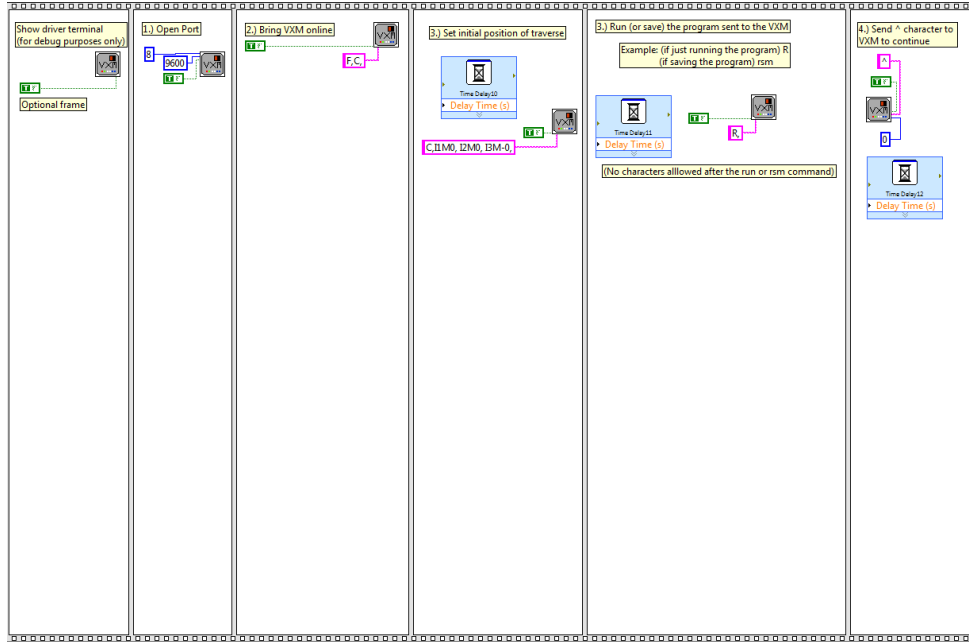


Figure A-2. First level of virtual instrument to set initial position of hot wire and initialize communication with Velmex controller.

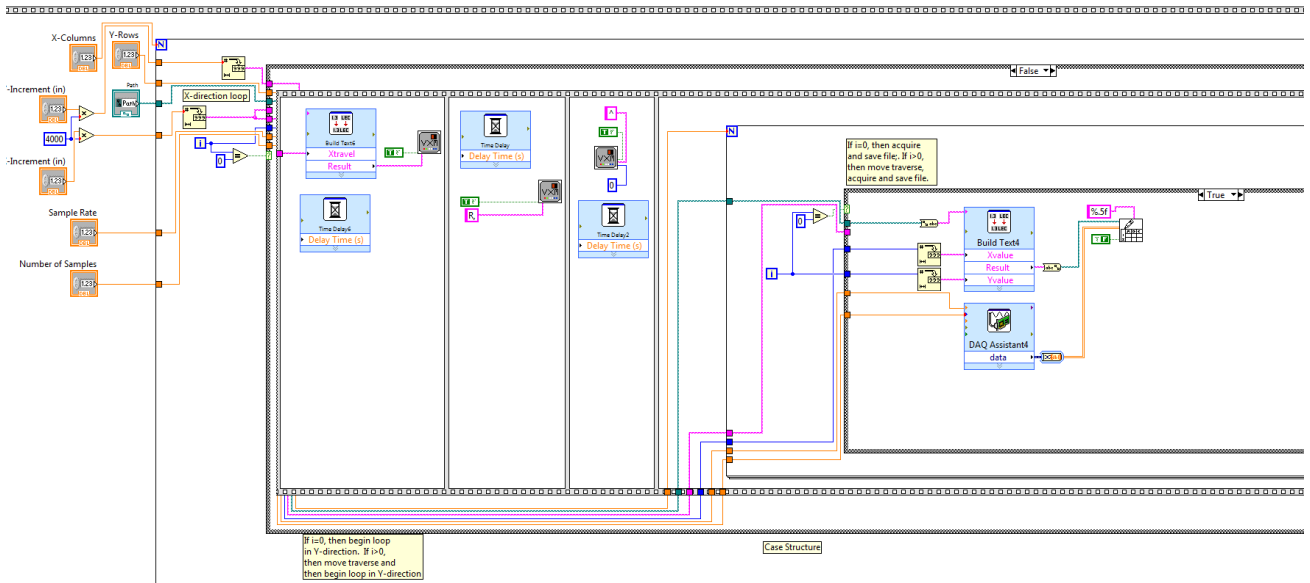


Figure A-3. Secondary level to move traverse and acquire velocity data with directional options to position the traverse

The remaining portions of the instrument move the traverse in the prescribe direction in a prescribed increment with several short delays built in to ensure the arm of the traverse has

stabilized before acquiring the hot wire voltages.

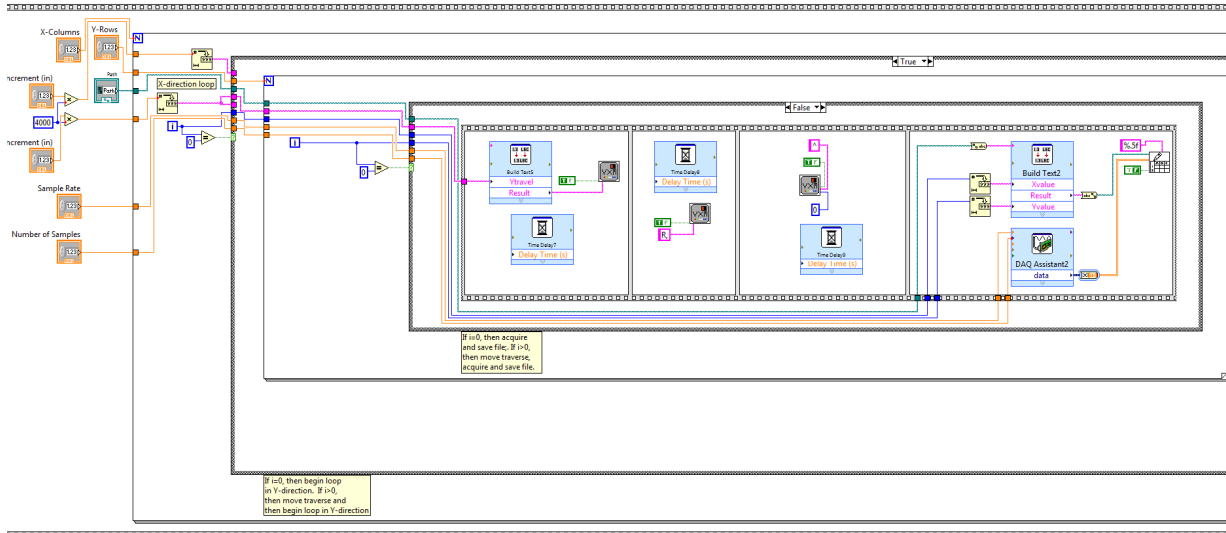


Figure A-4. Alternate secondary level to move traverse and acquire velocity data with directional options to position traverse.

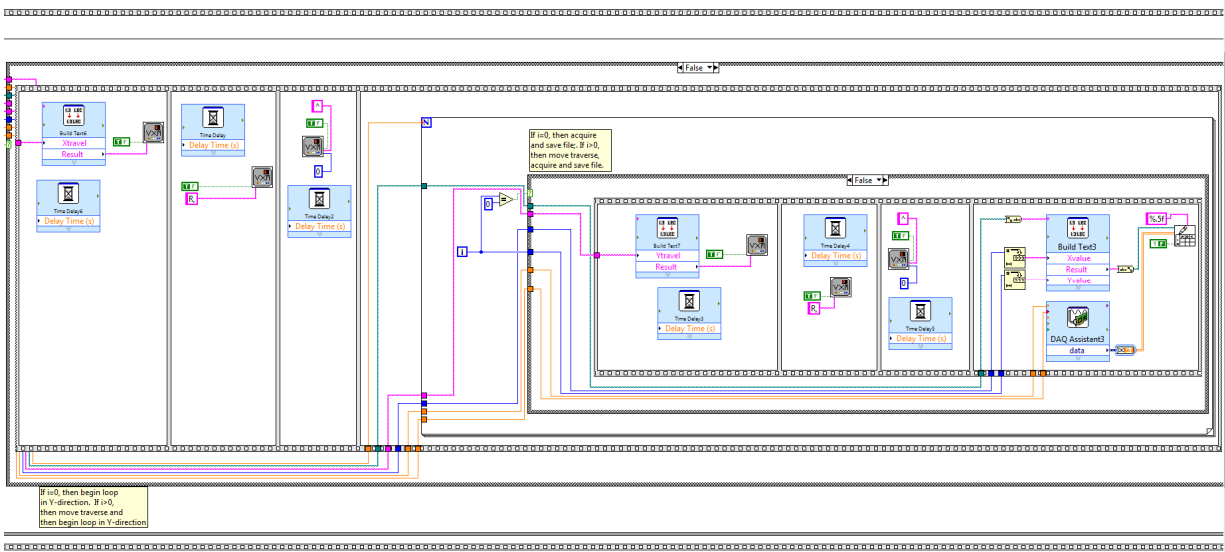


Figure A-5. Final level to move traverse and acquire velocity data with alternate directional option

Appendix B. MATLAB Scripts

hwcal2.m

```
function U_cal = hwcal2(dp,Rt,Pa);
%
% Fuction to evaluate the calibration velocity (m/s) for the Dantec Model
% 5410 calibrator for specific values of the manometer pressure (Pa),
% thermisor resistance (ohm),and atmospheric pressure (kPa). This function
% is based on the 54H10 with Nozzle #1.
%
% Randy Jackson
% 1/15/14
%
format short
%
% Properties of air
%
gamma1 = 1.4; % Specific heat ratio
R = 287.053; % Gas constant (kJ/kg-K)
%
% Details of nozzle in Dantec 54H10 Calibrator (Nozzle #1)
%
do = 63; % Nozzle inlet diameter (mm)
Ao = 3117; % Nozzle inlet area (mm^2)
de = 12.4; % Nozzle exit diameter (mm)
Ae = 121; % Nozzle exit area (mm^2)
FR = 0.97; % Fill ratio
CR = Ao/(FR*Ae); % Contraction ratio
%
% Correction factor as a function of Reynolds Number (Ref. Dantec)
%
Rec = [0 10e3 12e3 22e3 25e3 30e3 35e3 45e3 60e3 80e3 100e3];
cf = [0.0091 0.0114 0.0230 0.0256 0.0262 0.0238 0.0157 0.0109 0.0100 0.100 0.100];
%
% Compute air temperature (K) from thermistor resistance
%
A = 1.128220e-3; %
B = 2.342890e-4; % Steinhart-Hart coefficients for thermistor ( ref:Dantec)
C = 8.692430e-8; %
%
T = 1/(A+B*log(Rt)+C*(log(Rt))^3); % Temp from Steinhart-Hart equation (K)
ao = sqrt(gamma1*R*T); % Speed of sound (m/s)
Po = Pa*1000+dp; % Measured chamber pressure (Pa)
PR = Po/(Pa*1000); % Pressure ratio
M1 = sqrt(2*(PR^((gamma1-1)/gamma1)-1)/(gamma1-1)); % Mach number
a = sqrt(ao^2/(1+((gamma1-1)/2)*M1^2)); % Estimated Mach number
U = M1*a; % Estimated exit velocity (m/s)
rho = Po/(R*T); % Density of air in chamber (kg/m^3)
mu = 17.145+0.0497*(T-273.15)-0.00003*(T-273.15)^2; % Dynamic viscosity of air (E-06
kg/m-s)
Uo = U/CR; % Chamber velocity (m/s)
```

```

h = 0.5*rho*Uo^2; % Stagnation pressure correction (Pa)
Re = rho*U*(de/1000)/(mu*0.000001); % Chamber Reynolds Number
f = interp1(Rec,Cf,Re); % Static pressure correction factor
Po2 = Po+h; % True stagnation pressure (Pa)
P = Pa*1000+dp*f; % True static pressure (Pa)
PR2 = Po2/P; % True pressure ratio
M2 = sqrt(2*(PR2^((gamma1-1)/gamma1)-1)/(gamma1-1)); % True Mach Number
a2 = sqrt(ao^2/(1+((gamma1-1)/2)*M2^2)); % True speed of sound (m/s)
%
U_cal = M2*a2; % Calibration velocity

```

error_eff_angle.m

```

% This script computes the normalized standard deviation from a calibration file
% using the effective angle method and a polynomial fit procedure
clear all
% Get filename and pathname for calibration file
%
[fname,pname] = uigetfile('*.txt','Load Calibration File For Zero Angle');
%
% Change directory to location of single calibration file
%
cd(pname)
format short
%
% Determine calibration velocities
%
[E1,E2,dp,Rt,Pa,angle,Tref]=textread(fname,'%f %f %f %f %f %f %f',15);
for i=1:length(E1)
Ucal(i)= hwcal2(dp(i),Rt(i),Pa(i));
end
%
% Determine polynomial coefficients from zero angle data
%
Pcoeff1 = polyfit(E1',Ucal,4);
Pcoeff2 = polyfit(E2',Ucal,4);
%
% Read calibration data at yaw angle
%
[fname2,pname2] = uigetfile('*.txt','Load Calibration File From Yaw Angle');
cd(pname2)
format short
[E1ea,E2ea,dpea,Rtea,Paea,angleea,Trefea]=textread(fname2,'%f %f %f %f %f %f %f',15);
%Calculate calibration velocity from pressures and temperatures
for i=1:length(E1ea)
Ucalea(i)= hwcal2(dpea(i),Rtea(i),Paea(i));
end
tic
k=0.04; %Yaw angle correction factor
% Equations for Effective Angle Method
U1cal=polyval(Pcoeff1,E1ea);
U2cal=polyval(Pcoeff2,E2ea);
U1=(sqrt(2)/2)*sqrt((1+k)*U2cal.^2-k*U1cal.^2);

```

```

U2=(sqrt(2)/2)*sqrt((1+k)*U1ca1.^2-k*U2ca1.^2);
Uea=(sqrt(2)/2)*U1+(sqrt(2)/2)*U2;
vea=(sqrt(2)/2)*U1-(sqrt(2)/2)*U2;
Umean=sqrt(Uea.^2+vea.^2);
angle1=atan(Vea./Uea)*180/pi;
% Normalized Standard Deviation for each velocity
nsderrU=sqrt((1/length(Ucalea))*sum((1-(Umean./Ucalea')).^2))
angle_error=mean(abs(angle1-angleea))
toc

```

error_polysurf.m

```

% This script calls a function to compute coefficients of a 4th order
% polynomial surface fit for hot wire calibration data. It then computes the
% calibration velocities, normalized standard deviation, and computation
% time
%
clear all
%
% Get filename and pathname full calibration file (all yaw angles)
%
[fname,pname] = uigetfile('*.txt','Load Full Calibration File');
%
% Call function to compute polynomial surface fit coefficients
% Coefficients for velocity are in Vector A
% Coefficients for angle are in Vector B
%
[E1_ca1,E2_ca1,Uca1,theta_ca1,T0,A,B]=fullcal2(fname,pname)
%
% Vectors of exponents for 3rd order polynomial surface fit
%
p1=[3 2 1 0 2 1 0 1 0 0];
p2=[0 1 2 3 0 1 2 0 1 0];
%
% Read calibration data at yaw angle
%
[fname2,pname2] = uigetfile('*.txt','Load Calibration File From Yaw Angle');
cd(pname2)
format short
[E1sf,E2sf,dpsf,Rtsf,Pasf,anglesf,Trefsf]=textread(fname2,'%f %f %f %f %f %f',15);
%Calculate calibration velocity from pressures and temperatures
for i=1:length(E1sf)
Ucalsf(i)= hwcal2(dpsf(i),Rtsf(i),Pasf(i));
end
tic
% Evaluate velocities and angles from polynomial surface equations
for n=1:length(Ucalsf)
temp=0;
temp2=0;
for q=1:10
Upsf1(n)=temp+A(q).*E1sf(n)^p1(q).*E2sf(n)^p2(q);
alphapsf(n)=temp2+B(q).*E1sf(n)^p1(q).*E2sf(n)^p2(q);

```



```

temp=Upsf1(n);
temp2=alphapsf(n);
end
end
Upsf=Upsf1.*cos(alphapsf);
Vpsf=Upsf1.*sin(alphapsf);

% Normalized Standard Deviation for each velocity

nsderrU=sqrt((1/length(Ucalsf))*sum((1-(Upsf1./Ucalsf)).^2))
angle_error=mean(abs(alphapsf'*180/pi-anglesf))

toc

```

fullcal2.m

```

function[E1_cal,E2_cal,Ucal,theta_cal,T0,A,B]=fullcal2(cal_fname,cal_pname)
%
% Function to compute calibration coefficients, calibration velocities (m/s),
% and calibration angles (rad) from a calibration file of hot wire voltages,
% nozzle DP (Pa), thermistor resistance (ohm), calibration angles (deg),
% and reference temperature
%

cd(cal_pname)
format long
[E1,E2,dp,Rt,Pa,theta,Tref]=textread(cal_fname,'%f %f %f %f %f %f %f');

Rt_ave=mean(Rt);
Pa_ave=mean(Pa);
T0=mean(Tref);
m=1;
NU=15;           % Number of velocity measurements in calibration file
Nangle = 9;     % Number of angle measurements in calibration file

for P=1:NU
    for angle=1:Nangle
        E1_cal(m)=E1(m);
        E2_cal(m)=E2(m);
        dp_cal(m)=dp(m);
        theta_cal(m)=theta(m)*pi/180;           % Compute calibration angle in rad
        Ucal(m)=hwcal2(dp(m),Rt_ave,Pa_ave);    % Compute calibration velocity (m/s)
        m=m+1;
    end
end
%
N=length(E1);
%
% Vectors of exponents for 3rd order polynomial surface fit
%
p1=[3 2 1 0 2 1 0 1 0 0];
p2=[0 1 2 3 0 1 2 0 1 0];

```

```

%
%
for i=1:10
    for j=1:10
        C(i,j)=sum(E1.^(p1(i)+p1(j)).*E2.^(p2(i)+p2(j)));
        F(i,j)=C(i,j);
    end
end
%
for k=1:10
    D(k)=sum(Ucal'.*E1.^(p1(k)).*(E2.^p2(k)));
    G(k)=sum(theta_cal'.*E1.^(p1(k)).*(E2.^p2(k)));
end
%
% Solve linear systems CA=D and FB=G to get vectors of calibration
% coefficients A & B.

A=linsolve(C,D');
B=linsolve(F,G');

```

error_surfinterp.m

```

%
% This script uses the MATLAB function griddata.m to evaluate the velocities
% from hot wire anemometer data and then compute the normalized standard deviation
% as an estimate of the error.
%
clear all
% Get filename and pathname full calibration file (all yaw angles)
%
[fname,pname] = uigetfile('*.txt','Load Full Calibration File');
%
% Call function to compute create caliabrations point for grid surface
%
[E1cal,E2cal,Ucal,alphacal,Tcal]=loadcalgrid(fname,pname)
%
% Read calibration data at yaw angle
%
[fname2,pname2] = uigetfile('*.txt','Load Calibration File From Yaw Angle');
cd(pname2)
format short
[E1si,E2si,dpsi,Rtsi,Pasi,anglesi,Trefsi]=textread(fname2,'%f %f %f %f %f %f %f',15);
%Calculate calibration velocity from pressures and temperatures
for i=1:length(E1si)
    Ucalsi(i)= hwcal2(dpsi(i),Rtsi(i),Pasi(i));
end
tic
% Evaluate velocities and angles from polynomial surface interpolation
Usi=griddata(E1cal,E2cal,Ucal,E1si,E2si,'v4');
alphasi=griddata(E1cal,E2cal,alphacal,E1si,E2si,'v4');
Usi=Usi.*cos(alphasi);
Vsi=Usi.*sin(alphasi);

```

```

% Normalized Standard Deviation for each velocity
nsderrU=sqrt((1/length(UcalSI))*sum((1-(Usl./UcalSI)).^2))
angle_err=mean(abs(anglesi-alphaSI*180/pi))
toc

```

polynomial_cal2.m

```

%
% This script computes the calibration coefficients for a hot-wire
% anemometer from a calibration text file using a 4th order polynomial fit.
% The calibration file is a text file with the first column as the wire 1
% voltage (V) , second column as wire 2 voltage (V), third column as the
% manometer pressure (Pa) from the Dantec 54H10 calibrator, fourth column
% as the thermistor resistance (Ohm) from the Dantec 54H10 calibrator, and
% the fifth column is the barometric pressure(kPa). Fifteen (15)
% calibration points are needed.
%
clear all
%
% Get filename and pathname for calibration file
%
[fname,pname] = uigetfile('*.txt','Load Calibration File');
%
% Change directory to location of file
%
cd(pname)
format long
[E1,E2,dp,Rt,Pa,theta,Tref]=textread(fname,'%f %f %f %f %f %f %f');
Rt_ave=mean(Rt);
Pa_ave=mean(Pa);
Tref_ave=mean(Tref);
m=1;
for P=1:15
    Ecal_1(m)=E1(m);
    Ecal_2(m)=E2(m);
    dp_cal(m)=dp(m);
    theta_cal(m)=theta(m)*pi/180;
    Ucal(m)=hwcal2(dp(m),Rt_ave,Pa_ave);
    m=m+1;
end
% Get polynomial coefficients (4th order)
P1 = polyfit(E1,Ucal,4);
P2 = polyfit(E2,Ucal,4);
U1 = polyval(P1,E1);
U2 = polyval(P2,E2);
figure;hold
plot(E1,U1,'o',E1,U1,Ucal,'^')
plot(E2,U2,'x',E2,U2,Ucal,'>')
nsderr1=((1/length(E1))*sum((1-U1./Ucal).^2))^0.5
nsderr2=((1/length(E2))*sum((1-U2./Ucal).^2))^0.5

```

powerlaw_cal2.m

```
%
% This script computes the calibration coefficients for a hot-wire
% anemometer from a calibration text file using a power law equation.
% The calibration file is a text file with the first column as the wire 1
% voltage (V) , second column as wire 2 voltage (V), third column as the
% manometer pressure (Pa) from the Dantec 54H10 calibrator, fourth column
% as the thermistor resistance (Ohm) from the Dantec 54H10 calibrator, and
% the fifth column is the barometric pressure(kPa). Fifteen (15)
% calibration points are needed.
%
clear all
%
% Get filename and pathname for calibration file
%
[fname,pname] = uigetfile('*.txt','Load Calibration File');
%
% Change directory to location of file
%
cd(pname)
format long
[E1,E2,dp,Rt,Pa,theta,Tref]=textread(fname,'%f %f %f %f %f %f');

Rt_ave=mean(Rt);
Pa_ave=mean(Pa);
Tref_ave=mean(Tref);
m=1;
for P=1:15
    Ecal_1(m)=E1(m);
    Ecal_2(m)=E2(m);
    dp_cal(m)=dp(m);
    theta_cal(m)=theta(m)*pi/180;
    Ucal(m)=hwcal2(dp(m),Rt_ave,Pa_ave);
    m=m+1;
end

% call function to compute power law coefficients
[Ak1,Bk1,Ak2,Bk2,n1,n2,RSS_1,RSS_2]=powerlaw_cal(E1,E2,Ucal)

U1=((E1.^2-Bk1)/Ak1).^(1/n1);
% Note: Linear fit in function is actually E^2=AU^2+B
U2=((E2.^2-Bk2)/Ak2).^(1/n2);
figure;hold
plot(E1.^2,U1.^n1,'o',E1.^2,Ucal.^n1,'^')
plot(E2.^2,U2.^n2,'x',E2.^2,Ucal.^n2,'>')

nsderr1=((1/length(E1))*sum((1-U1./Ucal).^2))^0.5
nsderr2=((1/length(E2))*sum((1-U2./Ucal).^2))^0.5
```

powerlaw_cal.m

```
function [Ak1, Bk1, Ak2, Bk2, n1, n2, RSS_1, RSS_2]=powerlaw_cal(E1, E2, Uca1);
%
% function to find the value of n that minimizes the residual for a
% linear fit to a power law:  $E^2=A+B*U^n$  using data from each wire
%

n1_flag=.2:.01:0.6;
n2_flag=.2:.01:0.6;
for i=1:length(n1_flag)
    plin1=polyfit((Uca1.^n1_flag(i))', E1.^2, 1)
    plin2=polyfit((Uca1.^n2_flag(i))', E2.^2, 1);

    plinfit1=polyval(plin1, Uca1.^n1_flag(i)', 1);
    plinfit2=polyval(plin2, Uca1.^n2_flag(i)', 1);

    RSS1(i)=sum((E1.^2-plinfit1).^2);
    RSS2(i)=sum((E2.^2-plinfit2).^2);

end
figure; plot(n1_flag, RSS1, '-o', n2_flag, RSS2, '-^')
SStot1=(length(E1)-1)*var(E1.^2);
SStot2=(length(E2)-1)*var(E2.^2);
RSQ1=1-RSS1/SStot1;
RSQ2=1-RSS2/SStot2;

RSS_1=min(RSQ1);
RSS_2=min(RSQ2);

for j=1:length(n1_flag)
    if RSS1(j)==min(RSS1)
        n1=n1_flag(j);
        minfit1=polyfit((Uca1.^n1)', E1.^2, 1)
        Ak1=minfit1(1);
        Bk1=minfit1(2);
    end
    if RSS2(j)==min(RSS2)
        n2=n2_flag(j);
        minfit2=polyfit((Uca1.^n2)', E2.^2, 1)
        Ak2=minfit2(1);
        Bk2=minfit2(2);
    end
end
end
```

emptyspectral.m

```
%
% This script computes the flow and turbulence statistics from a
% hot wire anemometer file
%
clear all
```

```

%
% Load calibration grid
%
calpname='C:\Users\Randy\Documents\UWM Research Project\Data\Hot_wire_calibration\08Sep2013';
calfname='08Sep2013_full_mod.txt'
[E1ca1,E2ca1,Uca1,alpha1,Tca1]=loadcalgrid(calfname,calpname);
[fname,pname]=uigetfile('*.txt','Enter data file to process');
cd(pname)
fs=20000; % Hot wire sampling frequency
% Load data file
[E1,E2,mt1,mt2,mt3]=textread(fname,'%f %f %f %f %f');
t=0:1/fs:(length(E1)-1)/fs; % Create time vector
%
% Correct for temperature between data and calibration with wire
% temperature from CTA settings at Tw=250C
%
Tw=250; % wire temperature, C
rho=1.255e-3; % Air density
Tref=21.6; % Temperature during experimental from log file
%
E1corr=sqrt((Tw-mean(Tca1))./(Tw-Tref)).*E1;
E2corr=sqrt((Tw-mean(Tca1))./(Tw-Tref)).*E2;
% Determine velocity from calibration grid
S=griddata(E1ca1,E2ca1,Uca1,E1corr,E2corr,'v4');
A=griddata(E1ca1,E2ca1,alpha1,E1corr,E2corr,'v4');
U=S.*cos(A); % U-velocity
V=S.*sin(A); % V-velocity
N=length(U);
Uave=mean(U); % Mean U-velocity
Vave=mean(V); % Mean V-velocity
ut=U-Uave; % Fluctuating portion of U-velocity
vt=V-Vave; % Fluctuating portion of V-velocity
urms=sqrt((1/(N-1))*sum(ut.^2)); % Urms
vrms=sqrt((1/(N-1))*sum(vt.^2)); % Vrms
Iu=urms/Uave*100; % Relative turbulent intensity, u
Iv=vrms/Vave*100; % Relative turbulent intensity, v
It=100*sqrt(1/2*(urms^2+vrms^2)/(Uave^2+Vave^2)); %Total TI
resx=mean(ut.^2); % u-Reynolds normal stress component
resy=mean(vt.^2); % v-Reynolds normal stress component
resxy=mean(ut.*vt); % uv-reynolds shear stress component
%lateral transport quantities
uuv=mean(ut.^2.*vt);
vvu=mean(vt.^2.*ut);
skewu=(1/N)*sum(ut.^3/urms^3); % Skewness
skewv=(1/N)*sum(vt.^3/vrms^3);
kurtu=(1/N)*sum(ut.^4/urms^4); % Kurtosis
kurtv=(1/N)*sum(vt.^4/vrms^4);
meanquants=[Uave,Vave,urms,vrms,Iu,Iv,It,resx,resy,resxy,uuv,vvu,...
skewu,skewv,kurtu,kurtv];
% Power spectral density
[pxx,f] = pwelch(ut,2000,1000,2000,fs);
plot(f,10*log10(pxx),'k')

```

Appendix C. Measurement Uncertainty and Error

Uncertainty for hot wire measurement was evaluated for a single velocity sample using guidelines from a hot-wire anemometer manufacturer [60] and worldwide standards organizations [83]. The uncertainty budget for this study is shown in Table C-1 and is not based on repeated observations, but on manufacturer specifications, scientific judgement, and knowledge of the instrumentation, calibration equipment, and experimental conditions.

Table C-1. Uncertainty budget to determine total expanded uncertainty

| Uncertainty Budget for Hot-Wire Measurement | | |
|---|----------------------------|---|
| Source of Uncertainty | Relative Uncertainty Value | Comment |
| Calibration Velocity | 0.01 | Based on typical relative standard uncertainty of 1% for a dedicated calibrator and a coverage factor of 2 for a normally distributed error. |
| Hot-Wire Conversion Using Surface Interpolation | 0.01 | Based on standard deviation of the curve fitting using the surface interpolation method and a coverage factor of 2. |
| A/D Resolution-Wire 1 | 0.00019 | Based on 16-bit A/D board, 5V voltage range, 6.6 m/s velocity, 28.56 m/s/volt slope of the calibration curve at 6.6 m/s, and 1.732 coverage factor. |
| A/D Resolution-Wire 2 | 0.00018 | Based on 16-bit A/D board, 5V voltage range, 6.6 m/s velocity, 27.32 m/s/volt slope of the calibration curve at 6.6 m/s, and 1.732 coverage factor. |
| Total Expanded Uncertainty, U_{total} | | 2.83% |

The total relative expanded uncertainty, U_{total} , of the velocity combines relative standard uncertainties, $u(y_i)$, using a 95% confidence level. Thus, the total relative expanded uncertainty is calculated from:

$$U_{total} = 2 \cdot \sqrt{\sum u(y_i)^2} \quad (C.1)$$

The relative standard uncertainties are a function of the velocity, the standard deviation of the variables influencing the velocity, sensitivity factors, and a coverage factor which is related to the distribution of the variance (i.e. Gaussian, rectangular). For velocity measurements using hot-wire anemometry, the measurement is known to depend on the calibration velocity, the

conversion of hot-wire voltage to velocity (linearization), data acquisition board resolution, probe position, temperature variations, ambient pressure variation, and humidity. For this study, the effects of humidity and ambient pressure variations were ignored due to environmental controls within the laboratory. The uncertainty due to probe positioning was also ignored based compensation with in-situ calibration and the low order of magnitude compared to other uncertainties. The temperature change between calibration and experiment was accounted for when converting hot-wire voltages to velocity as noted in Section 5.6, thus eliminating the uncertainty due to temperature changes.

For a dedicated calibrator, the standard deviation of the calibration velocity is near 1% which puts the relative standard uncertainty, $U_{calibration}$, at 0.01. The standard deviation of the curve fitting errors using the surface interpolation method was estimated in Section 5.5.4 as 0.01 on average. Uncertainty from the A/D resolution is estimated from knowledge of the A/D board resolution ($n=16$), input voltage range ($E_{AD}=5$ V), velocity (U), and slope of the inverse calibration curve ($\partial U/\partial E$) shown in Figure 5-8 as:

$$U_{resolution} = 1/\sqrt{3} \cdot (1/U) \cdot E_{AD}/2^n \cdot \partial U/\partial E \quad (C.2)$$

The 54H10 calibrator has a published average error of 0.5% of reading (OR) ± 0.02 m/s over a 0.5 to 60 m/s range. The OR designation applies to the velocity calculated by the Dantec spreadsheet. According to Dantec literature, the barometric pressure measurement has a 1:1 influence on the calibration and the micromanometer has a 1:2 influence. The Conex JDB1 digital barometer has 20"-31" Hg range [67.73 kPa -104.98 kPa] with a ± 0.05 Hg accuracy (0.169 kPa). At 101.3 kPa, this equates to less than 0.17% accuracy, but for simplicity, the barometric pressure error contribution to the velocity calculation can be rounded to 0.2%. The Fluke micromanometer used in most calibrations has a 1% of reading accuracy which means the

calibration velocity calculation will have an additional 0.5% OR error. Thus, the error in the calibration velocity can be estimated at 1.2% over the entire velocity range. As a general verification of the calculations for the calibration velocity in MATLAB, the pitot tube supplied with the Fluke Model 922 Airflow Meter was installed in the 54H10 hot-wire calibrator with the nose of the pitot tube at the exit of the nozzle. Table C-2 shows a comparison of calculated calibration velocities based on measured manometer pressures, barometric pressure, and thermistor resistances in the 54H10

Table C-2. Comparison of calibration velocity calculation to pitot tube measurements

| Pitot Tube Velocity Measurement (Fluke 922) | 54H10 Calibrator Manometer Voltage (Setra) | 54H10 Calibrator Manometer Pressure (Setra) | 54H10 Calibrator Manometer Pressure | 54H10 Thermistor Resistance | Calculated Flow From Matlab Scripts | % Diff |
|---|--|---|-------------------------------------|-----------------------------|-------------------------------------|--------|
| [m/s] | [V] | [in H ₂ O] | [Pa] | [Ohm] | [m/s] | [%] |
| 1.303 | 0.0601 | 0.00395 | 0.98 | 11600 | 1.276 | -2.07% |
| 2.007 | 0.0714 | 0.0096 | 2.39 | 11600 | 1.99 | -0.85% |
| 2.584 | 0.084 | 0.0159 | 3.96 | 11600 | 2.562 | -0.85% |
| 3.202 | 0.1015 | 0.02465 | 6.14 | 11600 | 3.189 | -0.41% |
| 3.913 | 0.1261 | 0.03695 | 9.20 | 11600 | 3.904 | -0.23% |
| 4.933 | 0.1685 | 0.05815 | 14.48 | 11600 | 4.897 | -0.73% |
| 6.066 | 0.2289 | 0.08835 | 22.00 | 11600 | 6.036 | -0.49% |
| 8.226 | 0.3773 | 0.16255 | 40.48 | 11600 | 8.188 | -0.46% |
| 11.346 | 0.672 | 0.3099 | 77.18 | 11600 | 11.31 | -0.32% |
| 14.016 | 0.991 | 0.4694 | 116.91 | 11600 | 13.9 | -0.83% |
| 15.64 | 1.227 | 0.5874 | 146.30 | 11600 | 15.54 | -0.64% |
| 17.895 | 1.589 | 0.7684 | 191.38 | 11600 | 17.75 | -0.81% |
| 19.857 | 1.949 | 0.9484 | 236.21 | 11600 | 19.7 | -0.79% |

A Setra Model 26412R5WD2DT1F low differential pressure manometer was used with the 54H10 calibrator since the Fluke 922 micromanometer was being used with the pitot tube. The Setra manometer had a 2.5 in H₂O range and provided a 0-5 V output. The Setra calibration certificate showed a 0.0522 V offset at zero pressure. Table C-2 shows the calculated velocity from the MATLAB script was within 1% of the pitot tube measurements for all but the lowest velocity.

Appendix D. Measurement Locations

Table D-1. Location of measurement planes shown in Figure 6-8, Figure 6-15, and Figure 6-22

| Measurement Plane Locations | | | | | | | | |
|-----------------------------|---------------|-------------|----------------|---------------|-------------|----------------|---------------|-------------|
| Single Turbine | | | Dual Turbines | | | Triple Turbine | | |
| Designation | Location [cm] | x/D_b | Designation | Location [cm] | x/D_b | Designation | Location [cm] | x/D_b |
| S0 | 0.0 | -0.53 | D0 | 0.0 | -0.53 | T0 | 0.0 | -0.53 |
| S1 | 1.3 | -0.47 | D1 | 1.3 | -0.47 | T1 | 1.3 | -0.47 |
| S2 | 2.5 | -0.41 | D2 | 2.5 | -0.41 | T2 | 2.5 | -0.41 |
| S3 | 3.8 | -0.35 | | | | T3 | 3.8 | -0.35 |
| S4 | 5.1 | -0.28 | D4 | 5.1 | -0.28 | T4 | 5.1 | -0.28 |
| S5 | 6.4 | -0.22 | D5 | 6.4 | -0.22 | T5 | 6.4 | -0.22 |
| S6 | 7.6 | -0.16 | D6 | 7.6 | -0.16 | T6 | 7.6 | -0.16 |
| S7 | 8.9 | -0.09 | D7 | 8.9 | -0.09 | T7 | 8.9 | -0.09 |
| Rotor 1 | 10.8 | 0.00 | Rotor 1 | 10.8 | 0.00 | Rotor 1 | 10.8 | 0.00 |
| S8 | 12.7 | 0.09 | D8 | 12.7 | 0.09 | T8 | 12.7 | 0.09 |
| S9 | 14.0 | 0.16 | D9 | 14.0 | 0.16 | T9 | 14.0 | 0.16 |
| S10 | 15.2 | 0.22 | D10 | 15.2 | 0.22 | T10 | 15.2 | 0.22 |
| S11 | 16.5 | 0.28 | D11 | 16.5 | 0.28 | T11 | 16.5 | 0.28 |
| S12 | 17.8 | 0.35 | D12 | 17.8 | 0.35 | T12 | 17.8 | 0.35 |
| S13 | 19.1 | 0.41 | D13 | 20.3 | 0.47 | T13 | 20.3 | 0.47 |
| S14 | 20.3 | 0.47 | D14 | 25.4 | 0.72 | T14 | 25.4 | 0.72 |
| S15 | 21.6 | 0.53 | D15 | 30.5 | 0.97 | T15 | 30.5 | 0.97 |
| S16 | 26.7 | 0.78 | D16 | 35.6 | 1.22 | T16 | 35.6 | 1.22 |
| S17 | 31.8 | 1.04 | D17 | 40.6 | 1.47 | T17 | 40.6 | 1.47 |
| S18 | 41.9 | 1.54 | D18 | 43.2 | 1.60 | T18 | 43.2 | 1.60 |
| S19 | 67.3 | 2.79 | D19 | 45.7 | 1.73 | T19 | 45.7 | 1.73 |
| S20 | 87.6 | 3.80 | D20 | 48.3 | 1.85 | T20 | 48.3 | 1.85 |
| S21 | 108.0 | 4.80 | Rotor 2 | 51.4 | 0.00 | Rotor 2 | 51.4 | 0.00 |
| S22 | 128.3 | 5.80 | D21 | 53.8 | 0.12 | T21 | 53.8 | 0.12 |
| S23 | 148.6 | 6.81 | D22 | 55.1 | 0.18 | T22 | 55.1 | 0.18 |
| - | - | - | D23 | 56.4 | 0.24 | T23 | 56.4 | 0.24 |
| - | - | - | D24 | 57.7 | 0.31 | T24 | 57.7 | 0.31 |
| - | - | - | D25 | 58.9 | 0.37 | T25 | 58.9 | 0.37 |
| - | - | - | D26 | 61.0 | 0.47 | T26 | 61.0 | 0.47 |
| - | - | - | D27 | 66.0 | 0.72 | T27 | 66.0 | 0.72 |
| - | - | - | D28 | 71.1 | 0.97 | T28 | 71.1 | 0.97 |
| - | - | - | D29 | 76.2 | 1.22 | T29 | 76.2 | 1.22 |
| - | - | - | D30 | 81.3 | 1.47 | T30 | 81.3 | 1.47 |
| - | - | - | D31 | 86.4 | 1.73 | T31 | 83.8 | 1.60 |
| - | - | - | D32 | 91.4 | 1.98 | T32 | 86.4 | 1.73 |
| - | - | - | D33 | 96.5 | 2.23 | T33 | 88.9 | 1.85 |
| - | - | - | D34 | 101.6 | 2.48 | Rotor 3 | 92.1 | 0.00 |
| - | - | - | D35 | 106.7 | 2.73 | T34 | 94.0 | 0.09 |
| - | - | - | D36 | 111.8 | 2.98 | T35 | 95.3 | 0.16 |
| - | - | - | D37 | 116.8 | 3.23 | T36 | 96.5 | 0.22 |
| - | - | - | D38 | 121.9 | 3.48 | T37 | 97.8 | 0.28 |
| - | - | - | D39 | 127.0 | 3.73 | T38 | 99.1 | 0.35 |
| - | - | - | D40 | 132.1 | 3.98 | T39 | 101.6 | 0.47 |
| - | - | - | D41 | 137.2 | 4.24 | T40 | 106.7 | 0.72 |
| - | - | - | D42 | 142.2 | 4.49 | T41 | 111.8 | 0.97 |
| - | - | - | D43 | 147.3 | 4.74 | T42 | 116.8 | 1.22 |
| - | - | - | - | - | - | T43 | 121.9 | 1.47 |
| - | - | - | - | - | - | T44 | 127.0 | 1.73 |
| - | - | - | - | - | - | T45 | 132.1 | 1.98 |
| - | - | - | - | - | - | T46 | 137.2 | 2.23 |
| - | - | - | - | - | - | T47 | 142.2 | 2.48 |
| - | - | - | - | - | - | T48 | 147.3 | 2.73 |

Curriculum Vitae

Randall S. Jackson

Education

University of Wisconsin – Milwaukee
Ph.D. Engineering, May 2016.

San Diego State University
M.S. Mechanical Engineering, December 1991

University of Wisconsin – Madison
B.S. Mechanical Engineering, May 1988

Industrial Experience

2003 – Present, Product Development Group Leader – Solenoid Valves, Hydraforce Inc.,
Lincolnshire, IL

1997 – 2003, Senior Project Engineer-INCOVA/EHPV Development, HUSCO International
Inc., Waukesha, WI

1992 – 1997, Design & Research Engineer, Fisher Controls, Marshalltown, IA

1988 –1992, Principle Engineer – Ground Support Equipment, Structures and Liquid Oxygen
Systems, General Dynamics Space Systems Division (GDSSD), San Diego, CA

Research Experience

Jan 1991 – Oct 1991, San Diego State University / GDSSD
Topic: Feasibility of Jet Entrainment Mixer for Condensing Gaseous Hydrogen in a Slush
Hydrogen Tank

July 1995 – June 1997, Fisher Controls, Marshalltown, IA
Topic: Friction Effects in Control Valve Performance and Closed Loop Valve Performance
Using Internal Model Control (IMC) Tuning Methods

Aug 2007 – Jan 2009 University of Wisconsin – Milwaukee / Hydraforce Inc.
Topic: Effects of Varying Geometry on Flow Forces in Hydraulic Spool Valves

Jan 2009 – Jan 2011, University of Wisconsin – Milwaukee, WI
Topic: CFD Simulation of Melting and Solidification in a Laser Engineered Net Shaping Process

Teaching Experience

Jan 2008 – May 2008, Instructor, ME110 – Engineering Fundamentals I, University of Wisconsin Milwaukee – Milwaukee, WI

Sep 2008 – Dec 2008, Instructor, ME301 – Basic Engineering Thermodynamics, University of Wisconsin Milwaukee-Milwaukee, WI

Conference Papers/Presentations

Jackson, R., Amano, R.S., “Application of the Reynolds Stress Model to Direct Modeling and Actuator Disk Simulations of a Small-Scale Horizontal-Axis Wind Turbine”, *Proceedings of the ASME 2016 Fluids Engineering Division Summer Meeting*, July 2016 [accepted]

Jackson, R., Amano, R.S., “Computational Fluid Dynamics (CFD) Simulation of a Model Horizontal-Axis Wind Turbine Using Reynolds Stress Model and Correlation to Experimental Wake Measurements”, *International Conference on Next Generation Wind Energy*, August 2016 [accepted]

Jackson, R. “Friction Effects in Control Valve Performance”, *ISA TECH/EXPO Technology Conference Proceedings*, 1997, v 1, n5, p67-76

Patents/Awards

Jackson R., Casale A., Oligmueller J., *Three-way Poppet Valve with Intermediate Pilot Port*, US Patent 7,921,880, filed August 20, 2007, issued April 12, 2011

Stephenson D., Yang X., Jackson R., Hughes R.C., *Pilot Operated Valve With a Pressure Balanced Poppet*, US Patent 7,341,236, filed March 7, 2006, issued March 11, 2008

Jackson R., Clanton R., Pfaff J., *Hydraulic Control System with Electronic Load Sense Control*, US Patent 7,089,733, filed February 28, 2005, issued August 15, 2006

Stephenson D., Jackson R., Clifton B., *Hydraulic System with Cross Function Regeneration*, US Patent 6,502,393, filed September 8, 2000, issued January 7, 2003

Lovell M., Jackson R., Brestel R., *Low Friction Packing*, US Patent 5,593,166, filed March 2, 1994, issued January 14, 1997